学位論文

Study of tetra-neutron system via exothermic double-charge exchange reaction ^{4}He(^{8}He,^{8}Be)4n

(発熱型2重荷電交換反応 ^{4}He(^{8}He,^{8}Be)4n による4中性子系の研究)

平成26年12月 博士（理学）申請

東京大学大学院理学系研究科
物理学専攻
木佐森　慶一

Abstract

Tetra-neutron systems have attracted considerable attention since candidates of bound tetra-neutron system were reported. While a recent examination of the latest theoretical paper using *ab-initio* calculations suggests that the bound tetra-neutron system does not exist, the possibility that it may form a resonance state is still an open and fascinating question.

We performed missing-mass spectroscopy of the four-neutron system via an exothermic double-charge exchange reaction ^{4}He(^{8}He,^{8}Be)4n. The experiment was carried out at the RI Beam Factory at RIKEN using the SHARAQ spectrometer and the liquid He target system. The secondary beam, ^{8}He at 186 MeV/u, had a large mass excess, which enabled us to produce the four-neutron system with a small momentum transfer of less than 20 MeV/c. In order to obtain the missing-mass spectrum, we measured the momentum of the incident ^{8}He beam with the High-Resolution Beamline and momenta of outgoing two α particles, which were the decay products of the ^{8}Be ejectile, with the SHARAQ spectrometer.

We selected the events produced by ^{4}He(^{8}He,^{8}Be)4n reaction with a precise analysis. Two α particles from the ^{8}Be ejectile were detected in coincidence at the final focal plane of the SHARAQ spectrometer. Furthermore, a method to reconstruct trajectories for more than two particles under high intensity beam ($\sim$2 MHz) was developed. In this analysis, we obtained almost background free data.

We obtained 38 events in the the missing-mass spectrum of the four-neutron system. The spectrum had a strength at low excitation energy region between 0 and 2 MeV. We discussed the shape of the spectrum in comparison with a theoretical calculation assuming the effective range theory including the correlation of di-neutron clusters. We suggest a possibility that the observation is due to the resonance state of the tetra-neutron system.

Contents

List of Figures

List of Tables

Chapter 1

Introduction

1.1 Tetra-Neutron System

1.1.1 Previous Study of the Four-Neutron System

The possible existence of pure neutron nuclei has attracted considerable attention in nuclear physics in the last 60 years [3]. The few-body systems of chargeless nuclei such as di-neutron, tri-neutron and tetra-neutron, which have no Coulomb interaction, are an excellent way to investigate the pure nucleon-nucleon interaction as a basic system of nuclei. These systems are also interesting from the viewpoint of the limits of the nuclear stability beyond the neutron drip-line, especially for correlations in multi-body scattering states.

There were numerous attempts to search for a bound tetra-neutron. In the 1960s, thermal fission [4] and fast-neutron-induced fission [5] of uranium was used to investigate the bound tetra-neutron system. Furthermore, in the 1980s, several experiments using the pion double-charge exchange ^{4}He(π^-, π^+) reaction [2, 6, 7], and a number of transfer reactions [8, 9] were performed. However, all of attempts to detect either bound tetra-neutron or a resonance state have been unsuccessful. The existence of the bound tetra-neutron system was discussed by many authors from a theoretical point of view [8, 9].

In 2002, Marqués et al. [10] reported the surprising result that the possible existence of the bound tetra-neutron was observed by using a breakup reaction of ^{14}Be, most probably in the channel of ^{10}Be+4n. After they reported this experimental result, several theoretical attempts to confirm the experiment were performed, but all of the results were negative [1, 11, 12]. The theoretical papers claimed that our understanding of nuclear few-body systems and nucleon-nucleon interactions will be significantly changed if this

experimental observation of bound tetra-neutron were confirmed.

While those theoretical papers indicated that a bound tetra-neutron does not exist, it is still possible that the tetra-neutron system may form a resonance state. This possibility is an open and fascinating problem.

1.1.2 Possibility as the Resonant State

The possibility of the existence of the tetra-neutron as a resonance state has been discussed in many theoretical papers. Some theoretical attempts [1, 13–15] suggest that the tetra-neutron as a resonance state exists at the low excitation energy region, while others predict a negative result [16, 17].

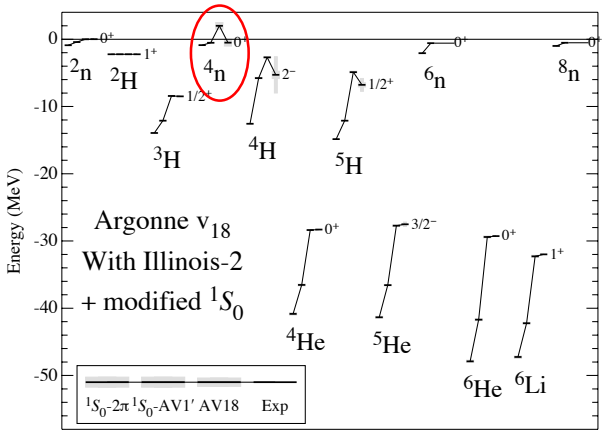

Figure 1.1: Taken from the figure of S. Pieper [1]. Energies of nuclei computed with the AV18/IL2 Hamiltonian with modified nucleon-nucleon (NN) potentials ($^1S_0 - 2\pi$ and $^1S_0$−AV1′) and with no modification (AV18), compared with experimental values for known nuclei. The red circle is the energy of the four-neutron state.

In Pieper [1], the energy level of four-neutron has been studied in the Green's Functions Monte Carlo method [18] with the modern realistic nuclear Hamiltonian, which provide a good description of nuclei up to $A = 10$. They suggest that a broad-resonance of tetra-neutron state may exist at 2 MeV by extrapolatiing of the energy calculated with an external potential well. Figure 1.1 shows the energy state of the nuclei calculated with the realistic potentials AV18/IL2 [19] and modified NN potentials. In the calculation of Fig. 1.1, the three body force for isospin (T), $T = 3/2$ —an interaction between three neutrons—was not considered. This calculation also showed that the level energy of the resonance state crucially depends on the $T = 3/2$

three body force in the NNN potential and $T = 2$ four body force in the NNNN potential.

Recently, it was revealed that many body forces, especially for the isospin $T = 1/2$ three body force, play an important role in the limit of neutron-rich nuclei, the neutron drip line, and evolves regularly from light to medium-mass nuclei [20]. However so far the isospin $T = 3/2$ three-body force and four-body forces have not been investigated. The $T = 3/2$ component of three-nucleon force was predicted to an impressive next-to-next-to-next-to-leading order (N^3LO) in chiral effective field theory, so that the 3n and 4n properties are possible to predict without any unknown couplings to higher-order [21, 22]. For this reason, the isospin $T = 3/2$ three-body force and $T = 2$ four-body force are very interesting topic of not only in the nuclear physics but also astrophysics.

This is also interesting from the point of view of the structure of neutron stars. Understanding the multi-body force in a pure neutron system is important for understanding the nature of neutron stars, since their equation of state includes the many-body force, which is highly uncertain. This plays a crucial role when extrapolating to the high density region found in neutron stars [23].

1.1.3 Multi-Neutron Correlation in Scattering State

The decay property of the many-body system has been investigated to establish the foundation of our understanding of atomic nuclei. For example, in recent years, two-proton radioactivity was observed [24]. However, the multi-neutron decay property had yet to be observed experimentally because of the difficulty in detecting the neutron, while the theoretical study was developed [25]. To overcome the difficulties associated with experimentally neutrons, the scattering state was examined. The scattering state reflects the final state interaction of the reaction product. Thus the scattering state enable us to investigate the correlation of subsystem such as di-neutron correlation and a correlation between di-neutron and di-neutron.

Figure 1.2 shows the result of the momentum spectrum of the four-neutron system produced by the (π^-, π^+) double-charge exchange reaction in Unger *et al.* [2]. There has been no clear evidence of the bound state of the tetra-neutron system. However, an interesting result of this study was that the continuum region in the spectrum was inconsistent with simple phase space decay. If four neutrons decay into phase space with no correlation, the shape of the continuum region of the excitation energy (E) spectrum will be proportional to $E^{7/2}$ (Appendix B). On the other hand, if there is a correlation, for instance, between two di-neutrons, the shape of spectrum will not

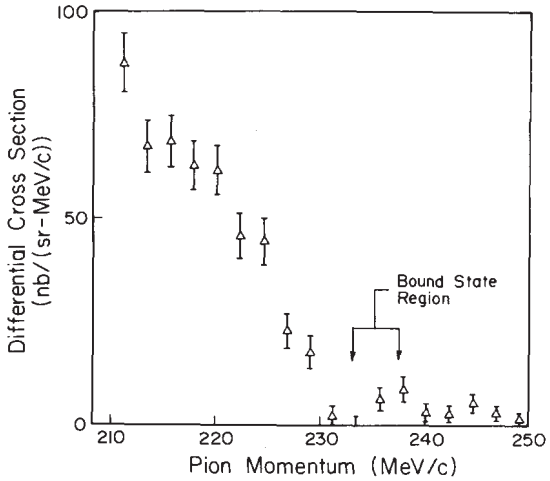

Figure 1.2: Taken from the figure of J. Unger *et al.* [2]. Here, the differential cross section is plotted versus π^+ momentum, with arrows indicating the region in which counts corresponding to a bound tetra-neutron would be expected.

follow the simple phase space decay.

Through the investigation of the correlation, information on the final state interaction of the subsystems is expected to be obtained from the continuum region in the energy spectrum.

1.2 Thesis objectives

The purposes of this experimental work are to investigate

- the existence of the resonance state in a low excitation energy region, and
- investigating the multi-neutron correlation especially for the correlation between the di-neutron and di-neutron from the shape of continuum region in the excitation energy spectrum.

The author was responsible for designing, preparing and performing the experiment and analysis of the data.

The author designed the system around the secondary target and operating the liquid He target system. In particular, the author played an central role in developing the detecting system at final focal plane of the SHARAQ

spectrometer. In order to detect two α particles at the focal plane as large yield as possible, the author developed a new ion optics of the SHARAQ spectrometer. The readout system of the CRDC adopted a multi-hit TDC and flash-ADC, which were essential for acquiring the two particles. The logic circuits to make a trigger signal of CRDCs and a whole DAQ system were developed with FPGA-based logic circuit named LUPO (Logic Unit for Programmable Operation), which makes it easy for us to develop a complicated circuit systematically and to change the circuit by remote control. In order to measure the momentum of the beam in event-by-event under high intensity beam, the multi-hit TDC was adopted.

In the analysis, the author developed the new analysis framework for treating the timing information to reconstruct the particle trajectory of more than two particle under high intensity beam condition, which was in the order of 10^6 cps. This idea and concept will be useful for experiments with the high intensity beam, which will increase in the future at the RIBF. The idea to detect very few events among huge background events was thus important. In this thesis, the detail of the experiment, analysis, result and its interpretation are reported.

Chapter 2

Design of the Experiment

2.1 Exothermic Double-Charge Exchange Reaction

In this work, we applied an exothermic double-charge exchange (^{8}He,^{8}Be) reaction on a ^{4}He target to study the four-neutron system. In the following subsection, we describe the characteristics of this reaction and the reason we employed this reaction.

2.1.1 Exothermic Reaction

Reaction kinematics using an RI beam are quite different from those in a stable-beam induced reaction. Since a reaction Q-value in the projectile system is negative with a stable beam, the momentum transfer (q) is not close to 0 because a large energy transfer is needed. On the other hand, an RI beam induced reaction can produce reaction products with small momentum transfer due to the large mass excess of unstable nuclei. We call the reaction which has a large positive Q-value *exothermic reaction*. Since the transferred energy can be provided from the internal energy of the projectile, the exothermic reaction is a powerful method of the reaction with small momentum transfer.

We measured the exothermic reaction (^{8}He, ^{8}Be) on a ^{4}He target to produce a four-neutron system in an almost recoil-less condition. This characteristic of the exothermic reaction is quite important to investigate in the four-neutron system which is expected to be a very weakly coupled system. Figure 2.1 shows the relation of Q-values between the target system and the projectile system in this reaction.

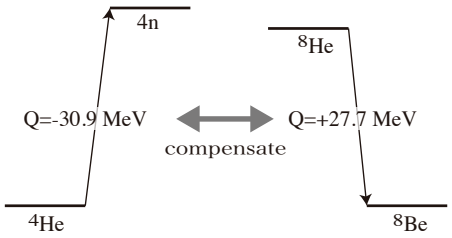

Figure 2.1: Energy relation between the target and projectile systems in the ^{4}He(^{8}He,^{8}Be)4n reaction.

Kinematics

We describe the characteristic relation of momentum transfer and energy transfer in this reaction. In the reaction described as A(a, b)B, the momentum transfer, q, energy transfer, ω, and mass difference, Δm, are defined as:

$$\vec{q} \equiv \vec{p_a} - \vec{p_b} = \vec{p_B}, \tag{2.1}$$
$$\omega \equiv m_B - m_A, \tag{2.2}$$
$$\Delta m \equiv m_a - m_b, \tag{2.3}$$

where m_x and p_x are the masses and momenta of each particle respectively.

Using following approximation:

$$|\Delta m| \ll m_a, \tag{2.4}$$
$$q \ll m_A, \tag{2.5}$$
$$q \ll \sqrt{m_a^2 + p_a^2}, \tag{2.6}$$
$$\theta \ll 1, \tag{2.7}$$

we can describe the relation between q and ω as :

$$\omega \simeq \frac{\Delta m}{\gamma} \pm \beta\sqrt{q^2 - (p_a\theta^2)}. \tag{2.8}$$

Equation (2.8) gives rise to

$$(\beta q)^2 \simeq \left(\omega - \frac{\Delta m}{\gamma}\right)^2 + (\beta p_a \theta)^2 \geq \left(\omega - \frac{\Delta m}{\gamma}\right)^2, \tag{2.9}$$

where β is the velocity parameter and γ is the the γ factor of incidence beam, respectively. The system of units $\hbar = c = 1$ is used in this thesis.

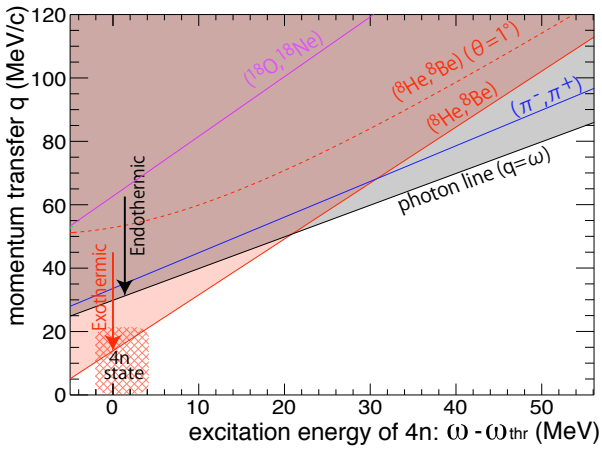

Figure 2.2: Reaction kinematics in the ω-q plane. The horizontal axis $\omega - \omega_{\rm thr}$ corresponds to the excitation energy of a four-neutron system. The shaded red area is the kinematical accessible region by the exothermic ^{4}He(^{8}He,^{8}Be)4n reaction at 200 MeV/u. The shaded gray area is one by endothermic reaction. The solid blue line corresponds to the (π^-, π^+) reaction at 165 MeV in Unger *et al.* [2]. The solid magenta line corresponds to the (^{18}O, ^{18}Ne) reaction at 200 MeV/u as the other example of double-charge exchange reaction.

Figure 2.2 shows the reaction kinematics on the ω-q plane. Here, we define $\omega_{\rm thr}$ is the threshold energy to produce a four-neutron system. Thus $\omega - \omega_{\rm thr}$ represents an excitation energy of the four-neutron system. If the projectile is an RI beam, $\delta m < 0$ can be achieved and the momentum transfer is placed only in the *space-like region* ($q > \omega$), where momentum transfer is larger than energy transfer. Furthermore, this exothermic reaction enables us to reach beyond *photon-line* i.e. we can study the reaction in the *time-like region* ($q < \omega$), where momentum transfer is smaller than energy transfer.

Note that this kinematical characteristics has an sensitivity at a low excitation energy region to investigate four-neutron system rather than previous experiment of (π^-, π^+).

2.1.2 Reaction Mechanism

Responses of nuclear systems through nuclear reactions are characterized by angular momentum transfer (total ΔI, spin ΔS, and orbital ΔL) and isospin transfer (ΔT). The charge exchange reaction occurs through the NN effective interaction of the Fermi type (τ type) and Gamow-Teller type ($\sigma\tau$). For the projectile system, since the Fermi type interactions only contribute between the isospin transfer multiple ($\Delta T = 0$), this (^{8}He, ^{8}Be) reaction, which has a different isospin transfer ($\Delta T = 2$), occurs by a Gamow-Teller type interaction. This is the reason why we chose an incident energy of 200 MeV/u, where the $\sigma\tau$ effective interaction becomes strong.

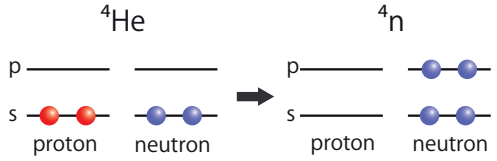

Figure 2.3: Transition of the target system.

Figure 2.3 shows the transition of the target system. Since the $\Delta L = 0$ transitions are blocked by the Pauli exclusion principle at the s orbit, the transition are dominated by the dipole ($\Delta L = 1$) transition. On the other hand, spin-flip transition in the projectile system was assumed, as mentioned above. As a result, the dominant interaction of the reaction of the target system is to be spin-flip dipole transition ($\Delta S = 1, \Delta L = 1$). Then, if we assume the two step transition in the double-charge exchange reaction, intermediate state of the reaction is assumed as ^{8}He + ^{8}Be $\rightarrow$ ^{4}H(1^-) + ^{8}Li(1^+) $\rightarrow$ 4n + ^{8}Be.

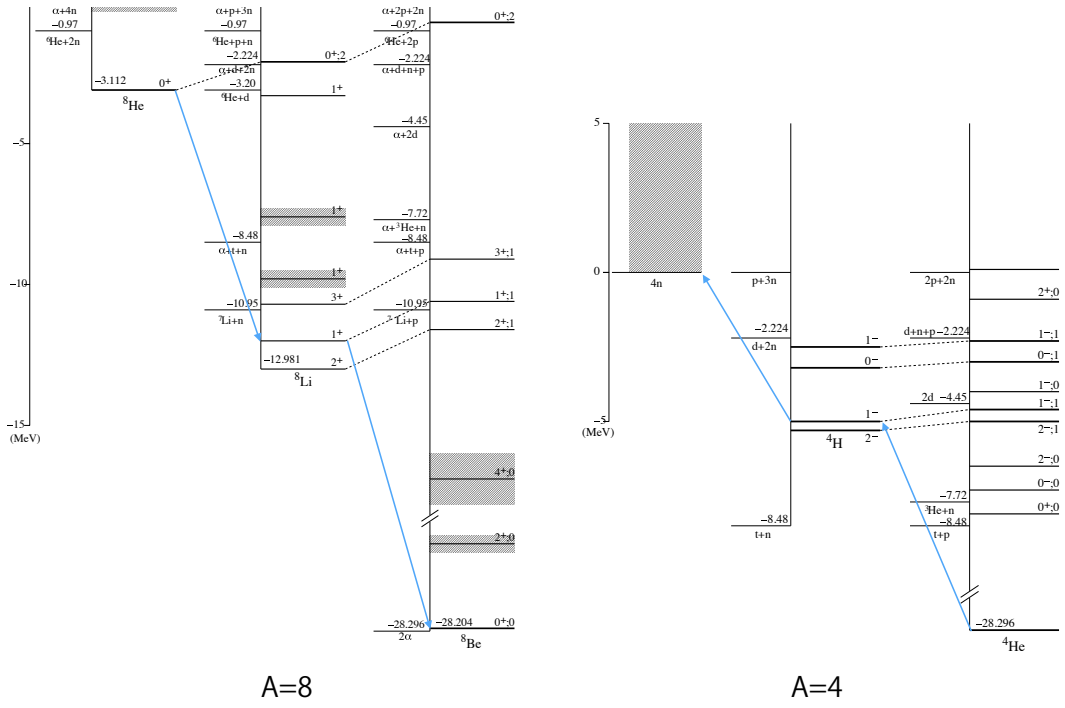

Figure 2.4: Energy level diagram for (a) A=8 isobars. Energy is measured from the α + 4n energy. (b) A=4 isobars. Energy is measured from the 4n energy.

Figure 2.4 shows the energy level diagram of the A=4 and A=8 isobars related to this reaction.

2.2 Missing-Mass Spectroscopy

We performed missing-mass spectroscopy at the RI Beam Factory (RIBF) at the RIKEN. We can obtain an unstable ^{8}He beam on the order of 10^{6} cps as a secondary beam with the BigRIPS fragment separator [26] and the High-Resoluton-Beamline (HRB) [27].

The required energy resolution is about 1 MeV (FHWM) in order to investigate a predicted resonance state, which is around 2 MeV above the threshold and has about 2 MeV width. If we employed a beam energy of 200 MeV/u, the required momentum resolution is less than $\delta p/p$ =1/3000 (FWHM).

In order to measure the momenta of reaction products in high-resolution, we used the SHARAQ spectrometer [28, 29], which was designed for high-resolution spectroscopy with an unstable beam. The designed value of the maximum momentum resolution is $\delta p/p \sim 1/14700$. On the other hand, the momentum distribution of the secondary beam at 200 MeV/u produced by fragmentation is usually about $\pm 2\%$ which is considerably larger than the resolution of the SAHRAQ spectrometer. Therefore, to measure the momentum of the beam, we employed the High-resolution Achromatic transport mode at the BigRIPS and the HRB. This ion optical transport enables us to measure the momentum event-by-event at a dispersive focal plane and obtain the achromatic beam spot at the target. As a secondary target, we employed a liquid hydrogen target [30] with thickness of 120 mg/cm^2.

One of noticeable advantages of the reaction (^{8}He, ^{8}Be ($\rightarrow 2\alpha$)) is to detect two α particles produced from ^{8}He in coincidence at the final focal plane of the SHARAQ spectrometer. The half-life of ^{8}Be is 6.7×10^{-17} sec, which is much shorter than the time of flight of outgoing particles (in the order of 100 ns – 1 μs). Two α particles detection in coincidence enables us to obtain data with a good signal-to-noise ratio. A spread of two α particles in space, the *decay corn*, from the ground state of ^{8}Be at 200 MeV/u is smaller than the acceptance of the SHARAQ spectrometer. The angular distribution of ^{8}Be is expected to have a forward peak because of the $\Delta L = 1$ transition so that we can detect almost all events of ^{8}Be. Furthermore, since the invariant-mass of the ^{8}Be can be reconstructed by the momenta and outgoing angles of the two α particles, we can identify whether their origin is ^{8}Be or not. In terms of the detection efficiency, since the decay channel of ^{8}Be is only two α particles decay without emission of any γ rays, it is not necessary to detect

γ rays.

Chapter 3

Experiment

We performed the experiment at the Radioactive Ion Beam Factory (RIBF) at RIKEN [31]. In order to obtain the missing-mass spectrum, we measured the momentum of the ^{8}He beam with BigRIPS and High-Resolution-Beamline as well as the momenta of two α particles, which were the decay products of the ^{8}Be ejectile, with the SHARAQ spectrometer. This chapter gives a detailed description of the experimental setup. Sec. 3.1 describes the experimental facilities. Sec. 3.2 describes the design of ion optics. Sec. 3.3 depicts a detail of detectors used in this experiment. Sec. 3.4 depicts the liquid He target system. Sec. 3.5 depicts DAQ system. Sec. 3.6 gives a summary of experimental conditions.

3.1 Experimental Facilities

3.1.1 RI Beam Facility

RIBF is designed to achieve up to 440 MeV/u for light ion [31]. A schematic view of RIBF accelerators is shown in Fig. 3.1.

In this experiment, we used the hyper electron cyclotron resonance ion source (hyper-ECR) with the radio frequency (RF) of 14.25 GHz and three cyclotrons, the AVF (K=70 MeV), the RRC (K=540 MeV) and SRC (superconducting , K=2500 MeV) to accelerate an ^{18}O beam of 230 MeV/u. The intensity of the primary ^{18}O beam was a maximum of 400 pnA during this experiment. The SRC was operated with an RF of 13.7 MHz which corresponds to beam bunch separation of 73 ns.

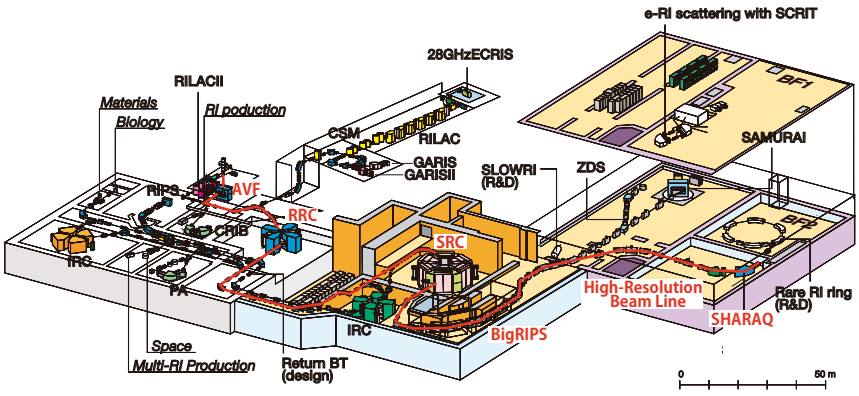

Figure 3.1: Overview of RIBF facility.

3.1.2 BigRIPS and High-Resolution Beam Line

BigRIPS is an in-flight RI beam separator constructed at RIBF [26]. The High-Resolution-Beamline (HRB) is a beam line for the SHARAQ spectrometer designed to satisfy the lateral and angular dispersion matching condition [27]. A detailed specification of the SHARAQ spectrometer is described in the Sec. 3.1.3.

The layout of BigRIPS, the High-Resolution-Beamline and the SHARAQ spectrometer is shown in Fig. 3.2. The secondary beam emitted from the production target at F0 is achromatically focused at F3. An aluminum degrader of 15 mm thickness is placed at F1. In order to optimize the momentum acceptance of secondary beam, a collimator is placed at F2. A secondary target is installed at S0, which is the starting point of the SHARAQ spectrometer. The design of ion optics in this experiment is described in Sec. 3.2 in detail.

The secondary ^{8}He beam was produced by a fragmentation reaction at the F0 production target. The primary beam was ^{18}O with an energy of 230 MeV/u. The intensity of the primary ^{18}O beam was about 400 pnA. A production target of ^{9}Be with a thickness of 20 mm was used. An aluminum wedge-shaped energy degrader with a thickness at its center of 8 mm was used.

3.1.3 SHARAQ Spectrometer

The SHARAQ spectrometer is designed to achieve a high momentum resolution of $\delta p/p \sim 1/14700$ and high angular resolution $\delta\theta \sim 1$ mrad for the reaction production from the secondary beam [28, 32].

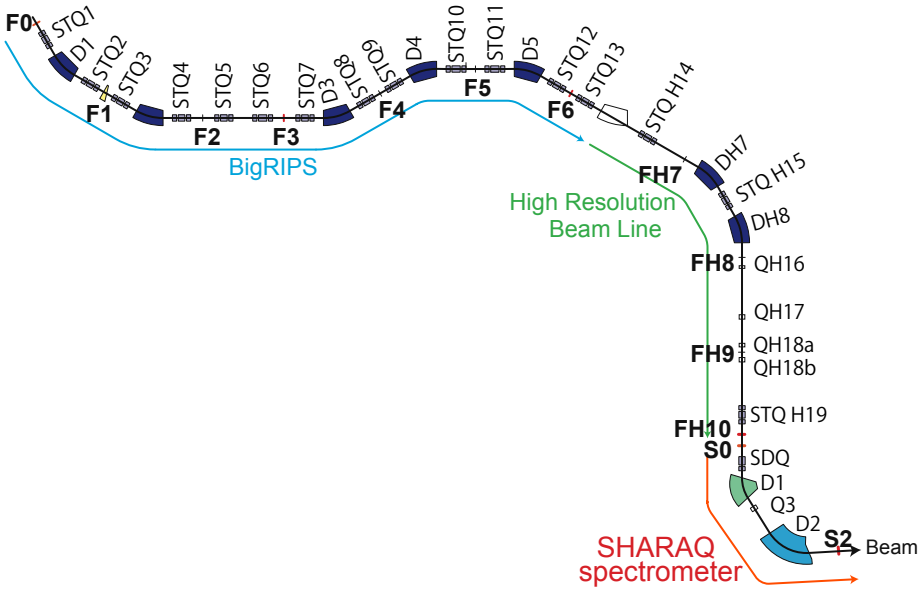

Figure 3.2: Overview of BigRIPS-HRB-SHARAQ.

Figure 3.3 shows the schematic view of the SHARAQ spectrometer. The SHARAQ spectrometer consists of three quadrupole magnets (Q) and two dipole magnets (D) in the following order: Q1-Q2-D1-Q3-D2. The first doublet qudrupoles (SDQ) are superconducting magnets. The design specification of the SHARAQ spectrometer is listed in Table 3.1. The design of the magnet and ion optics is described in Ref. [28] and [33] in detail. The maximum rigidity is 6.5 Tm, which is larger than 4.29 Tm and 5.7 Tm for ^{4}He and ^{8}Li of 200 MeV/u, respectively. The rigidity is smaller than 8.59 Tm for ^{8}He of 200 MeV/u. The ratio of the dispersion (D = 5.86 m) and the horizontal magnification ($M_x = 0.40$) corresponds to spectrometer resolving power of $p/\delta p = D/M_x = 14700$ assuming a target spot size of 1 mm. The infinitely small value of the vertical magnification leads to a high angular resolution from vertical position of final focal plane S2. The ^{8}He beam was stopped at the exit of the D1 magnet by a load beam dump.

3.2 Ion Optics

We used optical parameters which can transport the beam with high resolution achromatically for the BigRIPS-HRB to measure the momentum

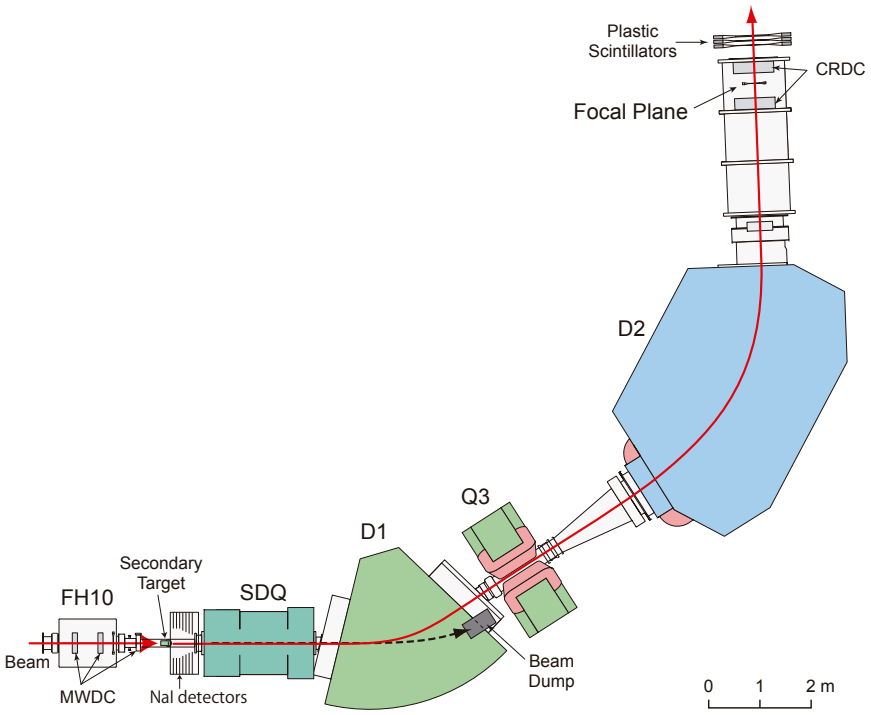

Figure 3.3: Schematic layout of the SHARAQ spectrometer.

Table 3.1: Design specification of the SHARAQ spectrometer.

Maximum rigidity	6.5 (Tm)
Dispersion (D)	5.86 (m)
Horizontal magnification (M_x)	0.40
D/M_x	14.7 (m)
Resolving power (for image size of 1 mm)	14,700
Vertical magnification	0.0
Angular resolution	1 (mrad)
Momentum acceptance	$\pm$1 (%)
Vertical acceptance	$\pm$30 (mrad)
Horizontal acceptance	$\pm$53 (mrad)
Solid angle	4.8 (msr)

of the secondary beam at the F6 dispersive focal plane with a resolution of about $\delta p/p \sim 1/7000$. For the SHARAQ spectrometer, we developed a large momentum acceptance transport to satisfy momentum resolution about $\delta p/p \sim 1/10000$ and as large acceptance for two α particles originated from the ground state of ^{8}Be. Detailed description on the transfer matrix of the ion optics can be found in Appendix A with the definition of the parameters.

3.2.1 High-resolution Achromatic Transport

We used the High-resolution Achromatic Transport (HA) mode for the BigRIPS-HRB to measure the momentum of the secondary beam with $\delta p/p \sim 1/7000$ (FWHM) which corresponds to a 0.46 MeV resolution of missing-mass of four-neutron system. Figure 3.4 shows the envelope of the beams with the HA mode between F3 and S0 with the first order abbreviation optical matrix for ^{8}He of 200 MeV/u. The upper figure shows a horizontal direction for position varied by ± 3 mm and angle by ± 10 mrad. Each color line corresponds to a momentum distribution of ± 1%. The lower figure shows a vertical direction for position ± 3 mm, and for angle ± 30 mrad. In this experiment, the target position (S0) is 20 cm downstream from the standard optics.

Table 3.2 shows a summary of the transfer matrix of the HA mode in the first order. If the beam is achromatic at F3, the ratio of the dispersion ($(x|\delta) = 7.36$ m) to the horizontal magnification ($(x|x) = 0.87$) corresponds to a resolving power of $p/\delta p = (x|\delta)/(x|x) = 10500$, assuming a resolution of 1 mm at F3.

The secondary target is located at S0 which is the achromatic focal plane. The multi-wire drift chambers (MWDCs) were placed at FH9 and FH10 to determine the incident angle and the positions of the beams at the secondary target at S0 with the position resolution of better than 1 mm and the angular resolution of better than 1 mrad. In this experiment, the S0 position is moved 10 cm downstream from the normal HA optics mode as a result of the optimization of the large momentum acceptance mode of the SHARAQ spectrometer.

Table 3.3 summarizes the transfer matrix between FH9 and S0. The position information at FH9 also provides extra information on the beam position at the secondary target because an image of FH9 is symmetric with the image at S0.

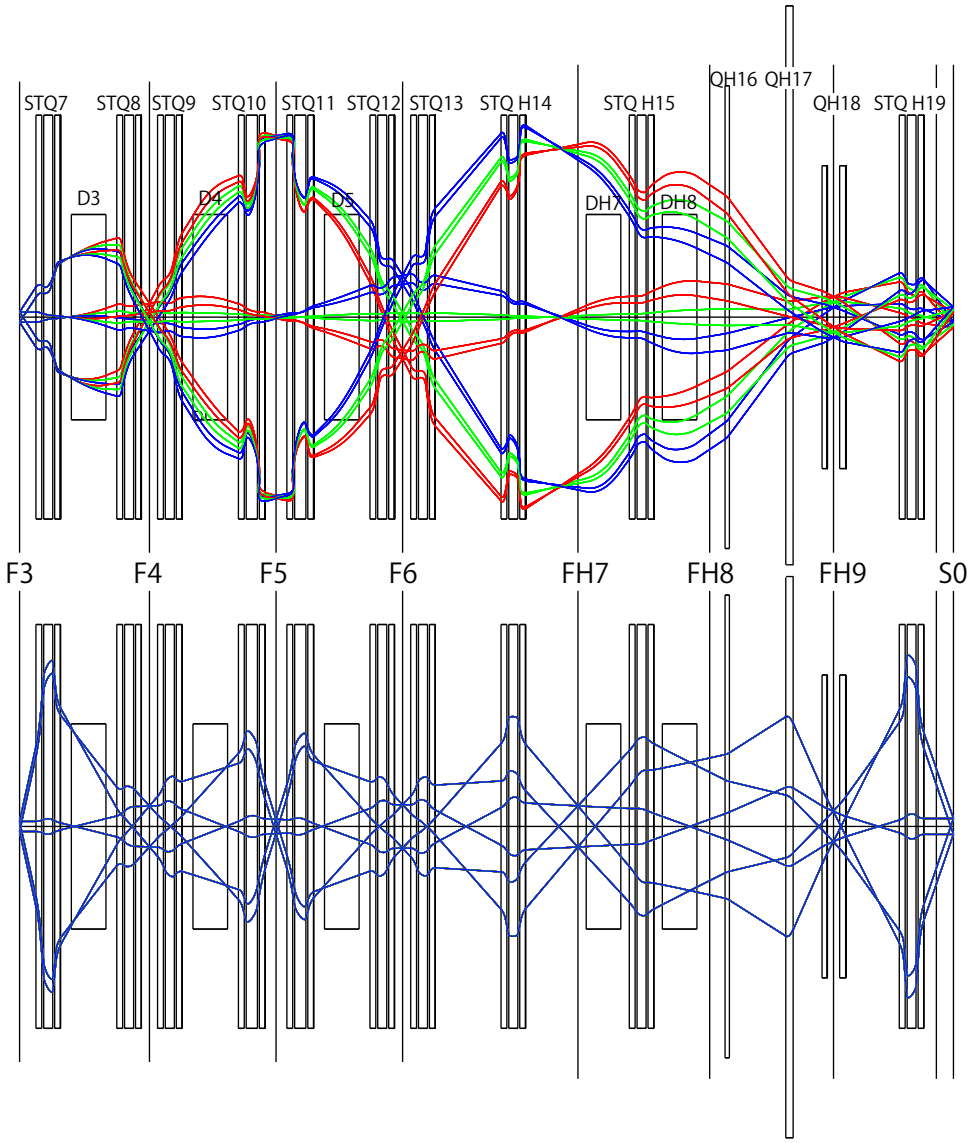

Figure 3.4: The simulated envelope of the ^{8}He beam of 200 MeV/u with the new optics of HA mode between F3 and S0. The upper panel is the horizontal direction, while the lower is the vertical one. Blue, green and red lines indicate the momentum differences of beams by $\pm 1\%$. At S0, the achromatic focus was achieved.

Table 3.2: Transfer matrix of the beam line.

F3-F6					
$(x\|x)$	0.87	$(x\|a)$	0.00	$(x\|\delta)$	7.36
$(a\|x)$	0.03	$(a\|a)$	1.15	$(a\|\delta)$	0.34
$(y\|y)$	-4.30	$(y\|b)$	0.00		
$(b\|y)$	0.00	$(b\|b)$	-0.23		
F3-FH9					
$(x\|x)$	-2.89	$(x\|a)$	0.00	$(x\|\delta)$	-1.01
$(a\|x)$	-0.03	$(a\|a)$	-0.35	$(a\|\delta)$	0.27
$(y\|y)$	-3.10	$(y\|b)$	0.00		
$(b\|y)$	0.81	$(b\|b)$	-0.32		
F3-S0					
$(x\|x)$	1.50	$(x\|a)$	0.00	$(x\|\delta)$	0.52
$(a\|x)$	0.62	$(a\|a)$	0.67	$(a\|\delta)$	-0.33
$(y\|y)$	1.58	$(y\|b)$	0.00		
$(b\|y)$	0.00	$(b\|b)$	0.63		

Table 3.3: Transfer matrix between FH9 and S0.

FH9-S0					
$(x\|x)$	-0.52	$(x\|a)$	0.00	$(x\|\delta)$	0.00
$(a\|x)$	-0.21	$(a\|a)$	-1.93	$(a\|\delta)$	-0.02
$(y\|y)$	-0.51	$(y\|b)$	0.00		
$(b\|y)$	-0.52	$(b\|b)$	-1.96		

3.2.2 Large Momentum Acceptance Transport at the SHARAQ

The original resolution of the SHARAQ spectrometer with the standard optics was 1/14700, which is sufficient for the present experiment. However, the acceptance of the ejectiles was found to be too small for the experiment, so we developed a new transfer matrix with a large momentum acceptance mode and a better acceptance [34].

The momentum distributions of two α particles are within $\pm 0.73\%$ and angular distributions are within ± 0.2 degrees in the laboratory frame for the ground state of ^{8}Be if we choose an incident beam energy of 200 MeV/u. These kinematics enable us to detect two α particles at the same time with the SHARAQ spectrometer. Two α particles from the excited state of ^{8}Be, which satisfy the acceptance are small, since these two α particles have an large opening angle. In addition, in the case of an accidental coincidence of two independent α particles, the position and angle of two particles will have no correlation at the focal plane.

The SHARAQ spectrometer is required to have a momentum acceptance of about $\pm 2.5\%$ to measure the four-neutron system from the ground state to the excited state at 40 MeV and including the momentum distribution of both the two α ($\pm 0.74\%$) and the beam ($\pm 1\%$). A momentum resolution of 1/10000 was also required to achieve the energy resolution of 1 MeV in the invariant mass spectrum. We calculated an ion optical transfer matrix using the code COSY infinity [35] so that the maximum solid angle satisfies those requirements. As shown in Fig. 3.5, we obtained an effective solid angle of 4.2 msr which covers the required momentum area.

Table 3.4 shows a comparison between this optimized large momentum acceptance transport optics and the standard one. The momentum acceptance was 1.8 times larger than the standard optics while the momentum resolution was reduced and the solid angle was almost same as the standard optics. The maximum size of the decay-cone was estimated to be 120 mm in horizontal direction (x direction) and 28 mm in vertical direction (y direction) by a Monte Carlo simulation using the transfer matrix and angular acceptance.

Figure 3.6 shows the large momentum acceptance transport at the SHARAQ spectrometer for ^{4}He of 200 MeV/u. The upper figure shows that for the horizontal direction, the distribution of position is $\pm$ 8 mm and on the angle, it is $\pm$ 1 degrees. Each color line corresponds to a momentum distribution of $\pm$ 1%. The lower figure shows that for the vertical direction, the distribution of position is $\pm$ 8 mm on the angle, it is $\pm$ 1 degrees.

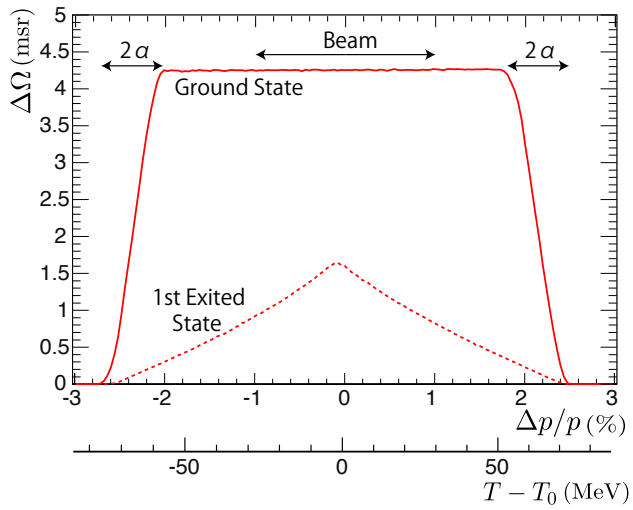

Figure 3.5: Effective solid angle of ^{8}Be. The solid line represents ground state of ^{8}Be and the dotted line for the first excited state (3.0 MeV)

Table 3.4: Comparison of the specifications for large momentum acceptance transport of SHARAQ to that of the standard transport.

	large moment. accept.	standard
Momentum resolution ($p/\delta p$)	10000	14700
Momentum acceptance	±1.8%	± 1.0%
Vertical acceptance	±1.5 deg.	±1.7 deg.
Horizontal acceptance	±2.9 deg.	±3.0 deg.
Solid angle	4.3 msr	4.8 msr

Table 3.5: Parameters of the transfer matrix of the SHARAQ spectrometer.

S0-S2					
$(x\|x)$	-0.58	$(x\|a)$	0.00	$(x\|\delta)$	-6.08
$(a\|x)$	-0.51	$(a\|a)$	-1.72	$(a\|\delta)$	0.62
$(y\|y)$	0.00	$(y\|b)$	-2.02		
$(b\|y)$	0.50	$(b\|b)$	-0.25		

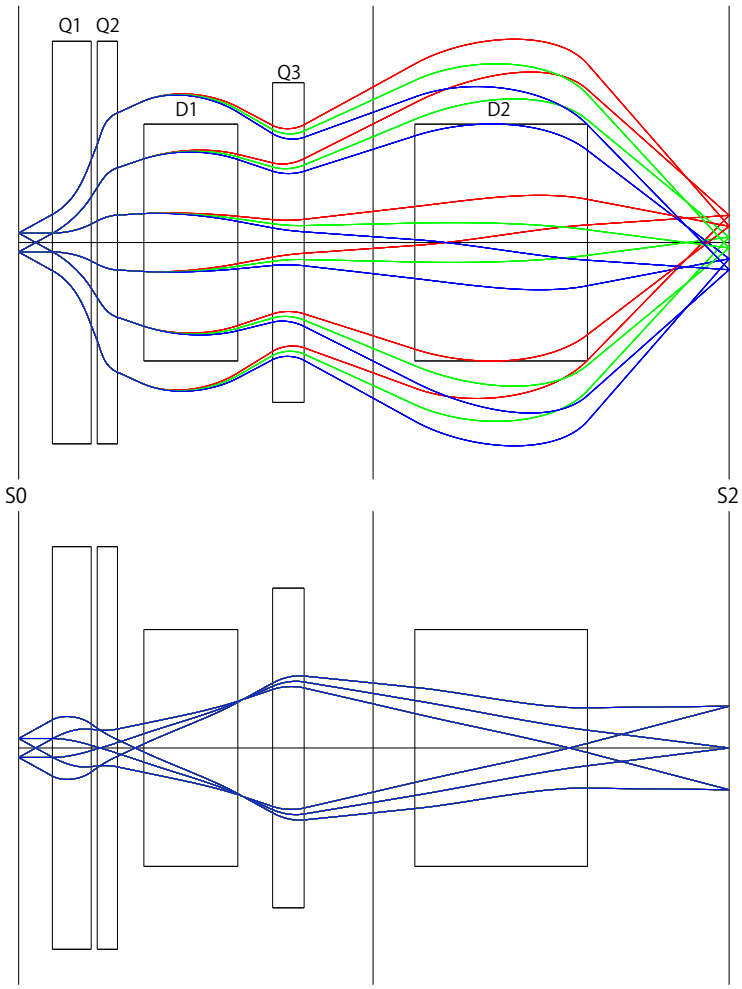

Figure 3.6: The envelope of the large momentum acceptance transport at the SHARAQ spectrometer for ^{4}He of 200 MeV/u.

3.3 Detectors

Table 3.6 lists the detectors used in this experiment at the BigRIPS-HRB-SHARAQ. Each of the detectors are described in detail in the following sections. The beam line detectors which are located from F3 to FH10 are described in Sec. 3.3.1. The final focal plane detectors which are located at S2 are described in Sec. 3.3.2.

Table 3.6: List of the detectors used in the present experiment.

Focal plane	Detector	Type	Name	Sensitive area $X \times Y$ mm	Used during physics runs
F3	Plastic	1 mm^{t}	F3PL	100 × 100	○
	Hodoscope	1 mm^{t}	μHodo	100 × 100	○
	LP-MWDC	T20	DC31	80 × 80	
	LP-MWDC	T21	DC32	80 × 80	
F6	LP-MWDC	S22	DC61	144 × 144	○
FH7	Plastic	3 mm^{t}	FH7PL	220 × 150	
	LP-MWDC	S20	DC61	144 × 144	
FH9	Plastic	1 mm^{t}	FH9PL	220 × 150	○
	LP-MWDC	S20	DC91	144 × 144	○
FH10	LP-MWDC	S21	DCX1	144 × 144	○
	LP-MWDC	S21	DCX2	144 × 144	○
	Plastic	1 mm^{t}	FHXPL	220 × 150	○
	LP-MWDC	S23	DCX0	96 × 96	○
S2	CRDC		CRDC1	550 × 300	○
	Plastic	10 mm^{t}	S2L0	200 × 100	
	CRDC		CRDC2	550 × 300	○
	Plastic	5 mm^{t}	S2L1	650 × 400	○
	Plastic	10 mm^{t}	S2L2	650 × 400	○
	Plastic	20 mm^{t}	S2L3	650 × 400	○

3.3.1 Beam Line Detectors

Plastic Scintillators

Four plastic scintillators were used in this experiment to detect the timing and the energy loss of the beam and to count the number of particles. The

light output from each scintillator was read by two photomultiplier tubes (PMTs) attached to the both sides of the scintillator. The PMTs used in this experiment were Hamamatsu R7600s.

Low Pressure Multi-Wire Drift Chamber

Eight low pressure multi-wire drift chambers (LP-MWDCs) were used in this experiment to track the position of the beam. The details of the LP-MWDCs are described in Ref. [36] and Ref. [37]. Figure 3.7 shows the schematic picture of a LP-MWDC. Table 3.7 shows the summary of specification of MWDCs. The data reduction of MWDCs is given in Sec. 4.2.1. This section gives a specific design and configuration of three type of LP-MWDCs which categorized by a plane configuration.

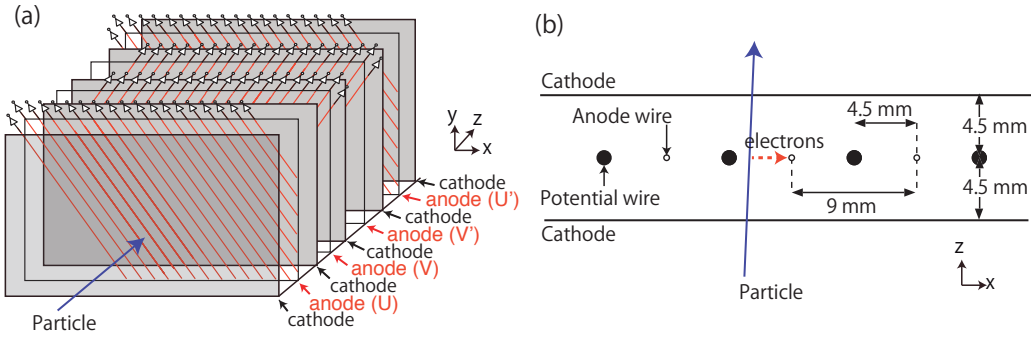

Figure 3.7: A schematic picture of a MWDC. (a) The plane configuration of S23 type. (b) A cross sectional picture of MWDC between anode and cathode plane of S23 type.

There are several different types of MWDCs used in this experiment. Their purposes are as follows:

- The T20, T21, S23 types are designed for use near the achromatic focal plane where the size of the beam spot is small. The cell size is small to detect as many as 10^5 particles/sec in each cell.
- The S22 type is designed for the use at a dispersive focal plane where the size of the beam spot is large. The effective area and cell size are large. The plane configuration of this type of MWDC is two pairs of planes such as U-U′ and V-V′. The V(U) plane is in the same direction of wire as the V′(U′) plane. The V(U) plane is shifted to the half cell size to the V′(U′) plane. This configuration is useful to identify and track two particles described in Sec. 4.4.2.

- The S20, S21 types are designed for the use at FH7, FH9 and FH10. These types each consist of three planes.

These MWDCs were filled with 10 kPa pure of isobutane gas and operated with a bias of 1–2 kV. The detectors were then installed in the vacuum chamber. Aluminized mylar with a thickness of 25 or 50 μm was used as a window for the detector. The signals from the anode wires were amplified and discriminated by REPIC RPA-130/131 cards and the timings for leading and trailing edge were digitized by a multi-hit TDC module CAEN V1190A/B. The position resolution of less than 300 μm (FWHM) and detection efficiencies of more than 90% were obtained in an experiment using the light ion beam with an intensity of around 10^5 cps [36].

Table 3.7: Specification of the low pressure multi-wire drift chamber.

Name	DC31	DC32	DC61	DC71 DC72 DC91	DCX1 DCX2	DCX0
Type	T20	T21	S22	S20	S21	S23
Configuration	(XX′YY′)^2	XX′YY′	VUU′V′	XUY	XYV	XX′YY′
Sensitive area	80×80 mm^2		144×144 mm^2			96×96 mm^2
Cell size	5×4.8 mm^2		9×9 mm^2			6×6 mm^2
#ch	16×8	16×4	24×4	24+24+6		16×4
Anode wire	Au-W 12.5 μm$^{\phi}$		Au-W 10.0 μm$^{\phi}$			
Potential wire	Cu-W 75 μm$^{\phi}$					
Cathode foil	Mayler 1.5 μm$^{\mathrm{t}}$					
Window foil	50 μm$^{\mathrm{t}}$		25 μm$^{\mathrm{t}}$			
Voltage	-1. $\sim$ -2. kV					
Gas fill	pure isobutane (i-C_4H_{10}), 10 kPa					

Micro-Hodoscope

A micro-hodoscope consists of thirty plastic scintillator bars with horizontal and vertical dimensions respectively. Each plastic scintillators are the size of 1 mm × 1 mm × 30 mm as shown in Fig. 3.8.

It was crucial to detect the position of the particles using MWDCs with a high beam rate ($\sim 10^6$ cps) and a narrow beam spot (10 mm diameter) since charged particles only come in one or two cells. In this experiment,

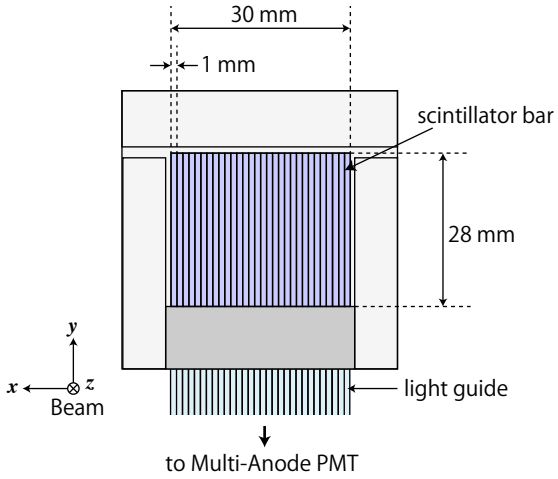

Figure 3.8: Schematic picture of micro-hodoscope.

we developed the micro-hodoscope used at the achromatic F3 focal plane described in Sec. 3.2. By using a micro-hodoscope, it is possible to detect the position of charged particles with a resolution of 1 mm (FWHM) under high intensity irradiation in a narrow region. If we can identify the scintillator bar which is fired by a particle, the position resolution of 0.68 mm ($= 1$ mm$\times 2.35 \times 1/\sqrt{12}$) (FWHM) is obtained. The efficiency is almost 100% for charged particles. The detail of the micro-hodoscope is described in Ref. [38, 39].

Figure 3.9 shows the position of micro-hodoscope and other detectors in the F3 chamber. The plastic scintillator (F3PL) and micro-hodoscope were located upstream of the F3 focal plane. The MWDC (DC31) was located on the F3 focal plane and MWDC (DC32) was downstream.

In order to minimize dead space, bulk scintillator bars were used without any light shield. The light emitted from each scintillator bar was transmitted using optical fibers. We used a 64 channel multi-anode photo-multiplier H7546B (Hamamatsu) for the conversion and amplification of signals. The signals from the PMTs were amplified and discriminated by REPIC RPA-130/131 cards, and the timing for leading and trailing edge was digitized by multi-hit TDC module CAEN V1190A/B. A detection efficiency of 95% was obtained in previous experiment [38]. The data reduction of the micro-hodoscope is given in Sec 4.2.2 in the following chapter.

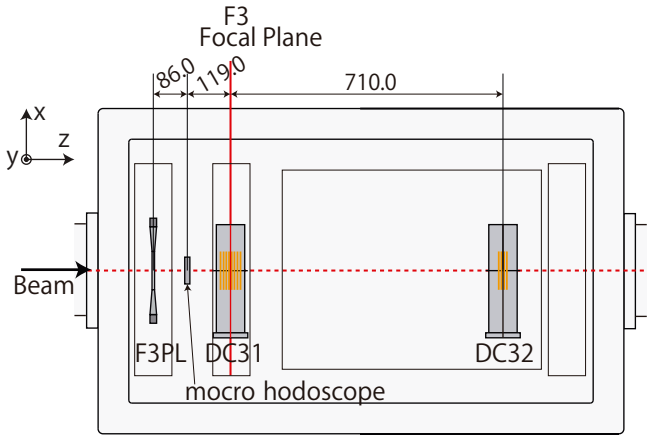

Figure 3.9: Top view of the F3 chamber.

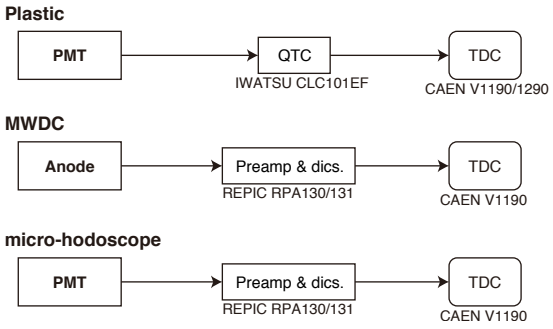

Figure 3.10: Circuits of beam line detectors.

3.3.2 Final Focal Plane Detectors

The final focal plane detectors consist of four plastic scintillators and two cathode readout drift chambers (CRDCs) [40, 41] in the S2 focal plane of the SHARAQ spectrometer. To cover the maximum size of the decay-cone sufficiently, we used the present CRDC which has a large effective area ($x =$ 550 mm, $y = 300$ mm) and no dead-space. The layout of the S2 focal plane is shown in Fig. 3.11.

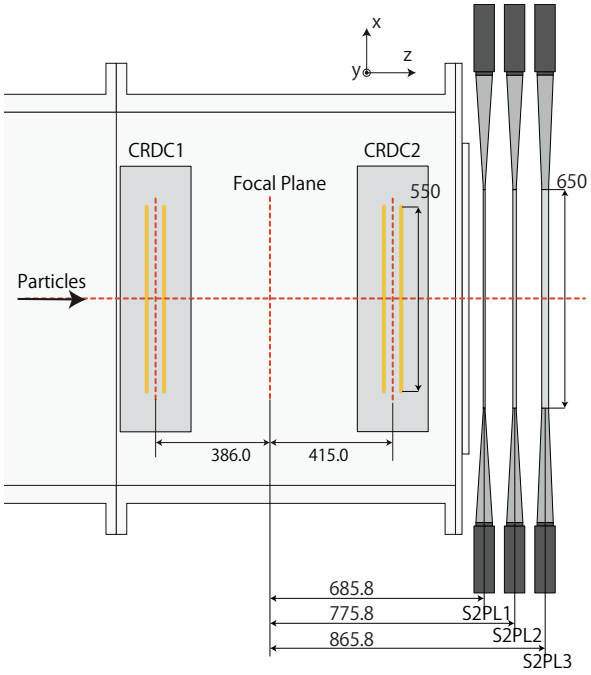

Figure 3.11: Top view of the S2 focal plane.

Plastic Scintillators

There were three plain plastic scintillators and one slitted plastic scintillator used in this experiment. The three plastic scintillators were downstream of the S2 focal plane for trigger generation and for the identification of the reaction products. Table 3.8 shows the specifications for each of the three plastic scintillators. The light output from each scintillator was observed by two PMTs (Hamamatsu H1161) attached to each side of the scintillator. The signals from the PMTs were discriminated and changed to logic signals whose width is in proportion of the charge by the Iwatsu CLC101EF charge-to-time

converter (QTC). The leading and trailing edges of those logic signals were digitized by the multi-hit TDC module CAEN V1290N.

Table 3.8: Specification of plastic scintillators at the final focal plane.

Name	S2PL1	S2PL2	S2PL3
Area		650 × 400 mm^2	
Thickness	5 mm	10 mm	20 mm
Material		EJ-200	
PMT		H1161	

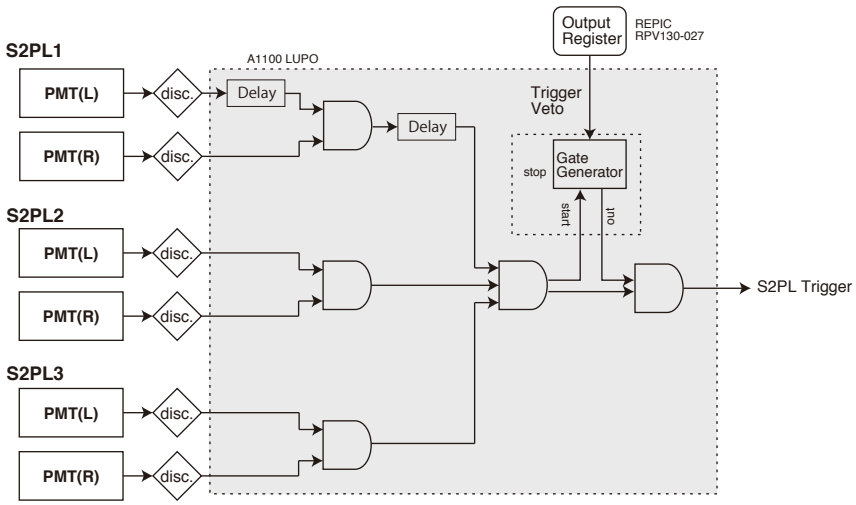

Figure 3.12: Schematic view of the CRDCs.

The plastic scintillator S2PL0 was designed for calibration of the vertical position of CRDCs. Data reduction of the calibration is described in Sec. 4.2.3. Figure 3.13 shows this plastic scintillator. This scintillator has 9 slits, each with a width of 0.2 mm placed at 10 mm intervals. The thickness of this scintillator is 10 mm. The light output from each scintillator was observed by two PMTs (Hamamatsu R7600) attached to both sides of the scintillator. The signals from the PMTs were discriminated by the LeCroy 623B and the timing was digitized by the multi-hit TDC module CAEN V1290N.

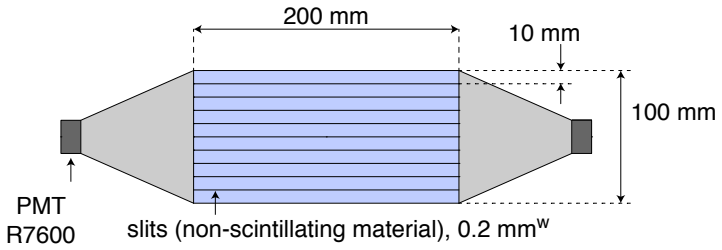

Figure 3.13: The plastic scintillator S2PL0 used for the calibration of the vertical position of the CRDCs.

Cathode Readout Drift Chamber

Two CRDCs were used at the S2 focal plane. The detail of of the CRDCs are described in Ref. [40].

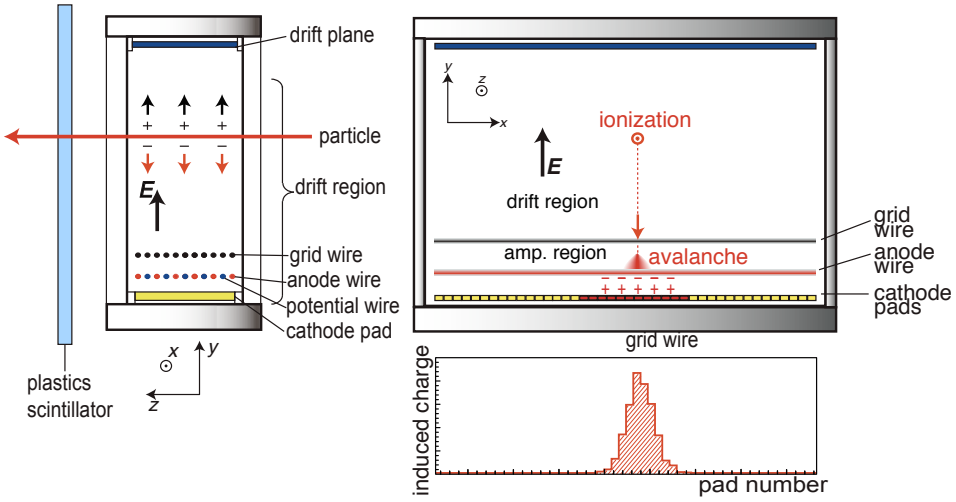

Figure 3.14: Schematic view of the CRDCs.

The CRDC is designed for measuring positions and angles of particles at the S2 focal plane. The SHARAQ, as described before, was designed to have a resolving power of $\delta p/p = 1/10000$ for a 1 mm-large target spot. Because of the dispersion, $(x|\delta)_{\rm SH} = 60$ mm/%, in order to satisfy this requirement, the CRDCs have position resolutions of better than 0.6 mm and must be operated with a low-gas pressure to suppress divergence by the multiple scattering.

In this experiment and its goal of measuring a two-particle system, it was especially important that the CRDCs had a large area and lacked dead-space.

Figure. 3.14 shows a schematic view of the principle for the position detection of charged particles in the CRDC. When a charged particle goes through the focal plane, gas inside of the CRDC chamber is ionized and the particle hits the plastic scintillator downstream of the CRDCs. Then, the electrons drift along in the vertical direction and make an avalanche near the anode wire. The vertical position of the charged particle is determined by measuring the drift time of electrons in the drift plane. The horizontal position is determined by measuring the center of the distribution of induced charges on the cathode pads which are arranged at 2 mm intervals.

Table 3.9: Specification of the cathode readout drift chamber

Sensitive area	550 × 300 mm^2
Cathode pad	51 × 2 mm^2 , 256 pads × 2 plane
Anode wire	10 wires, Au-W 20 μm^{ϕ}
Potential wire	11 wires, Au-W 50 μm^{ϕ}
Frisch grid wire	52 wires, Au-W 50 μm^{ϕ}
Grid - anode distance	7 mm
Anode - cathode distance	3 mm
Repartition grid	Au(15 nm)-PET 2.5 μm
Window foil	PET 25 μm
Gass fill	pure isobutane(i-C_4H_{10}), 30 Torr = 4 kPa
Drift voltage	$\sim$ -4 kV
Anode voltage	$\sim$ -1 kV

Table 3.9 shows the specification of CRDCs. The signals from anode wires were amplified and shaped with Timing-Filter-Amp (TFA) ORTEC 571/671. Output signals from the TFA were digitized by the multi-hit TDC CAEN V1190 and flash-ADC (FADC) SIS3310. The charge signal induced at the cathode pads are amplified and held in the capacitor in the GASSIPLEX chips. The trigger signals (Track and Hold, T/H) to hold the charge in the GASSIPLEX chips are generated by the anode signal. After that, the charge held in the GASSIPLEX chips were each read out with the CAEN Readout for Analog Multiplexed Signals V550 and CAEN Sequencer V551B. With its high multiplexing capability, the charge signals from the 256 cathode pads can be transmitted through a single signal line. Figure 3.15 shows the circuit of the CRDCs and timing chart of the readout system. The details

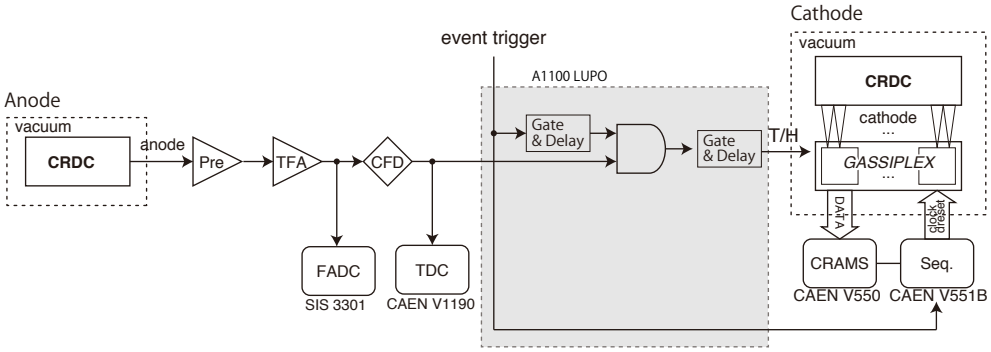

Figure 3.15: Circuit of the CRDC.

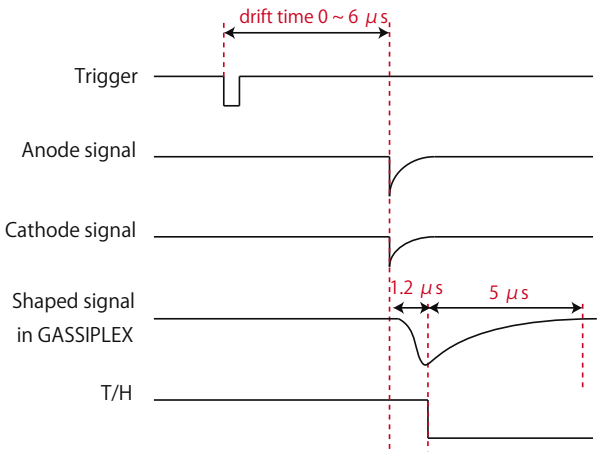

Figure 3.16: Timing chart of the CRDC circuit.

of those systems is provided in Ref. [40]. The drift time was 19.0 ns/mm at the pressure of 30 Torr. The position resolutions were 380 μm (FWHM) horizontal and 340 μm (FWHM) vertical in the previous experiment [41].

Detection System for ^{4}He(^{8}He,^{8}Be)4n Reaction

In this experiment, we used CRDCs as the two particle tracking detectors [42]. If two α particles were injected to the CRDCs, the T/H signals are generated by the anode signal when the first particle reached to anode wire. The second particle should reach the anode wire within 500 ns after the arrival of the first α particle, if they are from the ground state of ^{8}Be. Because the decay constant of the shaped signal in the GASSIPLEX (Fig. 3.16) is about 5 μs, which is much longer than the drift time difference of the two α particles from the ground state of the ^{8}Be, it is possible to read out signals for each α particle. The vertical positions of the two particles can be detected to obtain the pulse shape of the charge at the anode wire using flash-ADC SIS3301. The data reduction of CRDCs is given in Sec 4.2.3 of the following chapter.

FPGA-Based Circuit: LUPO

We used an FPGA-based circuit named LUPO (Logic Unit for Programmable Operation) as the trigger logic [42]. LUPO is a VME module with FPGA chips and has the interface of the FPGA and the VME bus. This module allows us to easily control and develop a complicated circuit by changing its logic structure and other related parameters remotely by changing the VME driver settings with networked computer. In addition, a single VME module, LUPO can replace many standard NIM modules.

The CRDC trigger module is mainly consists of two sections. As shown in Fig. 3.15, LUPO was used for the selection of the triggers for the CRDCs. The CRDC trigger condition can be selected by:

- coincidence signal of the plastic scintillator,
- the anode signal and
- the 100 Hz clock signal.

This system allows us to test the CRDC system. Once the local trigger signal is created, it is sent to the general trigger selector which can be selected for the local trigger or another one as the general trigger of the whole SHARAQ DAQ system. The whole DAQ system is described in Sec. 3.5.

3.4 Target

At the S0 focal plane, we used liquid helium as the secondary target for production of the four-neutron system. Considering the yield of four-neutron system and multiple scattering of particles, we used about 123 mg/cm^2 thickness with 6 μm haver foil [43].

3.4.1 Liquid Helium Target

We used a liquid helium target with a cryogenic system named CRYPTA [30], which was developed by RIKEN. It was installed from the upper side of the target chamber and could be removed from the target position while keeping the system under vacuum. The CRYPTA system is a compact liquid helium target for radioisotope beam experiments at RIKEN with a Gifford-McMahon cycle refrigerator. The schematic view of the CRYPTA system is shown in Fig. 3.17.

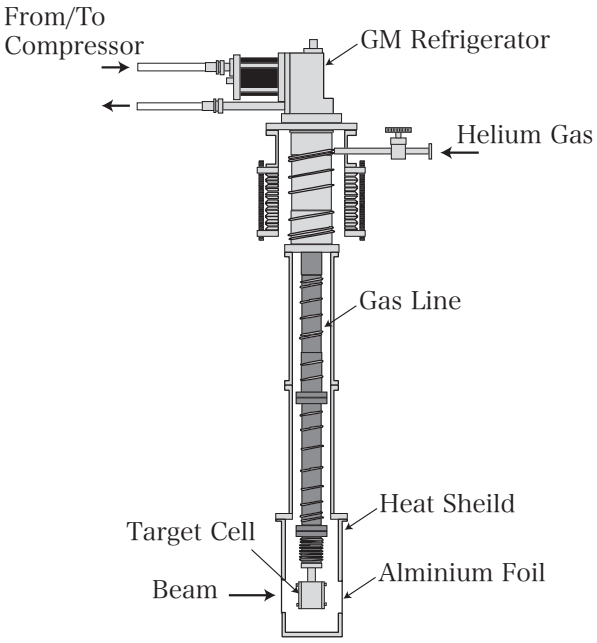

Figure 3.17: Schematic view of the CRYPTA.

Table 3.10 presents basic properties of 4-helium. In order to reach a temperature less than its boiling point of 4.2 K, it was necessary to use the heat shield, which protects from the radiant heat from the environment.

Each window for the beam was covered with an aluminum foil 6 μm thick to reduce multiple scattering of the beam. The angle straggling of the α particle of 200 MeV/u is 0.11 mrad, which was small enough in this experiment. It was necessary to select an opaque material for the heat shield window foil.

Table 3.10: Basic properties of 4-helium.

Atomic weight	Boiling point	Liquid density @ 1 atm	Gas density @ 1 atm, 0 °C
4.003	4.215 K	0.125 g/cm^3	0.179 g/l

The target cell has a window with a 30 mm diameter made of 6 μmHavar foil [43]. The thickness of the target cell is 8 mm. A thermometer is used to monitor the temperature of the cell. Front and cross views of the target cell are shown in Fig. 3.18. We chose 6 μm-thick Havar foils ($Co_{42}Cr_{20}Ni_{13}Fe_{19}W_1$) [43] as windows of the target cell since this foil can withstand the pressure difference of an atmosphere and a temperature below a boiling point of helium. Figure 3.19 shows the measurement of laser displacement sensor where the differential pressure is set to 1 atm. These data were fitted with a quadratic function [44] of the following form:

$$z = d\left\{1 - \left(\frac{x}{r}\right)^2\right\} \tag{3.1}$$

where x and z stand for the radial and thick displacements in same coordinate system, r is radius of the window ($r = 15$ mm), and d is the deduced deflection of the foil. We determined $d = 0.901$ mm.

A effective target thickness was therefore estimated to be 9.8 mm which corresponds to 123.38 mg/cm^2 including the effect of the bulge of the window foils.

3.5 Data Acquisition

3.5.1 Data Acquisition System

The data acquisition was performed by the RIBF DAQ system [45]. This system was designed to perform network-distributed data processing, hierarchical event building and parallel readout. This system is versatile and scalable so the whole DAQ system can be divided into a sub-DAQ system for

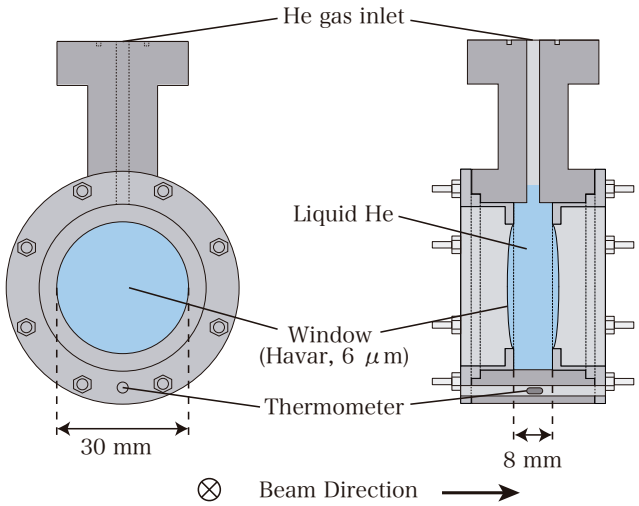

Figure 3.18: Front and cross views of the target cell.

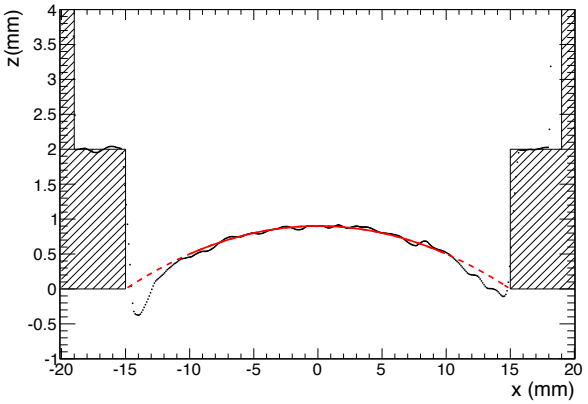

Figure 3.19: Measurement of leaser displacement sensor of the bulge of the target foil.

each detector segment. Each sub-DAQ system builds the events in parallel locally.

In this experiment, we placed a sub-DAQ system at each focal plane. Signals from the detectors were processed by the NIM and VME modules. In response to a common trigger, the data from the VME modules were assembled by the front-end computers, VMIVME7807, into an event fragment. Each part of an event was sent to the event building server and integrated by it into a complete event.

3.5.2 Trigger Logic

The data of each part of an event were integrated into a event building server synchronized and with a common trigger. The triggers were selected with a trigger selector on the Generic Trigger Operator (GTO) module.

We defined the following trigger conditions for an event:

- A hit to the plastic scintillator F3PL at F3 (the F3 trigger).
- A hit to the plastic scintillator FH10PL at FH10 (the FH10 trigger).
- A downscaling of the FH10 trigger (the FH10 downscale trigger).
- Hits to the plastic scintillators S2PL1, 2 and 3 (the S2 trigger).

A common trigger could be selected from these signals. The "or" logic of these signals was also able to be selected as the common trigger.

As summarized in following section (Sec. 3.6), we used the F3, FH10 and S2 triggers in the optics tuning. The F3 and FH10 triggers were used to obtain unbiased beam data. FH10 downscale trigger was with a reduced trigger rate by a factor of 1/100,000 using the latch module in order to monitor the beam with low trigger rate.

In the physics measurements which achieve a 10^6 cps beam at the secondary target, the F3 trigger rate was more than 10^6 cps and the S2 trigger rate was about a few 100 cps. The trigger rate in the physics measurement was restricted by a large dead time of the CRDCs cathode readout of about 2 μs.

3.6 Summary of the Measurement

A summary of all the measurement conditions is in Table 3.11.

We used ^{4}He and ^{8}Li beams to tune the transportation of the SHARAQ spectrometer. A ^{8}He beam was used to tune the transportation of the

beam line. During the physics measurement, we employed the setting of the SHARAQ spectrometer used for the ^{8}Li and ^{8}Be. The ^{8}Be setting was used to measure the ^{4}He(^{8}He,^{8}Be)4n reaction while the ^{8}Li setting was used for the calibration of the excitation energy of the four-neutron system and for another experiment to analyze the channel of the single charge exchange reaction p(^{8}He,^{8}Li)n. This channel will be summarized in a future publication.

Table 3.11: List of the measurement conditions.

Run	Magnet setting		Beam intensity	Secondary target	Trigger conditions
	Beam Line	SHARAQ			
Optics tuning	^{4}He	^{4}He	$\sim 10^{4}$ cps	–	F3, FH10, S2
	^{8}Li	^{8}Li			
	^{8}He	–			
Physics measurement	^{8}He	^{8}Li	$\sim 10^{6}$ cps	liq.He	S2$\oplus$FH10/n
	^{8}He	^{8}Be			

In the optics turing, the beam intensity was on the order of 10^{4} cps. In order to tune the transport between the beam line and the SHARAQ spectrometer, there was no secondary target. The trigger was selected from the signal of the plastic scintillator at F3, FH10 and S2.

In the physics measurement, the beam intensity was about 2×10^{6} cps at the secondary target, where the liquid helium target was used. The trigger condition was the "or" logic of S2 trigger and FH10 downscale trigger.

Chapter 4

Data Reduction

This chapter gives a description of the analysis to select the reaction events of ^{4}He(^{8}He,^{8}Be)4n reaction and to determine the mass of tetra-neutron system by missing-mass spectroscopy. Sec. 4.1 gives the event-by-event analysis of the intense beam. Sec. 4.2 describes how to resolve the trajectories of the beam and reaction products. The ion optical analysis including higher-order aberration and estimation of the energy resolution is described in Sec. 4.3. The selection method of four-neutron events is described in Sec. 4.4. The reconstruction of the four-neutron missing-mass spectrum from these selected events is described in Sec. 4.5. Finally, a background estimate of the obtained spectrum is described in Sec. 4.6.

Especially for detecting small statistical events, it is important to resolve ^{8}He beam under very intense beam condition (Sec. 4.4.2) and to detect two α particles at the final focal plane of the SHARAQ spectrometer (Sec. 4.4.4).

4.1 Analytical Framework for Intense Beam

In this experiment, it was important to achieve an intense beam and a good signal-to-noise ratio since the reaction cross section was expected to have a small. Here, we use the term *triggered bunch* to mean the bunch containing the particle which makes the trigger. Refer to Fig. 4.1 for a schematic representation of these terms.

The typical ^{8}He beam intensity in this experiment was 2×10^{6} particle/sec, which was provided at a frequency of 13.7 MHz. Accordingly, the secondary beam of ^{8}He had a bunch structure with a period of 73.0 ns, 7% of the beam the bunches contained more than two ^{8}He particles from the 2×10^{6} particle/sec beam. Figure 4.2 shows the relation between the occupation ratio of beam bunches and the beam intensity. The solid blue and red

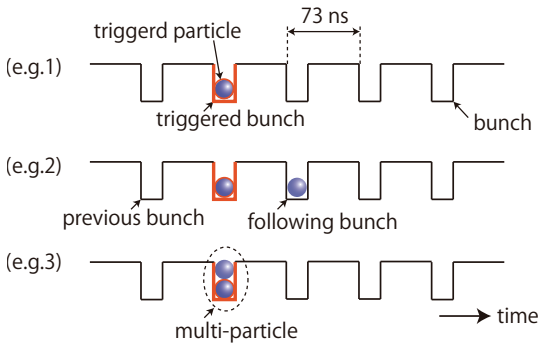

Figure 4.1: The schematic illustrating the bunch structure of the beam and the definition of terms in this thesis.

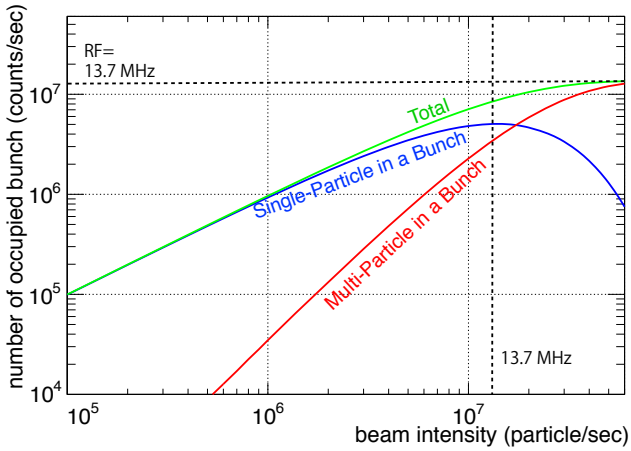

Figure 4.2: The occupation ratio of the beam bunch as a function of the beam intensity. The solid blue and red lines represent the number of bunches occupied by single and multiple particles, respectively. The solid green line represents the total number of bunch occupied particle. The dashed lines represent a frequency of 13.7 MHz, which is the RF of the cyclotron.

lines represent the number of bunch occupied by single and multiple particle bunches, respectively. The solid green line represents the total number of bunches which occupied with more than one particle. The number of single-particle in a bunch was maximized at 13.7 MHz. At intensity higher than 13.7 MHz, the majority of bunches are occupied by multiple particle.

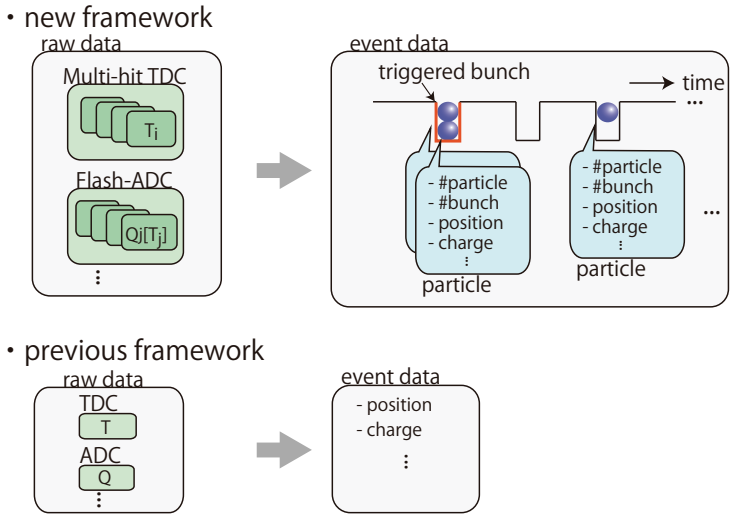

Figure 4.3: A schematic diagram of the analysis framework.

In order to obtain event-by-event information with such a high intensity beam, we used multi-hit TDCs for the beam line detectors. Here, we describe how to analyze timing information from the multi-hit TDC.

For treating multi-particle bunches under high intensity beam, we developed a new analytical framework. In this framework, the information on the timing of multi-particle bunches includes the bunch structure as a new parameters. We used *artemis* [46], which is a ROOT [47] based toolkits, to analyze the data from the DAQ system. As illustrated in Fig. 4.3, we assigned the number of particles and bunches for each event by reading the multi-hit TDCs of the plastic scintillators at FH10. We describe the analysis required to resolve the trajectories of the individual particle in detail in Sec. 4.4.2.

4.2 Trajectory Reconstruction of the Beam

4.2.1 Tracking by using MWDCs

Calibration of the Drift Time to Distance

To determine the positions hit on the MWDC, we calculated the relation between drift time and distance. First, we determined the timing of the plastic scintillator at FH10, which were used as the reference time for the MWDC drift time. Then we selected the timing of the signals of the anode wires. Here, we analyze the MWDC at F6, which has a simple plane configuration (DC6: type S22) in order to properly treat the multi-particle bunch (see Sec. 4.4.2). Here, we describe how to analyze to the DC6, while the analysis of the other type of MWDCs was almost the same. An analysis of the other MWDCs which have a different plane configuration is given by Ref. [37].

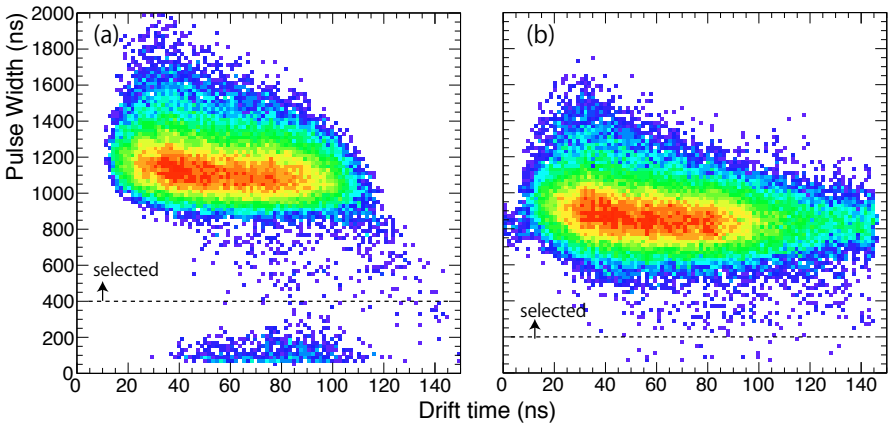

Figure 4.4: Drift time versus pulse width for the MWDC at F6 for (a) a low intensity beam ($\sim 10^4$ cps) and (b) high intensity beam ($\sim 10^6$ cps). The events were selected over a threshold (dashed line) in order to reject the δ-rays.

Figure 4.4 (a) shows the relationship between drift time and pulse width of the MWDC at F6 in a low-rate condition while Fig. 4.4 (b) shows this relationship under high-rate condition. When a particle passes through the counter gas, it creates δ-rays which are electrons with relatively high energies. These δ-rays produce small pulse signals in wires, which are different from the hit position of the particle. In order to discriminate the δ-ray signals, we set a minimum threshold for the pulse width and used the pulse height

over this threshold. The pulse width became smaller with the high intensity beam because of insufficiency of the filled gas.

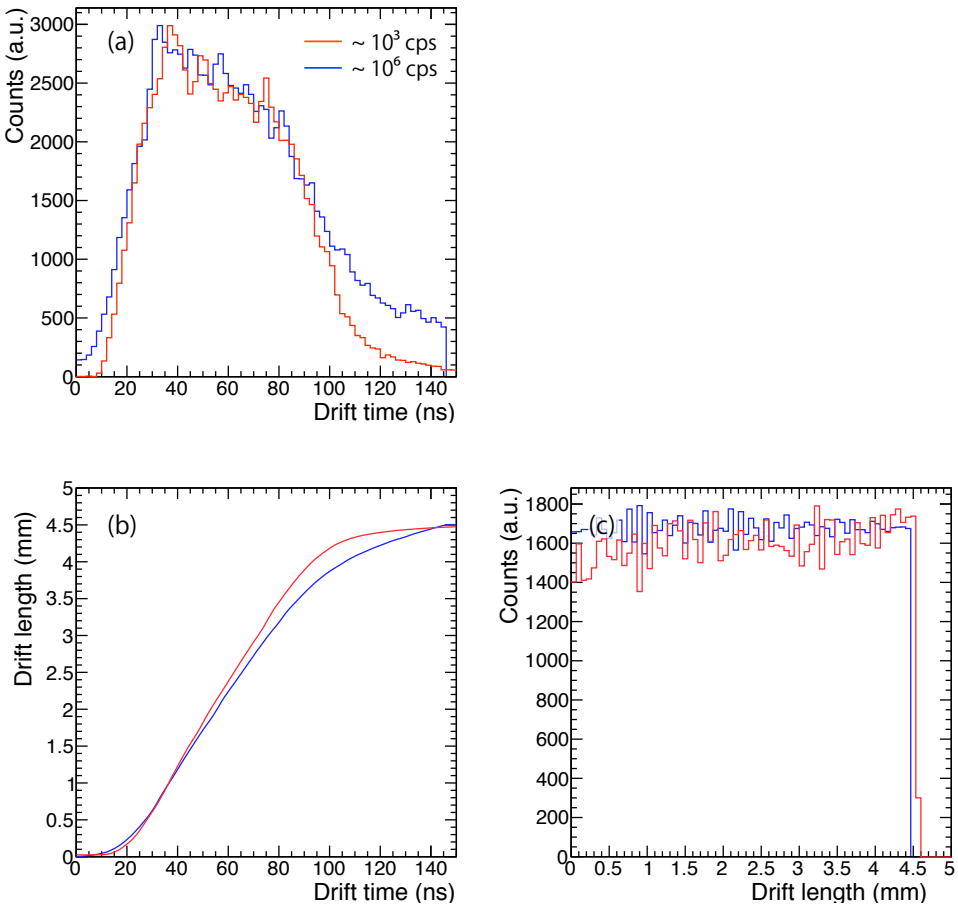

Figure 4.5: Calibration of drift time to length for MWDCs. (a) Distribution of the drift time, (b) the function for converting the drift time into length, and (c) the distribution of the length. The red and blue spectra correspond to the data at low intensity and high intensity beam respectively.

We deduced the relationship between the drift time distribution and the pulse width using a beam with a flat distribution. Then we calibrated the data using a data set from the low intensity beam condition ($\sim 10^3$ cps) for the optics analysis and one of a data set from high intensity condition ($\sim 10^6$ cps) for physics run. The function between the drift time and the length

$(l(t))$ was

$$l(t) = \int v(t)dt \tag{4.1}$$

$$= \frac{L_{\rm wire}}{N}\int \frac{dN}{dt}dt, \tag{4.2}$$

where $v(t)$ is the velocity of the electrons, N is total number of events and $x_{\rm cell}$ is distance between anode wires. The drift time distribution was mapped onto the drift distance distribution so that the resulting drift distance spectrum became uniform. Figure 4.5(b) shows the calibration curve of the drift time (Fig. 4.5(a)) to distance (Fig. 4.5(c)).

Determination of the Hit Position

We determine the left-right ambiguity of the drift length from the anode wire by using the other plane of them. An example illustrating the determination of the hit position on the F6 MWDC with a UU′VV′ plane configuration (see Sec. 3.3.1) is illustrated in Fig. 4.6. The average positions of U plane ($\bar{u}$) and V plane ($\bar{v}$) in the UV plane are described by:

$$\bar{u} = \frac{u+u'}{2}, \tag{4.3}$$

$$\bar{v} = \frac{v+v'}{2}. \tag{4.4}$$

The position of the beam in x and y coordinates was determined as the cross point of the U plane and V plane using

$$x(\bar{u},\bar{v}) = \frac{-\bar{u}\sin\theta_{\rm V}+\bar{v}\sin\theta_{\rm U}}{\sin(\theta_{\rm U}-\theta_{\rm V})}, \tag{4.5}$$

$$y(\bar{u},\bar{v}) = \frac{\bar{u}\cos\theta_{\rm V}-\bar{v}\cos\theta_{\rm U}}{\sin(\theta_{\rm U}-\theta_{\rm V})}, \tag{4.6}$$

where the $\theta_{\rm U}$ and $\theta_{\rm V}$ were 60 ° and -60 ° respectively.

Once again, we refer to Ref. [37] for a full description of the determination of the hit positions for MWDCs of the other plane configuration (XUV).

Position Resolution and Efficiency

From the Eqs. (4.5) and (4.6), we derive the following expressions for the position resolution of the horizontal (Δx) and vertical (Δy) coordinates of

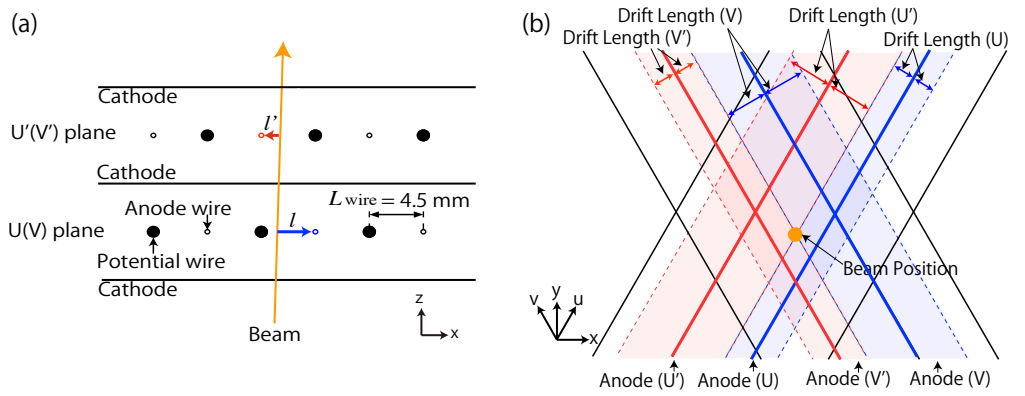

Figure 4.6: Position determination from the hit wires and drift length for the MWDC (UU′VV′ plane). (a) Cross sectional picture of MWDC of type S22. (b) The schematic picture of the anode wire and drift length.

the MWDC with a UU′VV′ configuration:

$$\Delta x = \frac{1}{\sin(\theta_{\rm U} - \theta_{\rm V})}\sqrt{(\Delta\bar{u}\sin\theta_{\rm V})^2 + (\Delta\bar{v}\sin\theta_{\rm U})^2}, \tag{4.7}$$

$$\Delta y = \frac{1}{\sin(\theta_{\rm U} - \theta_{\rm V})}\sqrt{(\Delta\bar{u}\cos\theta_{\rm U})^2 + (\Delta\bar{v}\cos\theta_{\rm V})^2}. \tag{4.8}$$

From the Eqs. (4.3) and (4.4), the position resolution of each U and V plane are

$$\Delta\bar{u} = \frac{1}{2}\sqrt{\Delta u^2 + \Delta u'^2} = \frac{1}{2}\sqrt{(\bar{u}-u)^2 + (\bar{u}-u')^2}, \tag{4.9}$$

$$\Delta\bar{v} = \frac{1}{2}\sqrt{\Delta v^2 + \Delta v'^2} = \frac{1}{2}\sqrt{(\bar{v}-v)^2 + (\bar{v}-v')^2}. \tag{4.10}$$

The efficiency of the MWDC of UU′VV′ plane is defined as

$$\epsilon = \epsilon_{\rm U}\cdot\epsilon_{\rm V} \tag{4.11}$$

$$= \frac{N(|\Delta u| < 3\sigma)\cap N(\text{Plastic})}{N(\text{Plastic})}\cdot\frac{N(|\Delta v| < 3\sigma)\cap N(\text{Plastic})}{N(\text{Plastic})}, \tag{4.12}$$

where $N(\text{Plastic})$ is the number of events hitting the plastic scintillator at FH10 and $N(|\Delta u| < 3\sigma)$ is the number of events satisfying $|\Delta u| < 3\sigma$ required to estimate the resolution.

The efficiency and position resolution of MWDCs are summarized in Table 4.1 and the detectors were previously described in Sec. 3.3.1. Due to the charge-up in the chambers of the MWDCs, the applied high voltage was insufficient to detect Z $\leq$ 2 particle with a high efficiency under high-rate conditions.

Table 4.1: Summary of the efficiency and the resolution of MWDCs.

Detector	Efficiency	Resolution
DC61	86.2 %	0.48 mm
DC91	89.3 %	0.27 mm
DCX1	92.8 %	0.30 mm
DCX2	78.3 %	0.36 mm

4.2.2 Position Detection by using the Micro-Hodoscope

The micro-hodoscope (described in Sec. 3.3.1) was developed to measure the position of the beam at F3 under a high intensity per unit area beam, such as 10^6 cps/mm^2 since it was impossible to use the MWDCs with such a high intensity beam. To estimate the position resolution and detection efficiency of the micro-hodoscope, we first analyzed the pulse width and charge signals with a low-intensity ($\sim 10^4$ cps) beam at F3 with the MWDCs. First, we calibrated the charge individual scintillator bars using the beam. A cross talk among the scintillator bars (a signal from a bar next to the one that was hit) was observed. To separate the true signals from the cross talk, we selected the maximum charge from all the scintillator bars. Then, we determined the signal position as the geometrical position of plastic scintillator bar where the pulse width was largest among the hits.

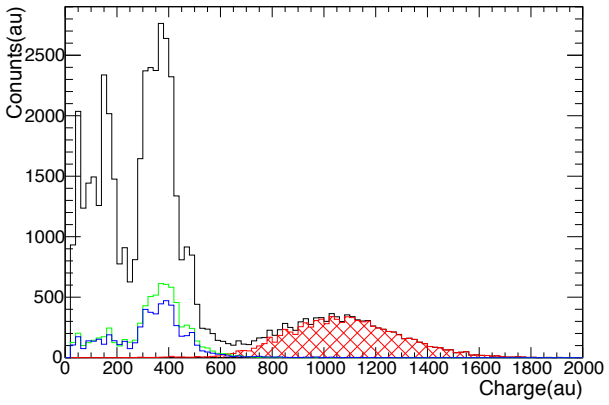

Figure 4.7: The charge of a scintillator bar placed at the center of the x direction (black line). The cross hatched red spectrum is the maximum charge of all the scintillator bars. The blue and green spectra are selected events by the maximum charge in the bars neighboring the central bar.

Figure 4.7 shows the charge in one scintillator bar placed at the center. The solid black line shows charge spectrum with all events. The hatched red spectrum shows events which are selected as the maximum charge in one trigger event after the gain calibration of each scintillator bars. The blue and green spectra show charges produced by cross talk from the neighboring scintillator bars. Here, we show that cross talk signals were identified by charge information. Therefore we determine the hit position at F3 by a scintillator bar where maximum charge was deposited.

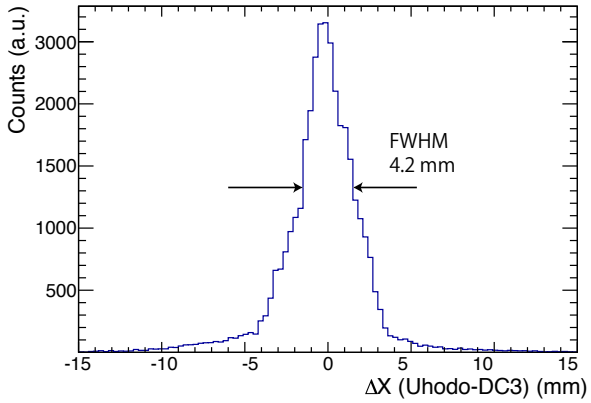

Figure 4.8: The difference between the hit position deduced using micro-hodoscope and the MWDCs.

Figure 4.8 shows the difference between the hit positions deduced by the micro-hodoscope and MWDCs. The position resolution of the micro-hodoscope was described as

$$\Delta x_{\mu\mathrm{Hodo}} = \sqrt{\Delta x^2_{\mathrm{diff}} - \Delta x^2_{\mathrm{DC}}}, \tag{4.13}$$

where $\Delta x_{\mu\mathrm{Hodo}}$ and Δx_{DC} are position resolution of the micro-hodoscope and the MWDCs respectively. The Δ_{diff} is the position resolution at the position of the micro-hodoscope deduced by using the DC31 and the DC32 MWDCs. From Fig. 4.8, $\Delta_{\mathrm{diff}} = 4.20$ mm (FWHM). The position resolution deduced by DC31 and DC32 was 0.56 mm (FWHM) by using the geometrical configuration as shown in Fig. 3.9. Therefore, the position resolution of micro-hodoscope was estimated to be 4.16 mm (FWHM). Initially, we assumed that the position resolution of the micro-hodoscope was the same as its bar width (1 mm). However, our calculations show that the position resolution was actually considerably worse. We attribute this discrepancy to the incomplete identification of cross talk between the scintillator bars.

The efficiency of the micro-hodoscope was 95% for about 10^4 cps beam. For the high rate condition, the efficiency was about 81% because it is difficult to determine the hit scintillator bar in the events that had ^{8}He particles in the previous bunch.

4.2.3 Tracking by using the CRDCs

The trajectories of the reaction products at the S2 final focal plane of the SHARAQ spectrometer were reconstructed using the CRDCs and the plastic scintillators. We determined the hit position using the standard method described in Ref. [37, 48] for one particle and developed new a analytical method for two particles in coincidence.

Vertical Direction

The hit position in the vertical direction is determined by using the drift time of electrons produced by the ionization gas. As described in Sec. 3.3.2, we used the S2PL0 plastic scintillator as an active slit for the calibration of the drift time to distance. Figure 4.9 shows the drift time spectrum except for hit events at the S2PL0. Each peak corresponds to the position of the slits. We estimated the drift velocity of CRDC's from this spectra, and determined that it was 5.39×10^{-2} mm/ns.

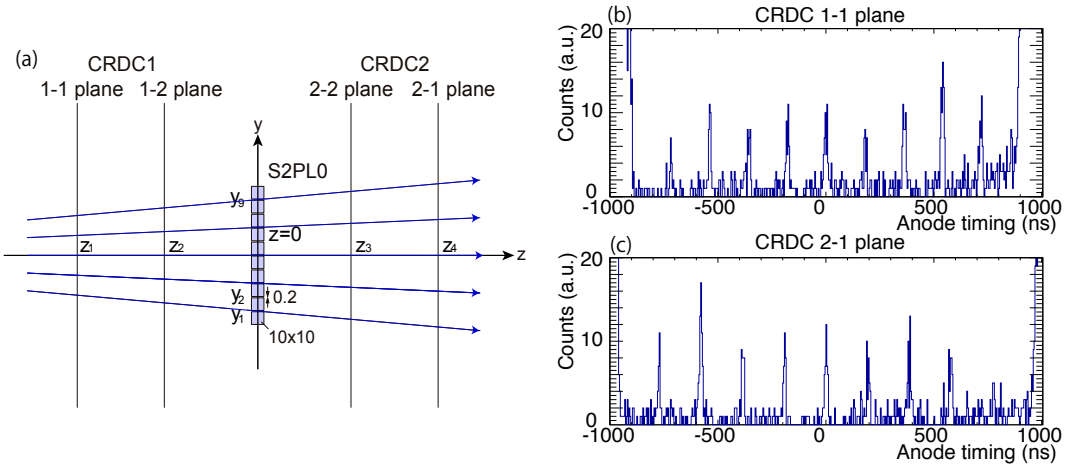

Figure 4.9: (a) A schematic diagram of the calibration in the vertical direction by using the S2PL0 veto plastic scintillator. (b), (c) Spectra of the anode timing of the CRDCs except for hit events at S2PL0.

Horizontal Direction

We determined the hit position in the horizontal direction by examining the distribution of the induced charge on the cathode pads.

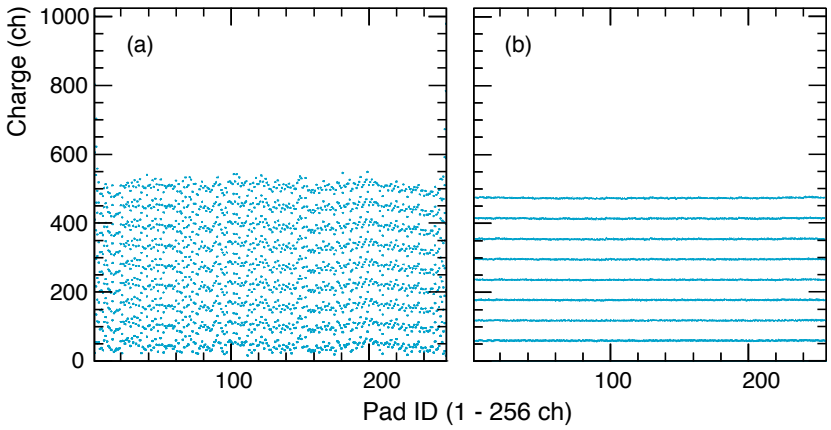

Figure 4.10: Charge distribution of cathode pads of a test pulse (a) before and (b) after the gain and pedestal calibration.

Since the uniformity of the response of each channel is important, we calibrated the pedestal and gain for each channel individually. Figure 4.10 (a) shows a 2-demensional plot of the pad identification number (ID) versus the uncalibrated induced charge, which was obtained using a research pulser. Each pattern was caused by the difference gain of research pulse. After the calibration of the gain and pedestal of each channel, we obtained Fig. 4.10 (b).

Figure 4.11 shows a typical distribution of the induced charge for a reaction product of ^{4}He. In this analysis, we defined a group of pads as a cluster which satisfied the following conditions:

- It consists of a set of two or more adjacent pads;
- All the charges are greater than a threshold value Q_{th};
- The maximum charge among them is greater than a threshold value Q_{max}.

After searching for the cluster, we used the Secant Hyperbolic Squared (SECHS) function [49] to determine the hit position in each plane. The SECHS function is known to give a good fit to the charge distribution, which is shows as

$$f(x|a,\mu,\delta) = \frac{a}{\cosh^2[\pi(x-\mu)/\sigma]}, \tag{4.14}$$

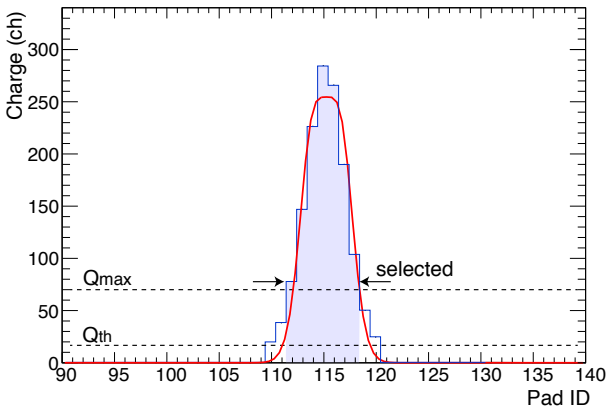

Figure 4.11: Sample of a distribution of induced charge at cathode pads and fit with the SECHS function.

where a is magnitude, μ is centroid and σ is the standard deviation.

Position and Angule Resolution

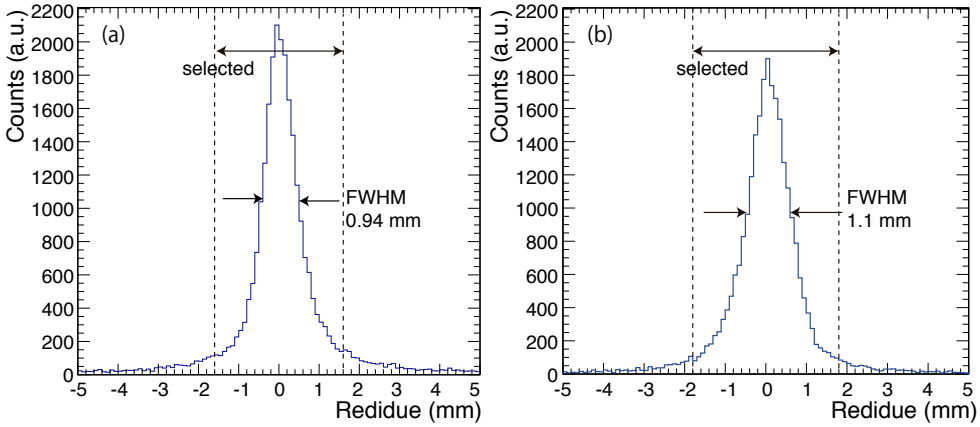

Figure 4.12: Residue distribution of the trajectory fitted by three planes for the (a) horizontal and (b) vertical directions.

We determined trajectory using least-square fit of the hit position of four planes. Then, we estimated the position resolution from the distribution of a residue using

$$\Delta x_i^{\mathrm{res}} = x_i^{\mathrm{hit}} - x_i^{\mathrm{traj}}, \tag{4.15}$$

$$\Delta y_i^{\mathrm{res}} = y_i^{\mathrm{hit}} - y_i^{\mathrm{traj}}, \tag{4.16}$$

where $x_i^{\rm hit}$ and $y_i^{\rm hit}$ are hit positions deduced by the charge distribution of the cathode pads and drift time to the anode wires. The $x_i^{\rm traj}$ and $y_i^{\rm traj}$ are obtained from the tracking by three planes without the i-th plane. Figure 4.12 shows the distribution obtained of residue from the CRDC1-1 plane for the horizontal and vertical directions.

In the vertical direction, the FWHM of the distribution was $\Delta y_1^{\rm res} = 1.1$ mm, which was almost the same for all planes. If residue distribution was the same for all planes, a relation between the residue and position resolution of each plane would be described as $\Delta y_i^{\rm res} = \sqrt{2}\Delta y_i$, where Δy_i is the position resolution of each plane (See Ref. [40]). The position resolution of the focal plane is $\Delta y_i/2$ described by the relation:

$$(\Delta y_{\rm FP})^2 = \sum_i \left(\frac{\partial y_{\rm FP}}{\partial y_i}\right)^2 (\Delta y_i)^2, \tag{4.17}$$

where $\Delta y_{\rm FP}$ is the resolution at the focal plane. Using these relations, position resolution at the focal plane was 0.78 mm (FWHM), which is sufficient performance for this measurement.

The angular resolution $\Delta b_{\rm FP}$ was obtained using a similar relation:

$$(\Delta b_{\rm FP})^2 \simeq (\Delta \tan b_{\rm FP})^2 = \sum_i \left(\frac{\partial \tan b_{\rm FP}}{\partial y_i}\right)^2 (\Delta y_i)^2. \tag{4.18}$$

Therefore, the relationship between the position resolution of each plane and the angular resolution of the focal plane was estimated as $\Delta b_{\rm FP} = \sqrt{2}\Delta y_i/L$, where L was the distance between CRDC1 and CRDC2. The angular resolution was 1.1 mrad, which is sufficient performance for this measurement.

In the horizontal direction, we determined the trajectory using a least-square fit of the hit position of four planes in the same way as the vertical direction. The position resolution was estimated from distribution of a residue defined as

$$\Delta x_i^{\rm res} = x_i^{\rm hit} - x_i^{\rm traj}, \tag{4.19}$$

where $x_i^{\rm hit}$ is the hit position deduced by the drift time and $x_i^{\rm traj}$ is that obtained from tracking by the three planes without the i-th plane. Figure 4.12 (1) shows the obtained distribution of residue in the CRDC1-1 plane. The FWHM of the distribution was $\Delta x_1^{\rm res} = 0.94$ mm, which was almost the same for all planes. Using same relationship of position resolution as vertical direction, the position resolution at the focal plane was 0.66 mm (FWHM), which is sufficient performance for this measurement.

The relation between the position resolution of each plane and angular resolution of focal plane was estimated as $\Delta a_{\rm FP} = \sqrt{2}\Delta x_i/L$ as in the same

case of vertical direction (Eq. (4.18)). The angular resolution was 0.94 mrad, which is sufficient performance for this measurement.

Tracking Efficiency of CRDCs

We estimated the tracking efficiency of the CRDCs using

$$\epsilon = \frac{N(\text{Plastic}) \cap \{N(\Delta x < 4\sigma) \cap N(\Delta y < 4\sigma)\}}{N(\text{Plastic})}, \tag{4.20}$$

where N(Plastic) is the number of events in the S2 plastic coincidence and $N(\Delta x < 4\sigma)$ and $N(\Delta y < 4\sigma)$ are the number of events with $\Delta x < 4\sigma$ and $\Delta y < 4\sigma$ respectively, where trajectories at S2 were successfully obtained. Since the acceptance of the plastic scintillator is larger than that of the CRDCs, we used a defocused beam through the empty target where the spot size was about 20 cm (sigma) diameter at the focal plane. In order to confirm uniformity of position resolution and detection efficiency, we measured the beam trajectories by changing the SHARAQ $B\rho$ setting by ± 1 % and ± 2 %, which correspond to a changing of x positions of ± 60 mm and ± 120 mm, respectively. The position dependence of the tracking efficiency was negligibly small. Finally, the efficiency was estimated to be 89.5 % in the entire effective area of CRDC's.

4.3 Ion Optical Anaysis

The purpose of the ion optical analysis is to determine the momentum of a particle and to consider an acceptance of this measurement. The definition of the transfer matrix is described in Appendix A. In this thesis, we use of indexes BL and SH with matrix elements to describe the Beam Line (F3-F6) and SHARAQ spectrometer (S0-S2), respectively.

4.3.1 High-Resolution Achromatic Mode at the Beam Line

We extracted the key elements of the transfer matrix to determine the momenta of the particles traveling in the BigRIPS-HRB. We ran diagnostics on the ion optics with the low-intense ^{8}He beam data for which allowed us to use the MWDCs at F3. The horizontal position at F6 was expressed as follows by ion optical information at F3:

$$x_{\text{F6}} = (x|x)_{\text{BL}} x_{\text{F3}} + (x|a)_{\text{BL}} a_{\text{F3}} + (x|\delta)_{\text{BL}} \delta. \tag{4.21}$$

In order to measure the momentum of the beam, δ, we extracted the element of magnification, $(x|x)_{\mathrm{BL}}$, focusing, $(x|a)_{\mathrm{BL}}$ and dispersion, $(x|\delta)_{\mathrm{BL}}$. We determined these three elements from the experimental data to measure the momentum of the beam event-by-event.

Dispersion: $(x|\delta)_{\mathrm{BL}}$

The element of the transfer matrix, $(x|\delta)_{\mathrm{BL}}$, is deduced by the relationship between the horizontal position x_{F6} and the momentum of the beam δ. We used the relation between the time of flight between F3 and FH10 ($\mathrm{ToF}_{\mathrm{F3-FH10}}$) as the momentum of the beam and horizontal position at F6. Figure 4.13(a) shows the correlation between the $\mathrm{ToF}_{\mathrm{F3-FH10}}$ and x_{F6}. We selected the momenta and x_{F6} positions for the momenta at 0%, ±0.5% and ±1%, then fit a quadratic function to the data in order to determine the dispersion coefficient $(x|\delta)_{\mathrm{BL}}$. The obtained function was shown in Fig. 4.13(b).

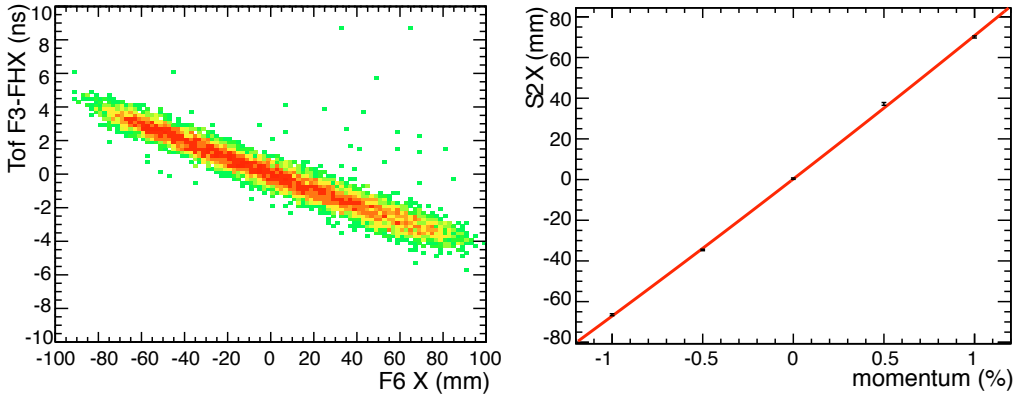

Figure 4.13: (a) The correlation between $\mathrm{ToF}_{\mathrm{F3-FH10}}$ and x_{F6}. (b) The relation between the momentum and x_{F6} selected with momenta of ±0.5, ±1.0% in $\mathrm{ToF}_{\mathrm{F3-FH10}}$ and a quadratic fitting function.

In this analysis, we found that

$$(x|\delta)_{\mathrm{BL}} = 68.94 \ \ \mathrm{mm}/\%. \tag{4.22}$$

Magnification: $(x|x)_{\mathrm{BL}}$, $(x|a)_{\mathrm{BL}}$

In order to determine the transfer matrix element of the position magnification expressed as $(x|x)_{\mathrm{BL}}$, we examined the relation between x_{F3} and x_{F6} with the limitation of a_{F3} and the momentum, δ. A momentum resolution better than ±0.01% was necessary to neglect the contribution of the $(x|\delta)\delta$ term in

Eq. 4.21. However, the momentum resolution determined by the $\mathrm{ToF}_{\mathrm{F3-FH10}}$ was insufficient. For this reason, we used the ^{8}Li beam of 200 MeV/u to calculate the transfer matrix element of the $(x|x)_{\mathrm{BL}}$ and $(x|a)_{\mathrm{BL}}$ element. The difference between the transfer matrix element of the first-order aberration of the ^{8}Li and ^{8}He beams was expected to be small, while the higher-order aberration was crucial.

There was a position and angle magnification of the horizontal image between F6 and F3, which was expressed as $(x|x)_{\mathrm{BL}}$ and $(x|a)_{\mathrm{BL}}$. The relationship between F3 and F6 is expressed in Eq. 4.21.

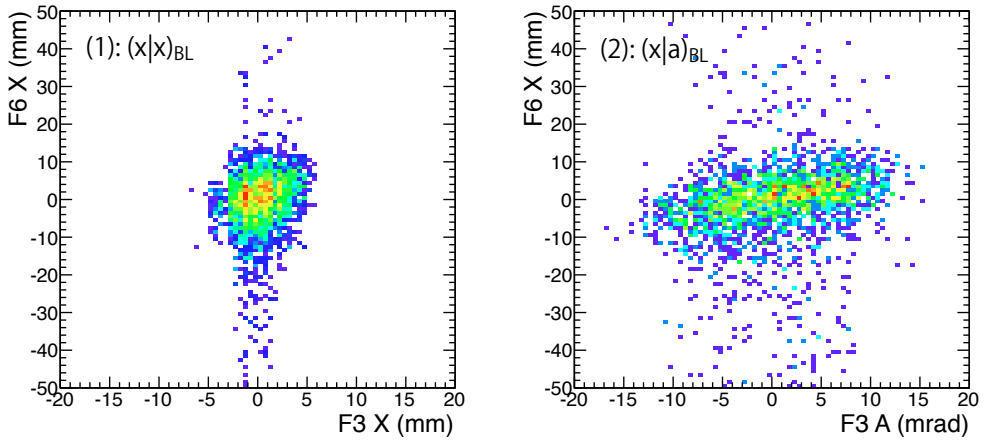

Figure 4.14: (1) The correlation between x_{F3} and x_{F6} limited by a_{F3} and δ. (2) The correlation between a_{F3} and x_{F6} limited by x_{F3} and δ.

Figure 4.14 (1) shows the correlation between x_{F3} and x_{F6}, which is limited by a_{F3} and δ, in order to neglect the contribution from the a_{F3} and δ. Figure 4.14 (2) shows the correlation between a_{F3} and x_{F6}, which is limited by x_{F3} and δ. We determined the $(x|x)_{\mathrm{BL}}$ and $(x|a)_{\mathrm{BL}}$ from the inclination of Fig. 4.14 (1) and Fig. 4.14 (2), respectively. In the Fig. 4.14 (1), the vertical patterns were due to the inefficiency of particles within near the anode wire at the F3 MWDCs. It was not influenced by the inclination of the loci.

We found that

$$(x|x)_{\mathrm{BL}} = 0.83, \tag{4.23}$$

$$(x|a)_{\mathrm{BL}} = 0.31. \tag{4.24}$$

The angle magnification $(x|a)_{\mathrm{BL}}$ was larger than that of the design value, which was almost zero. In order to measure the momentum from the position at F6, which was independent from the incident angle, the value of $(x|a)_{\mathrm{BL}}$

had to be as small as possible. Since we did not measure the angle of F3 in the physics measurement, this caused some ambiguity, which made the momentum resolution worse.

4.3.2 Large Momentum Acceptance Mode at SHARAQ

To extract the elements of transfer matrix $R_{\rm SH}$, we used the low intensity beam of ^{4}He without the secondary target.

Position and Angle Magnification

We extracted the first-order elements of the transfer matrix of large momentum acceptance mode at the SHARAQ spectrometer.

The horizontal position and angle at S2 were expressed as

$$x_{\rm S2} = (x|x)_{\rm SH}x_{\rm S0} + (x|a)_{\rm SH}a_{\rm S0} + (x|\delta)_{\rm SH}\delta \quad \text{and} \tag{4.25}$$

$$a_{\rm S2} = (a|x)_{\rm SH}x_{\rm S0} + (a|a)_{\rm SH}a_{\rm S0} + (a|\delta)_{\rm SH}\delta \quad . \tag{4.26}$$

We extracted the elements of position magnification, $(x|x)_{\rm SH}$, from

$$(x|x)_{\rm SH} = \left.\frac{\partial x_{\rm S2}}{\partial x_{\rm S0}}\right|_{a_{\rm S0},\delta}. \tag{4.27}$$

The inclination of a slope and the correlation between $x_{\rm S0}$ and $x_{\rm S2}$ were used to determine the $(x|x)_{\rm SH}$ element as shown in Fig. 4.15 (1),where $a_{\rm S0}$ and δ were negligible for $(x|x)_{\rm SH}$ term. In this analysis, position of $x_{\rm S2}$ was used to determine the momenta (δ) of the outgoing α particles on an event-by-event basis. The magnification was evaluated to be

$$(x|x)_{\rm SH} = -0.45. \tag{4.28}$$

Comparing $(x|a)_{\rm SH}$, to the position magnification, we obtained Fig. 4.15 (2) with similar limitations as $x_{\rm S0}$ and δ. The focus element, $(x|a)_{\rm SH}$, had vanished, so the focusing from S0 to S2 was fulfilled as ion-optically designed. In the same manner, we calculated

$$(a|x)_{\rm SH} = -0.54, \tag{4.29}$$

$$(a|a)_{\rm SH} = -2.51, \tag{4.30}$$

$$(a|\delta)_{\rm SH} = 5.74. \tag{4.31}$$

For vertical matrix elements shown in Fig. 4.16, we determined

$$(y|y)_{\rm SH} = -0.07, \tag{4.32}$$

$$(y|b)_{\rm SH} = -1.58, \tag{4.33}$$

$$(b|y)_{\rm SH} = 0.39, \tag{4.34}$$

$$(b|b)_{\rm SH} = 0.19. \tag{4.35}$$

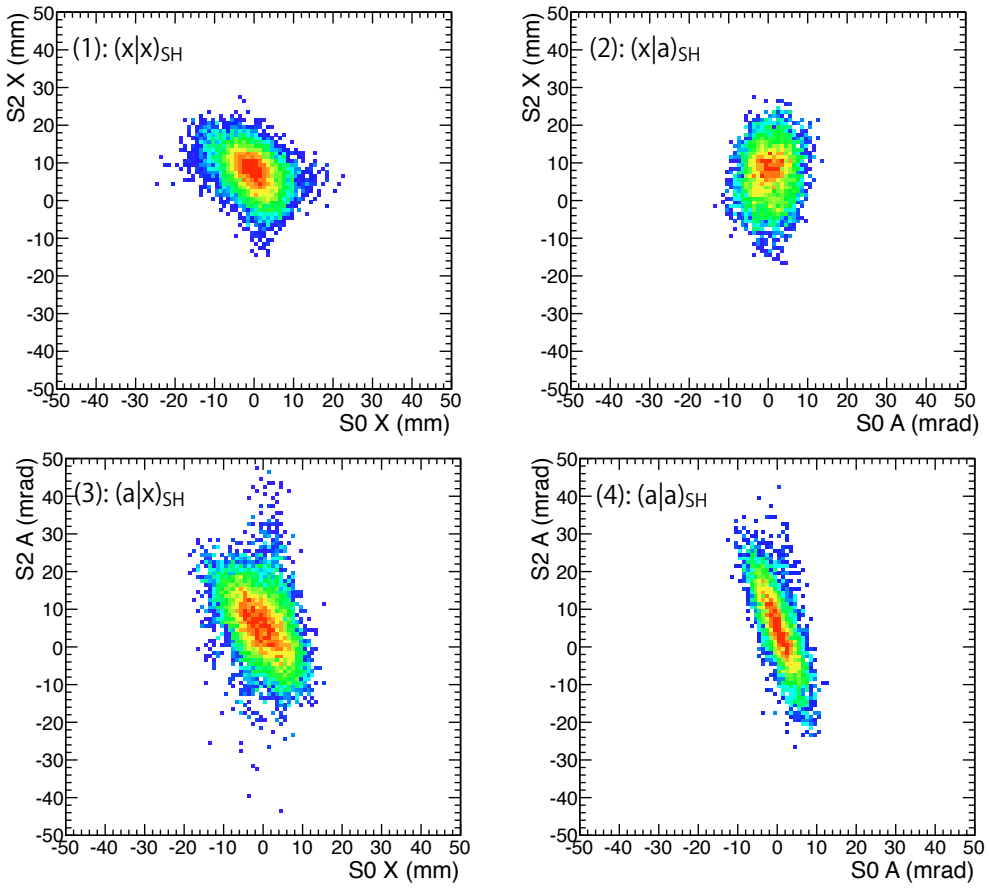

Figure 4.15: (1) The correlation between x_{S0} and x_{S2} limited by a_{S0} and δ. (2) The correlation between a_{S0} and x_{S2} limited by x_{S0} and δ. (3) The correlation between x_{S0} and a_{S2} limited by a_{S0} and δ. (4) The correlation between a_{S0} and a_{S2} limited by x_{S0} and δ.

As a specification of a magnetic spectrometer, it was important that the $(y|y)_{\mathrm{SH}}$ element was tuned to zero. This setting fulfilled the requirement that the S2 vertical position (y_{S2}) depends on only $(y|b)_{\mathrm{SH}}$ in the first-order matrix elements, therefore the vertical scattering angle of outgoing particles can simply be determined from y_{S2}.

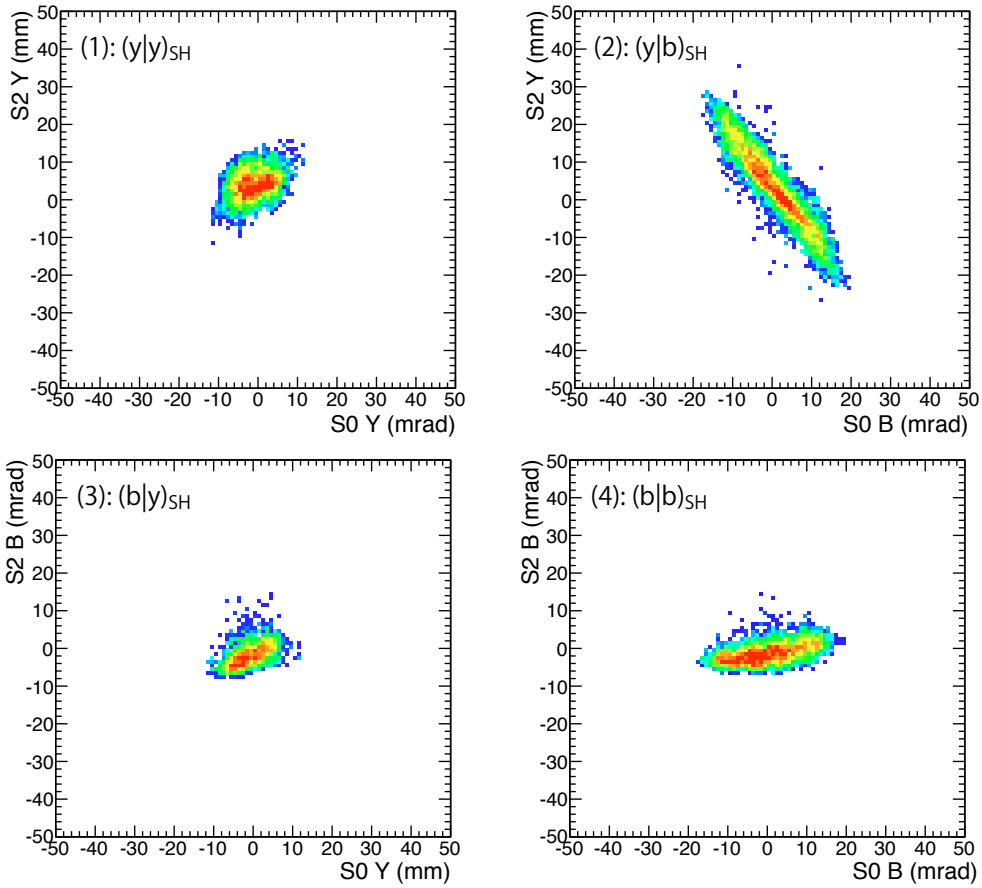

Figure 4.16: (1) The correlation between y_{S0} and y_{S2} limited by b_{S0}. (2) The correlation between b_{S0} and y_{S2} limited by y_{S0}. (3) The correlation between y_{S0} and b_{S2} limited by b_{S0}. (4) The correlation between b_{S0} and b_{S2} limited by y_{S0}.

Higher Order Aberration of the Horizontal Focus $(x|x\delta)_{\mathrm{SH}}$, $(x|a\delta)_{\mathrm{SH}}$

In order to measure the momentum more precisely, we examined the second-order aberration of the transfer matrixes, especially for the $(x|x\delta)_{\mathrm{SH}}$ and $(x|x\delta)_{\mathrm{SH}}$ terms, which were expected to be relatively large.

The horizontal position at S2 including higher order aberrations from the momentum distribution was expressed as:

$$x_{S2} = \{(x|x)_{SH} + (x|x\delta)_{SH}\delta\}x_{S0} + \{(x|a)_{SH} + (x|a\delta)_{SH}\delta\}a_{S0} + (x|\delta)_{SH}\delta. \quad (4.36)$$

The term $(x|a\delta)_{SH}$ causes shifting and tilting in the S2 focal plane. Detail of this effect is described in Ref. [37]. In order to extract the effect of $(x|a\delta)_{SH}$ term, we examined the correlation of the x_{S2} and a_{S2}, while the definition of the $(x|a\delta)_{SH}$ term depends on the correlation between a_{S0} and x_{S2}. For convenience, we define a $(x|a\delta)'$ as $(x|a\delta)'_{SH}a_{S2}\delta = (x|a\delta)_{SH}a_{S0}\delta$.

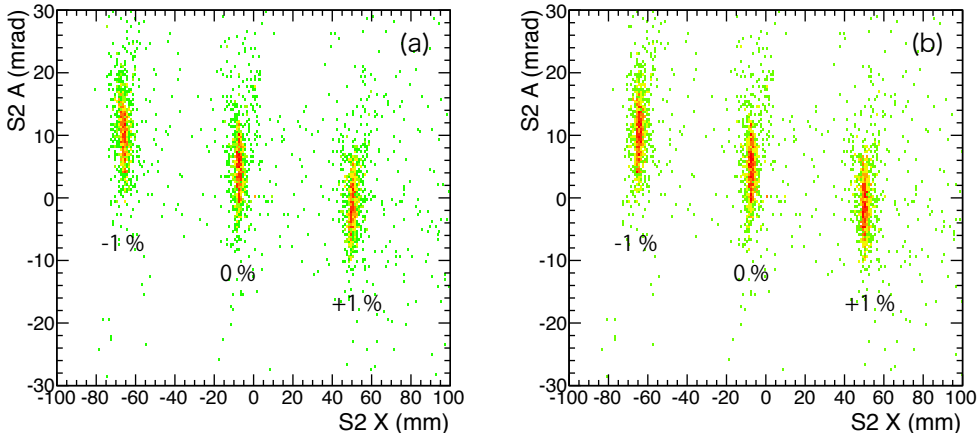

Figure 4.17: Correlation between x_{S2} vs a_{S2} (a) before and (b) after the correction. The three loci correspond to different magnet settings of the SHARAQ spectrometer.

Figure 4.17 (a) shows the correlation between x_{S2} and a_{S2}. The three loci correspond to momenta of -1%, 0% and +1%. These loci were taken with different magnet settings using the SHARAQ spectrometer. Based on the tilt shown in Fig. 4.17 (a), we determined that

$$(x|a\delta)'_{SH} = 0.0025 \ \text{ mm/mrad \%}. \quad (4.37)$$

Figure 4.17 (b) shows corrected correlation by the $(x|a\delta)_{SH}$.

For the term of $(x|x\delta)_{SH}$, we examined at the correlation between x_{S2} and x_{S0} as shown in Fig. 4.18. We obtained that

$$(x|x\delta)'_{SH} = 2.8 \times 10^{-3} \ \text{ mm/mm\%}. \quad (4.38)$$

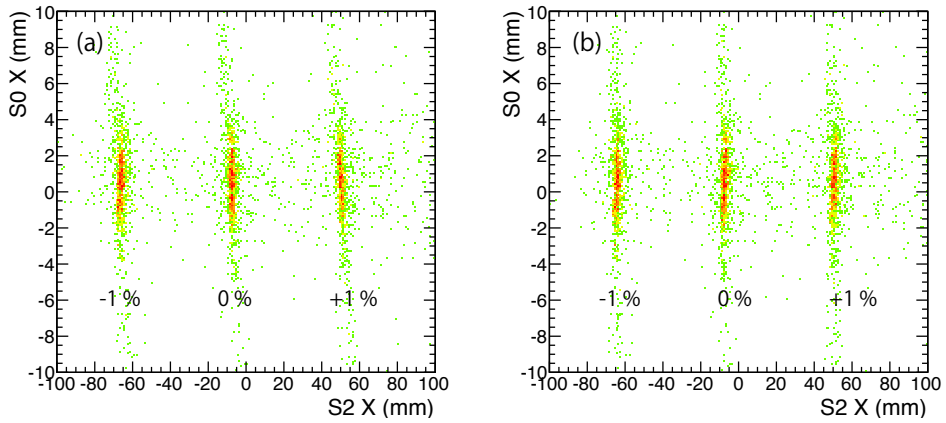

Figure 4.18: Correlation of x_{S2} vs x_{S0} (a) before and (b) after the correction. The three loci correspond to the different magnet settings of the SHARAQ spectrometer.

Dispersion $(x|\delta)_{SH}$

After the correction of the horizontal focuses $(x|a\delta)_{SH}$ and $(x|x\delta)_{SH}$, the dispersion, expressed as $(x|\delta)_{SH}$, was extracted using the ^{4}He beam with different magnetic settings of the SHARAQ spectrometer. Figure 4.19 (a) shows the x_{S2} for each magnetic setting of the SHARAQ spectrometer. Figure 4.19 (b) shows the relation between x_{SH} and the momentum of the central ray of the SHARAQ spectrometer calculated by a NMR of the dipole magnet.

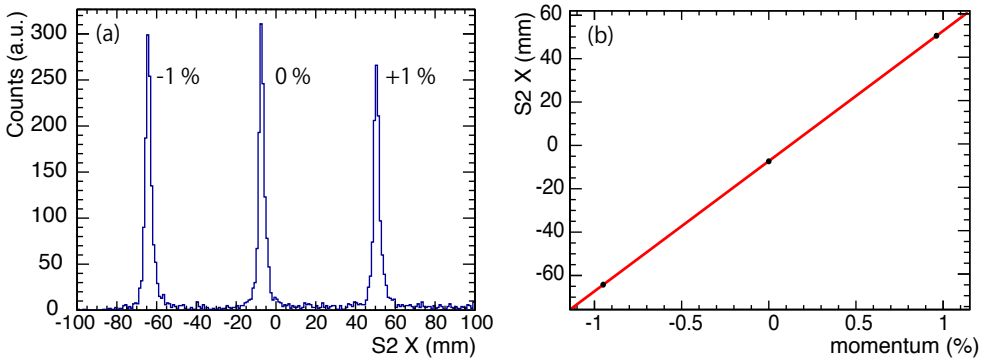

Figure 4.19: (a) The x_{S2} corrected by $(x|x\delta)_{SH}$ and $(x|a\delta)_{SH}$ components. Each peak corresponds to -1%, 0 % and +1% of the momentum. (b) Fitting by the linear function.

We determined that

$$(x|\delta)_{\rm SH} = 60.06 \ \ {\rm mm}/\%. \tag{4.39}$$

4.3.3 Reconstruction of scattering angle

The scattering angle was reconstructed by using the inverse matrix of the $R_{\rm SH}$. The phase space at S0 reconstructed by S2 phase space was expressed as

$$\vec{X}_{\rm S0} = R_{\rm SH}^{-1}\vec{X}_{\rm S2}. \tag{4.40}$$

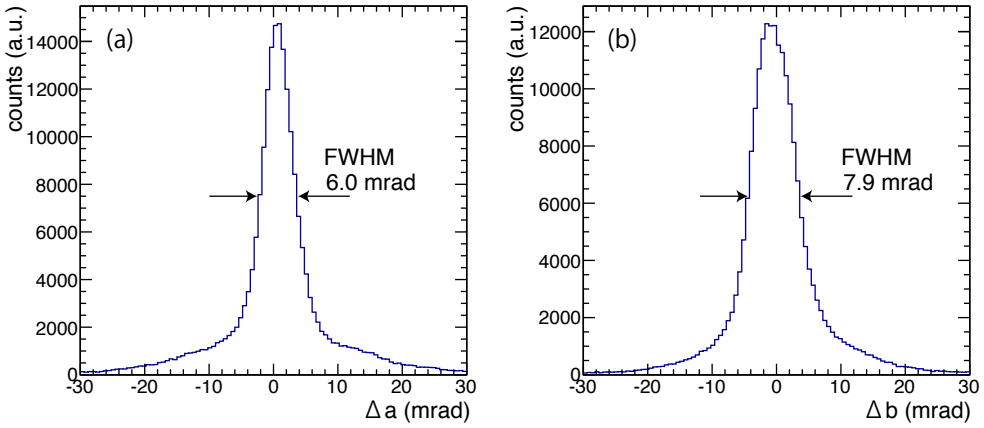

Figure 4.20: The difference between the angle of S0 reconstructed using the S2 and FH10 MWDCs at FH10 for (a) the horizontal direction and (b) the vertical direction.

In order to estimate the angular resolution, we defined

$$\Delta a = a_{\rm S0(SH)} - a_{\rm S0(BL)}, \tag{4.41}$$
$$\Delta b = b_{\rm S0(SH)} - b_{\rm S0(BL)}, \tag{4.42}$$

where $a_{\rm S0(SH)}$ and $b_{\rm S0(SH)}$ are the S0 angle reconstructed by S2, and $a_{\rm S0(BL)}$ and $b_{\rm S2(BL)}$ are the S0 angle reconstructed by FH10 MWDCs for the horizontal and vertical directions, respectively. Figure 4.20 shows the distribution of Δa and Δb. We obtained an angular resolution of 6.0 mrad (FMHM) for the horizontal direction and 7.9 mrad (FWHM) for the vertical direction.

4.3.4 Momentum Resolution

We estimated the momentum resolution of the SHARAQ spectrometer using the series of correction from the ion optical information. This momentum resolution corresponds to the energy resolution of the missing-mass spectrum of the four-neutron system. We used the ^{8}Li beam in order to estimate the momentum resolution since the ^{8}He beam with an energy of 186 MeV/u was not measured by the SHARAQ spectrometer.

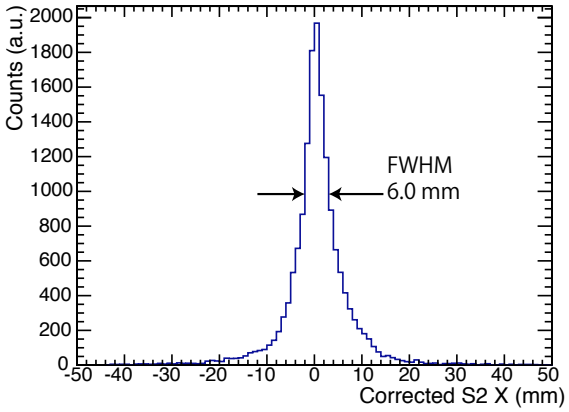

Figure 4.21: The momentum resolution at S2 corrected by the series of the correlation described in the previous section and the position of the F6.

Figure 4.21 shows the horizontal position at S2 corrected by the series of the correlations described in previous section and the position of F6. We corrected the position of S2 by 6.0 mm (FWHM) which corresponds to the momentum resolution of $\delta p/p \sim 1/1000.0$ and the energy resolution of 2.74 MeV (FWHM). This estimated momentum and energy resolution was worse than expected. We attribute to the dispersive focus which was slant at relative to the expected focal position at F6. If the focal plane was slant at F6, the position at F6 depend on the angle. However, we did not measure the angle at the F6. Another contribution was the multiple scattering of the materials in the beam line such as the plastic scintillators, which make the momentum distribution large.

4.3.5 Acceptance

Angular and Momentum Acceptance of the SHARAQ

It is necessary to estimate the angular acceptance or solid angle of the spectrometer in order to calculate the absolute value of the cross section. In

particular for this experiment, it was difficult to estimate the effective angular acceptance of the two α particles when one of the particle was restricted by the aperture of the spectrometer at a large angle. For this reason, we selected a region where the uniformity of the angular acceptance was ensured which was independent from the momentum of the particle (i.e. excitation energy of the four-neutron system). This region corresponds to the flat top region of the effective solid angle shown in a Fig. 3.5. In order to select this acceptance, we checked the phase space of a single α particle produced from the secondary target emitted at a large angular distribution in the spectrometer.

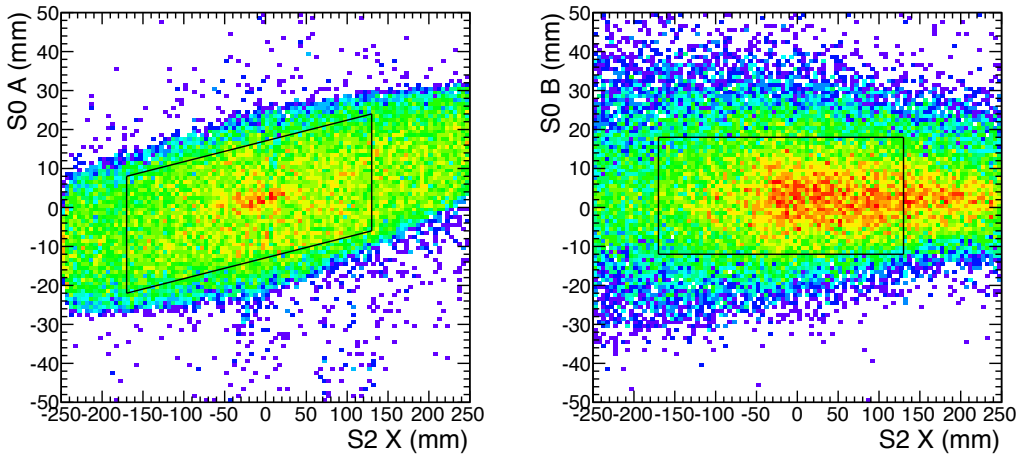

Figure 4.22: The correlation between the horizontal position at the S2 and the scattering angle at the target (S0) for (a) the horizontal and (b) the vertical direction. An area inside the solid line represents an area where the uniformity of the angular and momentum acceptance were ensured.

Figure 4.22 shows the correlation between horizontal position of the S2 and scattering angle at the S0 reconstructed by the S2 with events of single α particle production from the ^{8}He beam at the target. We used a region inside of the solid line in this analysis in order to ensure that angular acceptance was uniform.

Momentum Acceptance at F6

In order to ensure the uniformity of the momentum acceptance of the beam, we selected a region at F6. Figure 4.23 shows the distribution of the horizontal position at F6, which corresponds to the momentum of the beam. This

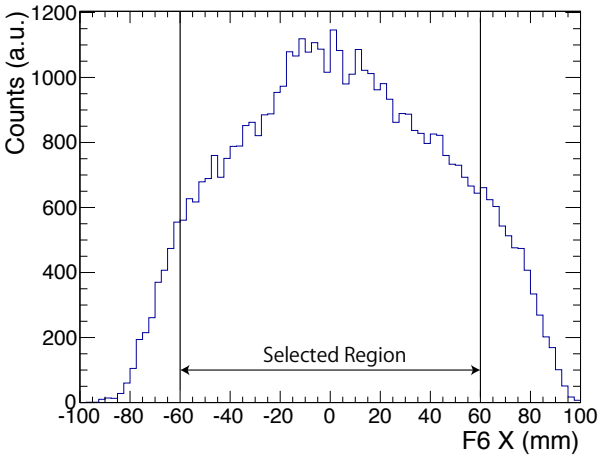

Figure 4.23: The distribution of the horizontal position at F6.

figure was obtained with the ^{8}He beam injected to the secondary target and produced a single α particle. The image of the horizontal direction was restricted since the transmission of the α particle was reduced by the aperture of the beam line. We selected the region between the solid lines in order to ensure that the momentum acceptance of the beam was uniform.

4.4 Selection of 4n Events

In order to select as many four-neutron production event as possible to obtain the best statistics, we performed the following steps:

- determine particle identification with ToF and energy loss for the beam and reaction product,
- remove events with multi-particles in a triggered bunch,
- select two α particles in coincidence at the final focal plane,
- select the of position at the target, and
- confirm the kinematics to reconstruct the invariant-mass of ^{8}Be.

Since the statistics were limited, it was important to examine a suitable selection cut for this analysis.

4.4.1 Particle Identification

Secondary Beam

We performed particle identification of the beam by using the ToF and anode charge of the MWDC. The ToF is the timing difference between the F3 and FH10 plastic signals. For the energy loss, we examined the anode charge of the MWDC (DCX1). The anode charge of the MWDC was used to obtain information on the energy loss under the high-rate condition. Pile up of the charge was expected to be very few, in comparison with the charge of plastic scintillator detected by using the QTC, which has timing window to integrate charge.

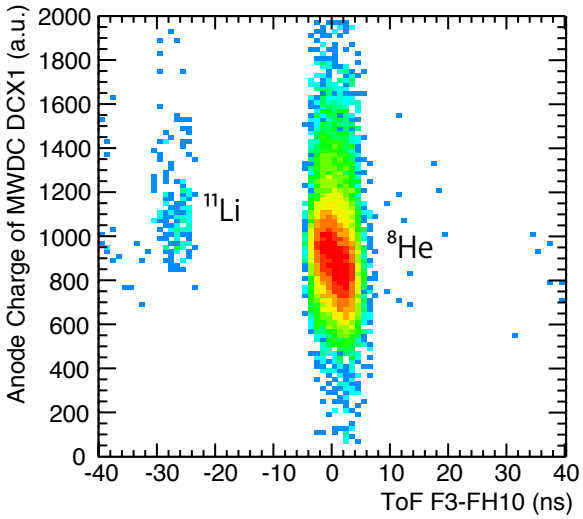

Figure 4.24: Particle identification of the ^{8}He beam.

Figure 4.24 shows the particle identification of the ^{8}He beam. The ToF corresponds to the ratio of the mass number to the atomic number: A/Z. Purity of the ^{8}He achieved 99.3%. There was about 0.7% of ^{11}Li contaminant.

Reaction Products

We performed particle identification of the reaction products at the SHARAQ spectrometer using the ToF and the charge of the plastic scintillator. The ToF was the timing difference between the FH10 and S2 plastic scintillators. We used the charge of the S2PL3 plastic scintillator since it is the thickest scintillator. The charge of plastic scintillator was corrected by the effect of

energy loss depending on the momentum difference which was a function of the vertical position of S2.

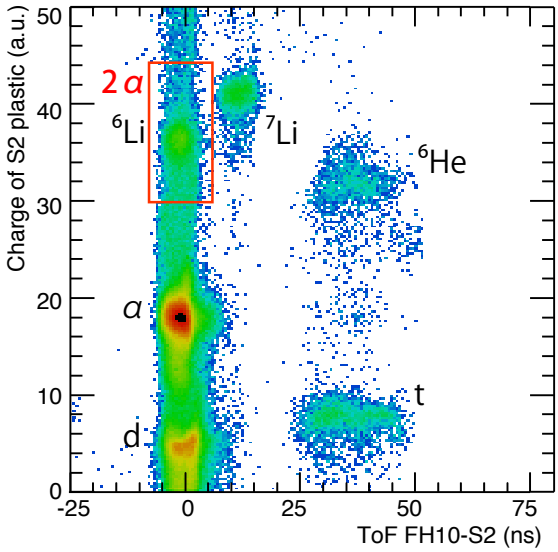

Figure 4.25: Particle identification of the reaction product.

Figure 4.25 shows the particle identification of the reaction products. The ToF corresponds to A/Z. Here, we see that two α particles have the same A/Z ratio as a single α particle, a deuteron and ^{6}Li. The energy loss for the two α particles is the 8 times larger than that of a proton because the energy loss of the charged particle is usually proportional to Z^2. However, if we include the quenching effect of the plastic scintillator, the energy loss of the charged particle is almost proportional to Z. Thus, the energy loss for two α particles is 4 times larger than that of the proton. Similarly, the energy loss of ^{6}Li is 9 times larger than that of the proton assuming a Z^2 dependence and 3 times larger with a Z dependence. Since these particles have the same ToF and similar values for energy loss compared to the proton, we cannot positively identify the region with only 2α in Fig. 4.25. For this reason, we selected the region indicated by a red square in Fig. 4.25 for the analysis.

4.4.2 Multi-Particle Identification at F6 MWDC

As discussed in Sec 4.1, multi-particles in "trigged bunch" and "neighbor bunch" can not negligible. Since the drift time of the MWDCs was about 120 ns was larger than the RF which was 73 ns, it is essential to identify

the beam particles in cases discussed later (see Fig. 4.27) and to track the correct trajectory of the beam particle.

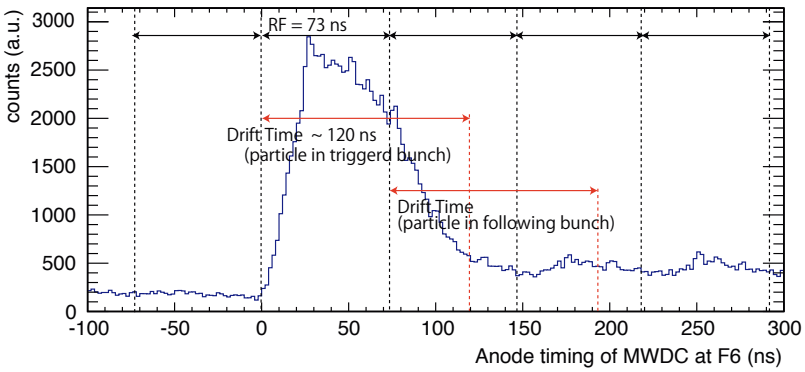

Figure 4.26: The drift time of anode wire of MWDC by reading multi-hit TDC.

Figure 4.26 shows an example of the anode timing of the F6 MWDC which stands for the drift time in the detector measurement by the multi-hit TDC. The dashed line represents the timing of the bunch structure of the cyclotron. This figure shows a bunch structure of 13.7 MHz AVF cyclotron which correspond to 73.0 ns interval and a half-bunch structure which is caused by difference between the number of turning for other cyclotron. The dotted red line indicates the shape of the anode timing of a MWDC obtained under the low intensity beam condition. Distributions for different bunches were simulated by 73 ns offsets. However, the maximum value for the drift time of the MWDC was 120 ns. Since the MWDC drift time was larger than the cyclotron RF period, it was possible that the anode signal from a particle in a following bunch could be confused with the signal from a triggered bunch.

We consider two cases as illustrated in Fig. 4.27:

(1) a single-particle in a triggered bunch and particles in the following bunch

(2) multi-particle in a triggered bunch

These cases cannot be identified using the QTC (Charge to Timing Converter) information of the plastic scintillators because the width of the charge integral gate was longer than the RF interval. Then we used the sum of the

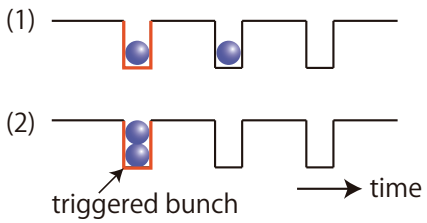

Figure 4.27: Multi-particle in data set of one event.

drift length $L = l + l'$ for pair plane of a F6 MWDC, with a plane configuration VV′UU′. The V′(U′) wire plane was shifted to half way through the cell of V(U) plane (see Sec. 3.3.1 for details). Cell size of the DC31 and DC32 MWDCs were smaller than other MWDCs, but they were specialized for F3 where the beam spot was the smallest and had an acceptance that was too small to use the dispersive focal plane or other planes. If there were more than two signals in the timing window of the drift time for each plane, we chose with drift lengths that summed to $L_{\rm wire}$, where $L_{\rm wire}$ is the distance between wires (45 mm). For this analysis, we could find the correct trajectory of the particle whether there were particles in the following bunch or not (case (1)). Furthermore, if there were more than two pairs of signals whose sum of the drift length was constant corresponding to the time twice as the RF interval, we could identify a multi-particle in the triggered bunch (case (2)). Events in case (2) were excluded from the analysis because we could not identify which particle produced the reaction products detected at S2.

Case (1): Single Particle in a Triggered Bunch and Particles in the Following Bunch

In the beam with an intensity of 2×10^6 cps, about 15% of events a particle in the following bunch. In order to identity the hit positions of particles at the trigger and the following bunches, we used information on the sum of drift lengths obtained from pair planes, such as V and V′ planes. Figure 4.28 shows the sum of drift lengths of DC6 after the timing cut of as in Fig. 4.5. The blue shaded area shows hits from the particle in the triggered bunch, so we selected hits in this area to reconstruct the trajectory. Events with summed length around 8.5 mm were considered to have originated from a hit in following bunch.

Figure 4.29 shows a snapshot of a typical event where two particles hit a detector in a trigger bunch and the one following. The solid lines represent

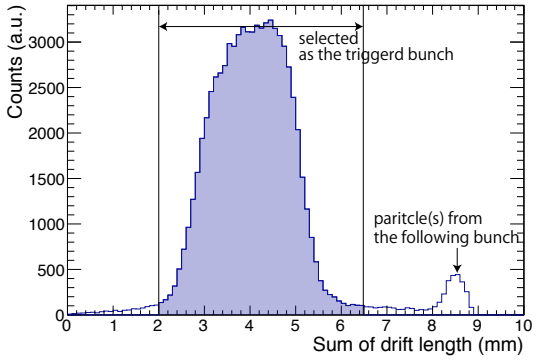

Figure 4.28: The data obtained showing the sum of the drift length at the F6 MWDC in the V and V′ plane.

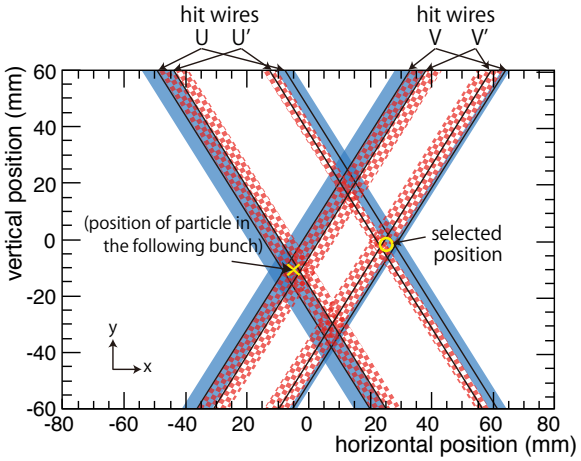

Figure 4.29: Snapshot of a typical event where two particles hit a detector sequentially in the trigger and the following bunch. The blue solid and red meshed bands represent the drift length of the U(U′) and V(V′) planes from wires (indicated by the solid line), respectively. The position (indicated by the yellow circle) of a particle in the triggered bunch is selected by the requirement that the sum of the drift length is same as the interval of the wires. The yellow cross denotes the particle in the next bunch of the triggered particle.

hit wires, while the blue solid and red meshed bands represent the drift length of U(V) and U′(V′) planes, respectively. In Fig. 4.29, the deduced position is indicated by a yellow circle, although there are four candidates for the hit position. On the other hand, the yellow cross denotes the position of a particle in the following bunch. The sum of drift length of this event is about twice the interval of the wires, which are shown in the 8–9 mm region in Fig. 4.28.

We improved the statistics by about 15%, compared with the case when we do not analyze the events where two particles are irradiated in sequential bunches.

Case (2): Multi-Particle in a Triggered Bunch

In the same manner of case (1), we identified more than two particles in the triggered bunch. We identified such events as case (2) when the two particles were identified at VV′ or UU′ pair plane. Since the efficiency of DC6 was 85% for the single α particle, we employed the "or" logic for the VV′ and UU′ plane.

4.4.3 Beam Position at the Target

In order to confirm that reaction products were made by ^{4}He(^{8}He,^{8}Be)4n reaction at the helium target, not for instance, in the aluminum target frame.

Confirmation of Target Position

In order to ensure that reaction products were produced in the liquid He target, we confirmed the reaction point in the target and selected the region to use for the analysis. Figure 4.30 shows the beam image at the target with (a) a down scale trigger of FH10. In this experiment, the center of the beam spot was shifted to negative position in the x direction. For this reason, large amounts of reaction products were produced at the aluminum frame of the target cell as shown in Fig. 4.30 (b). Figure 4.30 (c) shows a plot in which each bin content shown in (b) is divided by these in (a), which clearly shows the target position. We decided to use the events in circle with a diameter of 25 mm for the analysis.

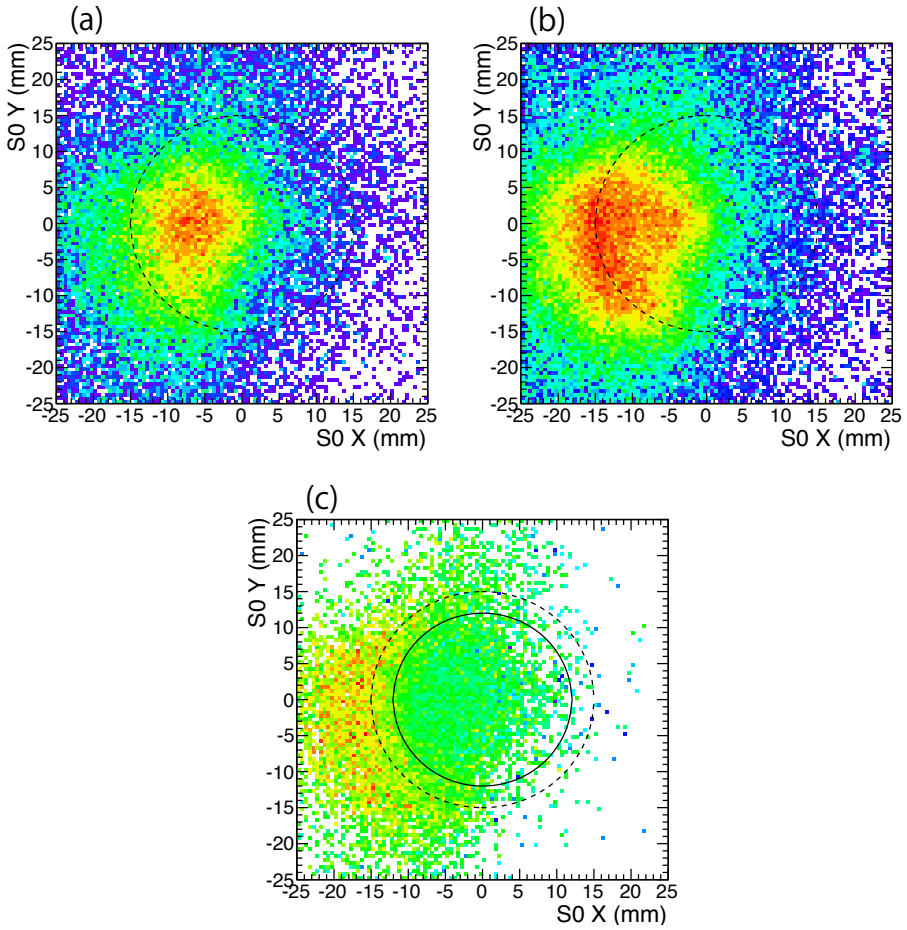

Figure 4.30: Beam image at the target with (a) a down scale of the FH10 trigger and (b) the S2 trigger. (c) A result of dividing each bin content of (b) by (a). The dashed line represents a circle 30 mm in diameter, which is same size as the target cell. The solid line represents a circle 25 mm in diameter.

4.4.4 Tracking of Two α Particle at the Final Focal Plane

To track two α particles produced by ^{8}Be, we developed a new analysis method [42]. This subsection describes this method in detail. The tracking of each particle was based on the analysis described in Sec. 4.2.3.

Vertical Direction

In order to identify and track two α particles, we used the sum of the ex-gaussian function [50] in the fitting procedure of the anode pulse shape data acquired by the flash-ADC. The ex-gaussian function is

$$g(x|a,\mu,\sigma,\tau) = \frac{a}{\tau\sqrt{2\pi}} \exp\left(\frac{\sigma^2}{2\tau^2} - \frac{x-\mu}{\tau}\right) \times \Phi\left(\frac{x-\mu}{\sigma} - \frac{\sigma}{\tau}\right), \quad (4.43)$$

$$\Phi(y) = \int_y^\infty \exp\left(-\frac{y^2}{2}\right) dy, \quad (4.44)$$

where a is the magnitude, μ is the timing of maximum voltage, σ is the width and τ is the decay constant. The function $\Phi(y)$ is known as the Cumulate Distribution function. In order to fit a double pulse shape, we used the sum of two ex-gaussian functions

$$G_{2\mathrm{p}}(t) = g(t|a_1,\mu_1,\sigma_1,\tau_1) + g(t|a_2,\mu_2,\sigma_2,\tau_2). \quad (4.45)$$

At first, parameters of the ex-gaussian for the single α particle were deduced from the pulse shape of a single α particle. Figure 4.31 (a) shows the correlation between the peak voltage of the pulse from an anode wire in the CRDC1-1 plane and the charge of the plastic scintillator, S2PL1. Events in this figure are selected by a software gate of ToF as shown in Fig. 4.25. Loci of triton, α and ^{6}Li are clearly seen. The blue, red and green solid lines in Fig. 4.31 (b) represent the distribution of the peak voltages of the pulse selected by the a software gate of each particle as shown in Fig. 4.31 (a).

In order to estimate the frequency of our misidentification of triton and ^{6}Li as α particles, the charge distribution of the α particle was fitted by a function which included triton, α and ^{6}Li components. These events make up the background. The charge distributions of the triton and ^{6}Li were assumed to have a Landau distribution, which are represented the blue and green dashed lines in Fig. 4.33 (c). Since we selected the indicated region as being α particles in Fig. 4.33 (c), the events in the blue and green shaded area were misidentified as α particle events. The portion of the events was 0.21 % of the total, which was negligibly small.

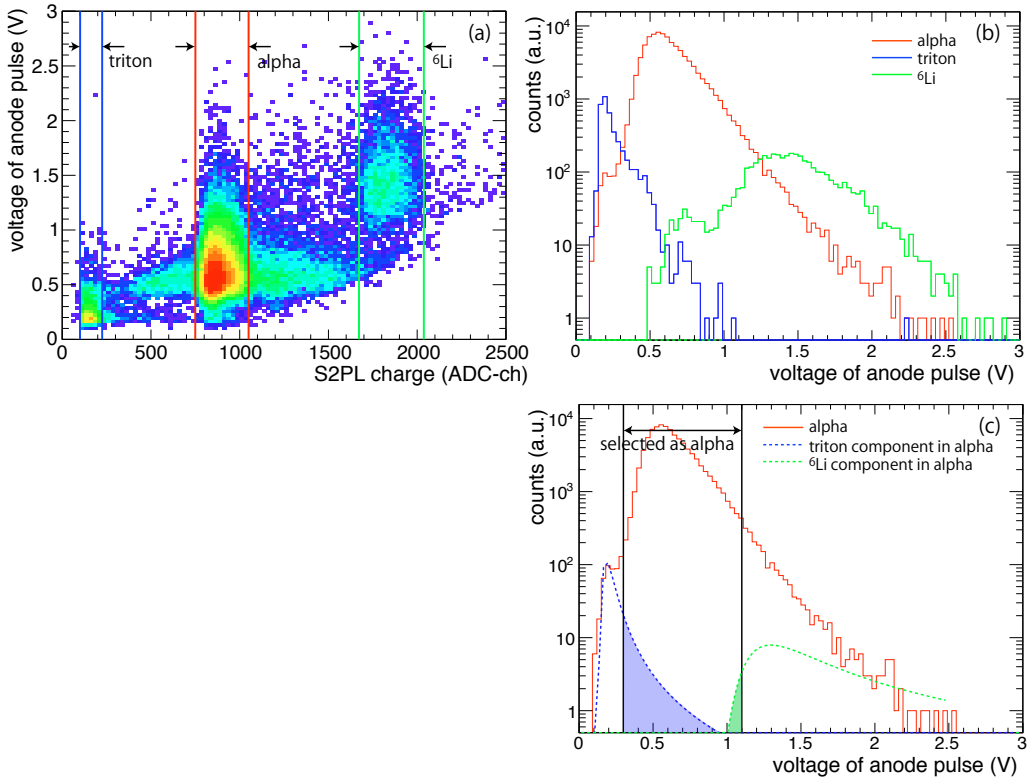

Figure 4.31: (a) The correlation between the peak voltage of the pulse from the anode wire of CRDC1-1 and the charge of plastic scintillator S2PL1. (b) The blue, red and green solid lines represent the distribution of peak voltage of pulse selected by the charge of plastic for triton, α and ^{6}Li, respectively. (c) The blue and green dashed lines represent the component of the triton and ^{6}Li deduced by the fitting of the distribution of α events (red solid line).

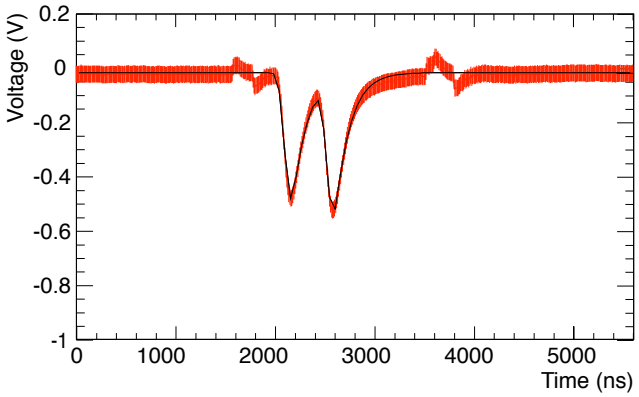

Figure 4.32: A sample of an anode pulse shape of two α particles and a fitting function produced by the sum of two ex-gaussian functions (Eq. (4.44)).

The fitting parameters σ_1, σ_2, τ_1 and τ_2 were determined by fitting a single α particle. These parameters were then fixed to fit the two α particles. We assumed an error for the voltage of each data point of 0.02 V for this fitting. Figure 4.32 shows a selected two-α event fitted by Eq. (4.47). In order to identify the two particles, we selected events that satisfied the following requirements:

- Each minimum voltage $V_{\rm min}$ is within the range of -0.3 V $\leq V_{\rm min} \leq -1.1$ V.
- The timing difference between two particles is greater than the uncertainty of each μ.
- The χ^2 value is less than 700 (NDF = 557).

These requirements were used in a previous experiment with the SHARAQ spectrometer as a test for two-particle detection [42]. In this analysis, we could identify two α particles separated bt more than 5 mm in the CRDCs for the vertical direction.

The hit position for each α particle was determined from the drift time measured by the TDC and including μ_1 and μ_2 as fitting parameters determined from the flash-ADC data. The timing value we used is based on the TDC-determined vertical hit position of a particle that first arrived at anode wire. Since the timing corresponded to the rise time of the first signal in the flash-ADC data, the position of the other particle was determined by the time difference $\mu_2 - \mu_1$. Accordingly, the hit position of the second particle

was

$$y_2 = y_1 + v_{\rm drift}(\mu_2 - \mu_1), \tag{4.46}$$

where $v_{\rm drift}$ is the drift velocity determined by a calibration of the S2PL0 plastic scintillator.

Horizontal Direction

In order to identify the position of the two α particles in the horizontal direction, we used the sum of the SECHS function to fit the charge distribution of the cathode pads.

$$F_{\rm 2p}(x) = f(x|a_1, \mu_1, \sigma_1) + f(x|a_2, \mu_2, \sigma_2), \tag{4.47}$$

where $f(x|a, \mu, \sigma)$ is given in Eq. (4.14).

Parameters in the $f(x|a, \mu, \sigma)$ for the single α particle were determined in the same manner of the pulse shape of anode wires for the vertical direction. Figure 4.33 (a) shows the correlation between the charge of the CRDC1-1 cathode plane and the charge of plastic scintillator S2PL1. Events in this figure are selected by a software gate of ToF as shown in Fig. 4.25. The loci of the triton, α and ^{6}Li are clearly seen. The blue, red and green solid lines in Fig. 4.33 (b) represent distribution of the charge of the cathode selected by the cut of each particle as shown in Fig. 4.33 (a).

In order to estimate the rate at which we misidentified tritons and ^{6}Li particles as α particles, we followed a similar procedure to the one we described for the vertical direction. However, here we assumed a Gaussian distribution for ^{6}Li since its charge was saturated. Once again, as shown in Fig. 4.33 (c), the portion of events which were misidentified was 0.22% of the total, which is negligibly small.

The fitting parameters σ_1 and σ_2 determined for a single α were the fixed to fit the two α particles. Once again, the error on the charge in each cathode pads was properly assigned. Figure 4.34 shows the typical charge distribution of two α particles and the fitted curve using the $F_{\rm 2p}(x)$ function. In order to identify two α particles, we selected events satisfied following requirements:

- The peak charges for the α particles were 200 ch $\leq Q_{\rm max} \leq$ 650 ch.
- The distance between the two particles was greater than the uncertainty of the sum of μ_1 and μ_2.
- The χ^2 value was less than 900 (NDF=252).

In this analysis, we could identify two α particles separated more than 10 mm in the CRDCs in the horizontal direction.

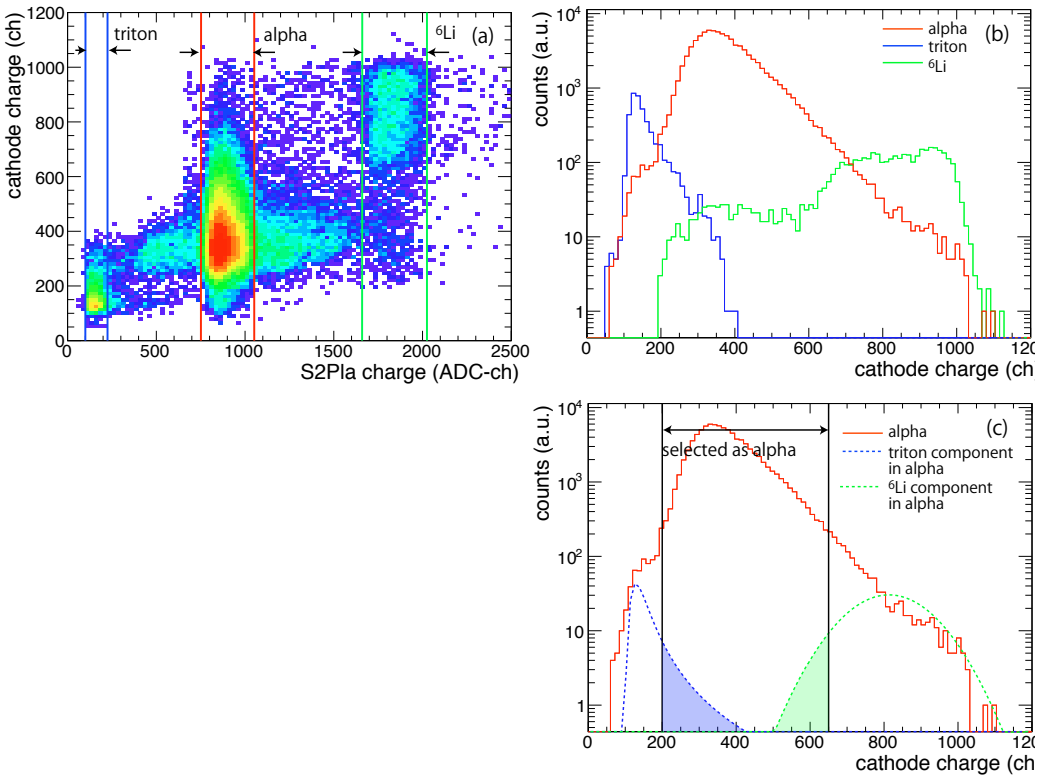

Figure 4.33: (a) The correlation between the charge of CRDC1-1 cathode plane and the charge of plastic scintillator S2PL1. (b) The blue, red and green solid lines represent distributions of charge of the CRDC1-1 cathode plane for the charge of triton, α and ^{6}Li particle, respectively. (c) The blue and green dashed line represent the component of the triton and ^{6}Li particle determined by fitting the distribution of α events (red solid line).

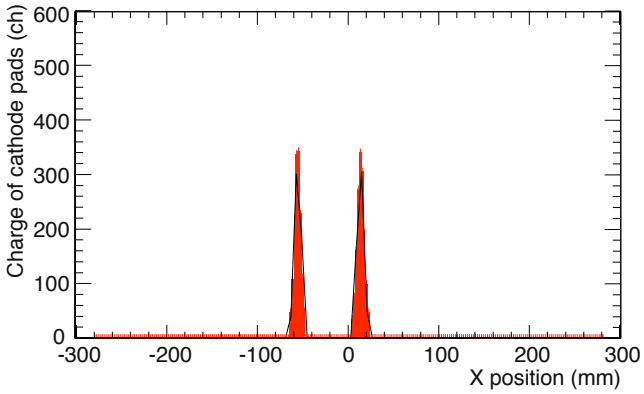

Figure 4.34: A sample of a charge distribution for two α particles and a fitted curve using the sum of the SECHS functions (Eq. (4.47)).

Vertical Position by Difference of the Drift Time

In this experiment, the detection efficiency of the flash-ADC was 25% due to trouble with the local trigger on the flash-ADCs. For this reason, we used the difference between the timing of two CRDCs to determine the vertical position for each of the two α particles as an alternative method. For two α events selected by the horizontal position, we determined the vertical position using information from flash-ADC, if the data were acquired correctly. If the data were not acquired correctly, we used the difference of the drift time as the vertical position of the two α particles.

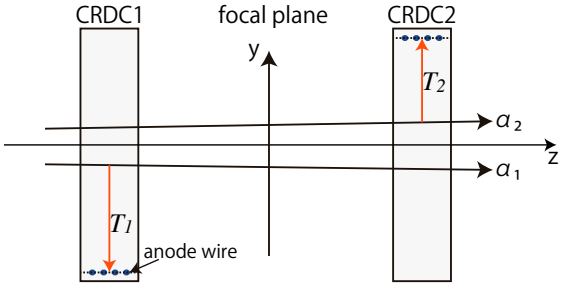

Figure 4.35: A schematic diagram of the procedure used to determine the position of two α particles based on the drift time of the CRDCs.

Figure 4.35 shows a schematic picture of the process of we used to determine the position of two α particles. If two α particles were parallel to

the focal plane, the position of a particle that first arrived at the anode wire (α_1 in Fig. 4.35) of CRDC1 was determined as $T_1 \times v_{\rm drift}$ by the drift time at CRDC1 (T_1). The other particle (α_2) was a particle that first arrived at CRDC2 (T_2), so that the position was determined by the CRDC2 as $T_2 \times v_{\rm drift}$. Considering the ion optical condition, the resolution of the position was $\Delta y = 4.7$ mm. Furthermore, two-particle events whose trajectories have cross points between the CRDCs were less than 1 % in the Monte Carlo simulation. The difference in the vertical positions of those events is less than Δy. This uncertainty was considered to be the resolution to reconstruct the invariant mass of the ^{8}Be in the following section (Sec. 4.4.6).

Obtained Event Snapshot

Figure 4.36 shows the curve of the charge distributions of the cathode pads (left) and the anode pulse shape (right) in a typical two-α event. Two particles were clearly identified in the horizontal and vertical directions, respectively.

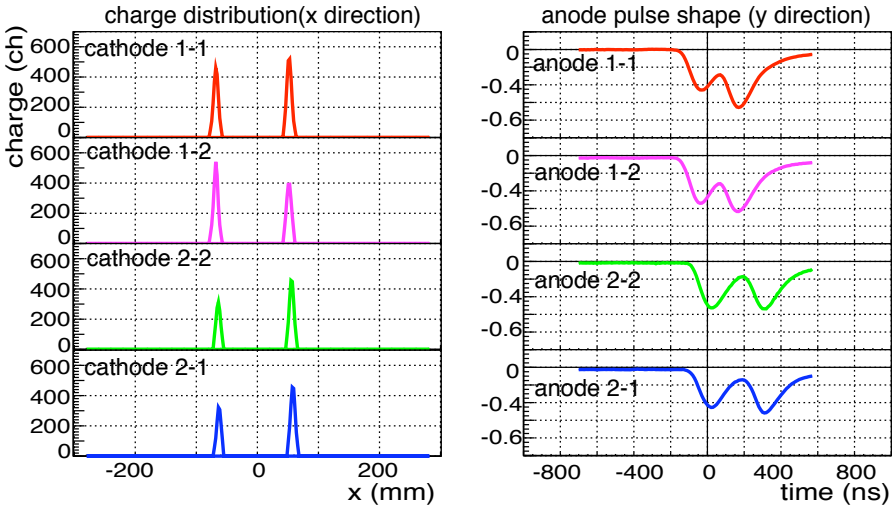

Figure 4.36: A sample of signals for the fitted curve of charge distribution of cathode pads and an anode pulse of the CRDCs for each plane. Two α particles were clearly identified.

Figure 4.37 shows reconstructed trajectories of the two α particles in the event shown in Fig. 4.36. We identified two α particles which separated more than 10 mm for horizontal direction and 5 mm for vertical direction respectively in this analysis.

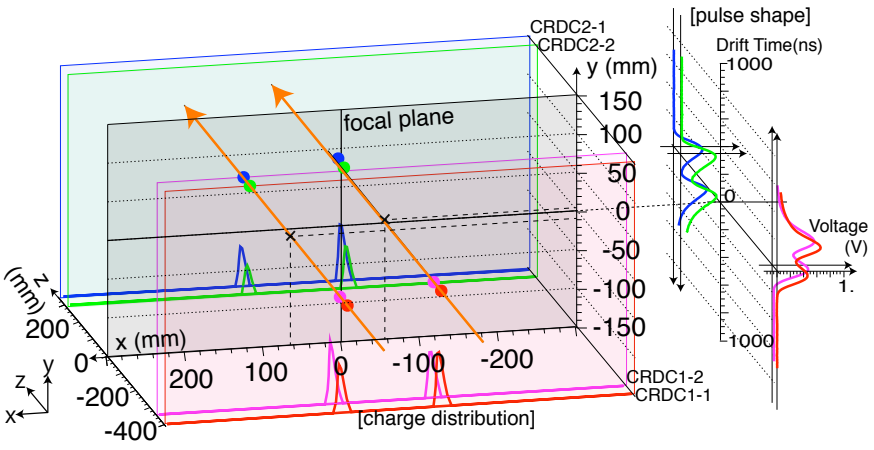

Figure 4.37: A snap shot of a typical two-α event reconstructed by the signals of Fig. 4.36.

Trajectories of the two α particles were described as $\vec{r_1} = (x_1, y_1)$ and $\vec{r_2} = (x_2, y_2)$. On the other hand, since we detected the horizontal and vertical position independently, alternative trajectories $\vec{r_1}' = (x_1, y_2)$ and $\vec{r_2}' = (x_2, y_1)$ were also possible. However, these two cases were not discriminated in this analysis, since exact trajectories were negligible in reconstructing the invariant-mass of the ^{8}Be and the missing-mass of the four-neutron system.

4.4.5 Examination of Accidental Coincidence at S2

There were about 70 cps of α particles at S2 during the experiment produced by the fragmentation reaction at the target. In order to exclude accidental coincidence of two α particles in the background, we examined two α particles detected in coincidence using the timing information of the plastic scintillator at S2.

Plastic Signals by the Following Bunch

The CRDC has a possibility to detect particles from the following bunch of a triggered particle. These events create artificial signal(s) for the plastic scintillator at the timing of the following bunch(es). Then we selected the events with no signals of delay timing of a triggered bunch at plastic scintillator of S2. The signals of the plastics scintillator were acquired for the 1 μs after the trigger timing.

Fiducial Cut for the α Particle

In order to exclude events from the background, we used the timing information of the plastic scintillators at S2. If the two α particles from the ^{8}Be decay were true events in coincidence, the difference between the timing of the plastic scintillator from left PMT ($T_{\rm L}$) and right PMT ($T_{\rm R}$) had a correlation with the position in the S2 focal plane ($x_{\rm S2}$). We defined the difference in left-right timing of the plastic scintillator as $\Delta T = T_{\rm L} - T_{\rm R}$. Figure 4.38 (a) shows the correlation between the $x_{\rm S2}$ tracked by the CRDCs and the ΔT of the single-α events.

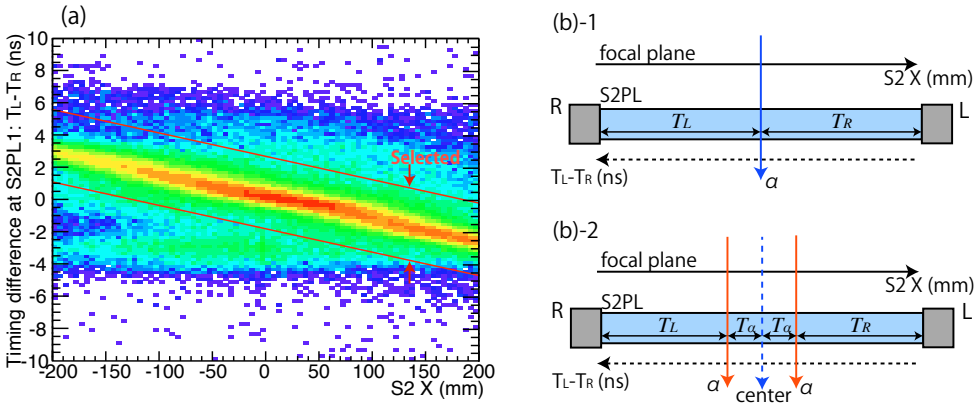

Figure 4.38: (a) The correlation between the horizontal position of S2 and the timing difference $T_{\rm L} - T_{\rm R}$ at plastic scintillator of S2. (b) A schematic diagram of the timing information from the left-right PMTs.

The number of uncorrelated events were less then 1/10000th of the correlated events. The uncorrelated events could also be from particles that passed through in the magnet on an unusual path.

If two particles hit the plastic scintillator, the difference in the left-right timing was the same as the central position of the trajectory (Fig. 4.38 (b-1)), which is given by

$$\Delta T = T_{\rm L} - T_{\rm R} \quad (4.48)$$
$$= (T_{\rm L} + T_{\alpha}) - (T_{\rm R} + T_{\alpha}), \quad (4.49)$$

where T_{α} is the timing difference between central position of the two α particles and one of the α particles as shown in Fig. 4.38(b)-2. We used this selection software gate to identify the two particles in coincidence at S2.

4.4.6 Reconstruction of the ^{8}Be Invariant-Mass Spectrum

We reconstructed the invariant mass spectrum of ^{8}Be from the angle and the momentum of the two α particles from selected events as previously described. The momentum and angle of the α particles were reconstructed by the ion optical information as described in Sec. 4.3.

The excitation energy (decay energy), $E_{^8\mathrm{Be}}$, was described as

$$E_{^8\mathrm{Be}} = M_{^8\mathrm{Be}} - 2M_\alpha, \tag{4.50}$$

where M_α is the rest mass of an α particle and $M_{^8\mathrm{Be}}$ is the invariant-mass of ^{8}Be reconstructed from the two α particles. The invariant mass of ^{8}Be was described by the momentum, p_α, and angle, θ, of the two α particles as

$$M^2_{^8\mathrm{Be}} = (M_\alpha + M_\alpha)^2 + 2(E_{1\alpha}E_{2\alpha} - M_\alpha M_\alpha - p_{1\alpha}p_{2\alpha}\cos\theta). \tag{4.51}$$

The momenta of the α particles, p_α, and the opening angle, θ, were determined by calculating of invert transfer matrix and the position and angle at S2.

Figure 4.39 (a) shows the correlation between the opening angle and momentum difference of the two α particles from the selected events. Figure 4.39 (b) shows the invariant-mass spectrum of the selected events. The excitation energy of the ground state and first excited state are 0.092 MeV and 3.03 MeV respectively. The resolution of angle was about 6.0 mrad (FWHM) and 7.9 mrad (FWHM) for the horizontal and vertical directions. In addition, there was an ambiguity in the position of 4.7 mm (sigma) and angle of 5.8 mrad (sigma) for the vertical direction at S2, since the difference of the position was determined by the drift time distance between the CRDC1 and CRDC2. The momentum resolution was about 1/2000 (σ), however the energy loss straggling, which was a maximum of 0.217 MeV for an α particle at the liquid He target (123 mg/cm^2) was large in comparison with the excitation energy of 0.092 MeV from the ground state of ^{8}Be. Although there was a concentration near the ground state of ^{8}Be energy at 0.98 MeV, the resolution of this spectrum of the excitation energy of ^{8}Be was not good enough and statistics were too small to properly separate the ground state and first excited state of ^{8}Be and the background.

In order to compare the result with the simulation, we generated events from the decay of ^{8}Be and reconstructed the invariant-mass with the angular and momentum resolutions and energy loss straggling at the target. Figure 4.40 shows the simulated events of ^{8}Be for (a) the angle and momentum correlation and (b) the invariant-mass spectrum of the ^{8}Be. In Fig. 4.40 (b),

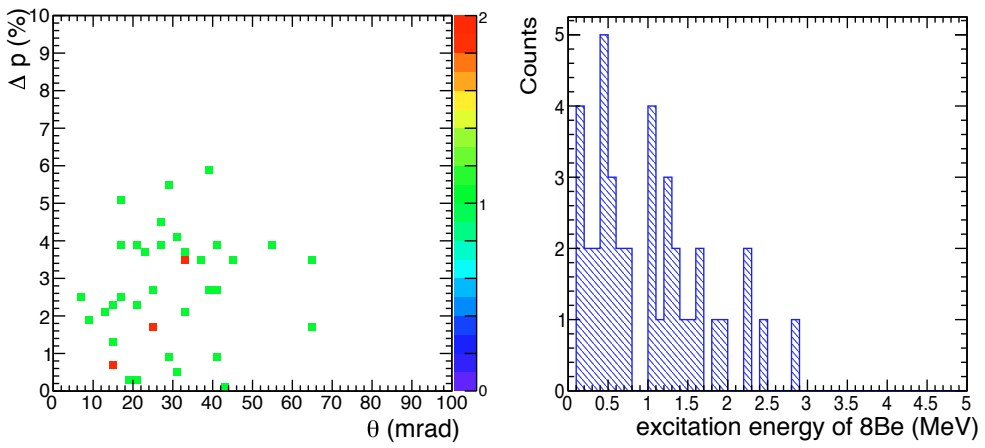

Figure 4.39: (a) The correlation between the opening angle and momentum difference of the two α particles for the selected events. (b) The invariant-mass spectrum of the selected events.

the blue dashed line and red dashed line represent the reconstructed spectrum from the ground and first excited state of ^{8}Be, respectively. The number of seed of simulated events of the ground state and first excited state was same in this simulation. The width of the ground state was 5.6 eV and first excited state was 1.51 MeV. To generate the first excited state, we assumed the energy density function in Ref. [51], which is suitable for reproducing the nuclear levels near a threshold. In this simulation, various resolutions of the experiment were considered. The angular resolution was 6.0 mrad (FWHM) and 7.9 mrad (FWHM) for the horizontal and vertical reconstructed angles at S0 respectively The momentum resolution was 1/2000 (σ) with an energy loss straggling at the target of 0.217 MeV at maximum. In addition, the position resolution of 4.7 mm at S2 for the vertical direction was considered since the position of two α particles were determined from the difference in the drift time, not the flash-ADC (Sec. 4.4.4). The energy loss straggling was calculated with the assumption that the reaction point for the beam axis was uniform in the target.

In addition, we estimated the shape of background. We generated the events from the distribution of the single-α events at the S2 produced by the ^{8}He beam during the physics measurement. Then two random events were chosen at random and reconstructed invariant-mass in the same manner as the previous description of the simulation.

Figure 4.40 (c) shows the correlation between the opening angle and the momentum difference of the two random α particles. Figure 4.40 (d) shows

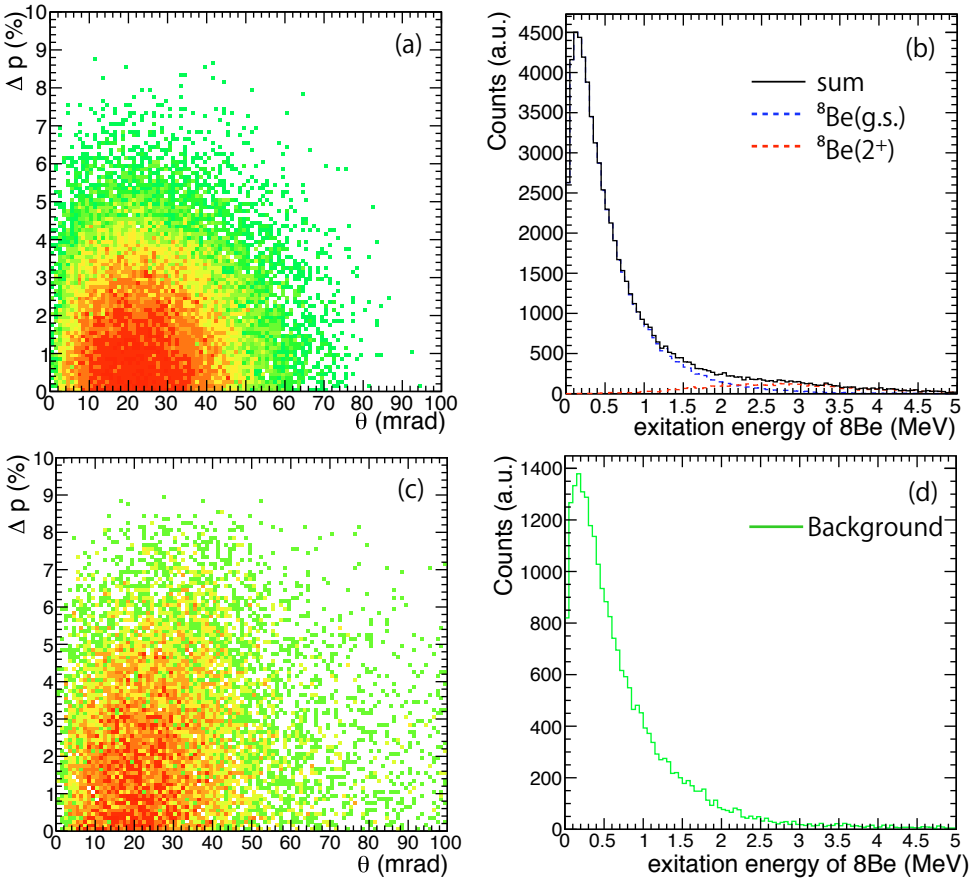

Figure 4.40: The simulated spectrum of (a) the correlation between the opening angle of the two α and momentum difference and (b) excitation energy of the ground state and first 2^{+} state of ^{8}Be. (c) The correlation between opening angle of the two α particles and momentum difference. (d) The excitation energy of the random two α particles from measured data set.

the the shape of reconstructed spectrum from the two random α particles. The shape was similar to the simulated ground state of ^{8}Be. We could not separate the background events from the true events with ^{8}Be with these small statistics.

4.5 Reconstruction of 4n Missing-Mass Spectrum

4.5.1 Energy Calibration

For the energy calibration of the excitation energy of the four-neutron system, we used the S2 horizontal position of known peak of the ^{8}Li (1^{+}) state produced by the ^{8}He(p,n) reaction at the FH10 plastic scintillator and a scaling of magnetic rigidity of the SHARAQ spectrometer.

Calibration using the Known Peak of ^{8}Li

We determined the relation between the position of 1^{+} state of ^{8}Li at S2 in the magnetic setting for ^{8}Li measurement and the position of the ground state (g.s.) of ^{8}Be in the ^{8}Be setting. The position of ^{8}Li(1^{+}) and ^{8}Be(g.s.) at the S2 were expressed as $x_{S2}^{^{8}\mathrm{Li}}$ and $x_{S2}^{^{8}\mathrm{Be}}$ respectively. The magnetic rigidity at the ^{8}Li setting and ^{8}Be setting was expressed as $B\rho^{^{8}\mathrm{Li}}$ and $B\rho^{^{8}\mathrm{Be}}$ respectively. The scaling factor between the magnetic setting at ^{8}He beam and ^{8}Li beam is therefore,

$$R_{B\rho} = \frac{B\rho^{^{8}\mathrm{Be}}}{B\rho^{^{8}\mathrm{Li}}}. \tag{4.52}$$

If we know the absolute value of the momentum of ^{8}Li(1^{+}) at the S2, which was expressed as $p^{^{8}\mathrm{Li}}$, the particles having a momentum of

$$p' = R_{B\rho}\, p^{^{8}\mathrm{Li}} \tag{4.53}$$

were reaching at $x_{\mathrm{S2}}^{^{8}\mathrm{Li}}$ in the magnetic setting of ^{8}Be. On the other hand, the ^{8}Be(g.s.) had an momentum expressed as $p^{^{8}\mathrm{Be}}$, which was reaching $x_{\mathrm{S2}}^{^{8}\mathrm{Be}}$. Then, the position of ^{8}Be(g.s.) $x_{\mathrm{S2}}^{^{8}\mathrm{Be}}$ was shifted from $x_{\mathrm{S2}}^{^{8}\mathrm{Li}}$ by the momentum difference

$$\Delta p = \frac{p' - p^{^{8}\mathrm{Be}}}{p'}. \tag{4.54}$$

Consequently, we deduced the $x_{\mathrm{S2}}^{^{8}\mathrm{Be}}$ as

$$x_{\mathrm{S2}}^{^{8}\mathrm{Be}} = x_{\mathrm{S2}}^{^{8}\mathrm{Li}} + \Delta p\ (x|\delta)_{\mathrm{SH}}, \tag{4.55}$$

where $(x|\delta)_{\rm SH}$ is the element of the transfer matrix for the momentum dispersion described in Sec. 4.3.

The scaling factor, $R_{B\rho}$, was calculated from the measured data of the magnetic field and the NMR value. We calculated deduced an absolute value of $p^{^{8}\rm Li}$ from the readout value of the NMR of the dipole magnet DH8 (see Fig. 3.2), which was the last dipole magnet before the secondary target. In order to calculate $p^{^{8}\rm Li}$ precisely, we considered (1) all of energy loss of the material in the path of the beam, (2) the Q-value (9.869 MeV) of the ^{8}He(p,n)^{8}Li reaction and (3) a reduction of mass of ^{8}Li from de-excitation of the γ ray of ^{8}Li(1^{+}) (0.98 MeV) state. These calculation was carried out by the LISE++ [52]. In the same manner, the $p^{^{8}\rm Be}$ was calculated from the NMR of the DH7 (Fig. 3.2), which was common setting for both the ^{8}Li and ^{8}Be.

The peak position of the ^{8}Li(1^{+}) state was determined as shown in Fig. 4.41. Events produced by the reaction were selected in the same manner as the particle identification of ToF between FH10 and S2 and the energy loss of the plastic scintillator at the S2.

Figure 4.41 (a) shows the correlation between $x_{\rm S2}$ and $x_{\rm F6}$. The inclination of the dashed line represents the ratio of the momentum dispersion, which is expressed as $(x|\delta)_{\rm BL}/(x|\delta)_{\rm SH}$. The histogram was projected along the dashed line, then the position at S2 corrected by the spread of the momentum of the beam was obtained. Figure 4.41 (b) is the correlation between the horizontal position at S2 corrected by the F6 position and scattering angle. The dashed curve represents the kinematic correlation in this reaction. The events had an reasonable correlation along this curve. The position shown in Fig. 4.41 (c) was corrected along the kinematical curve. From the spectrum of Fig. 4.41 (c), we obtained the value of $x_{\rm S2}^{^{8}Li}$ by fitting it with a Gaussian function.

Uncertainty of the Calibration

For the systematic error, we estimated the uncertainty of the calibration from the uncertainty of the magnetic rigidity of the dipole magnet and the peak position of the ^{8}Li know state.

There were two dipole magnets in the SHARAQ spectrometer. The uncertainty of the scaling factor $R_{\rm B\rho}$ arising from these two dipole magnets was estimated as 3.23×10^{-2}% from the data of NMR and magnetic field measurements. The error propagation was calculated along the Eq. (4.52) to Eq. (4.55). The error of $\Delta p(x|\delta)_{\rm SH}$ in Eq. (4.55) was estimated as $\pm$1.89 mm, which corresponds to $\pm$0.86 MeV.

The error in the $x_{\rm S2}^{^{8}\rm Li}$ was estimated from the error of the fitting of the peak

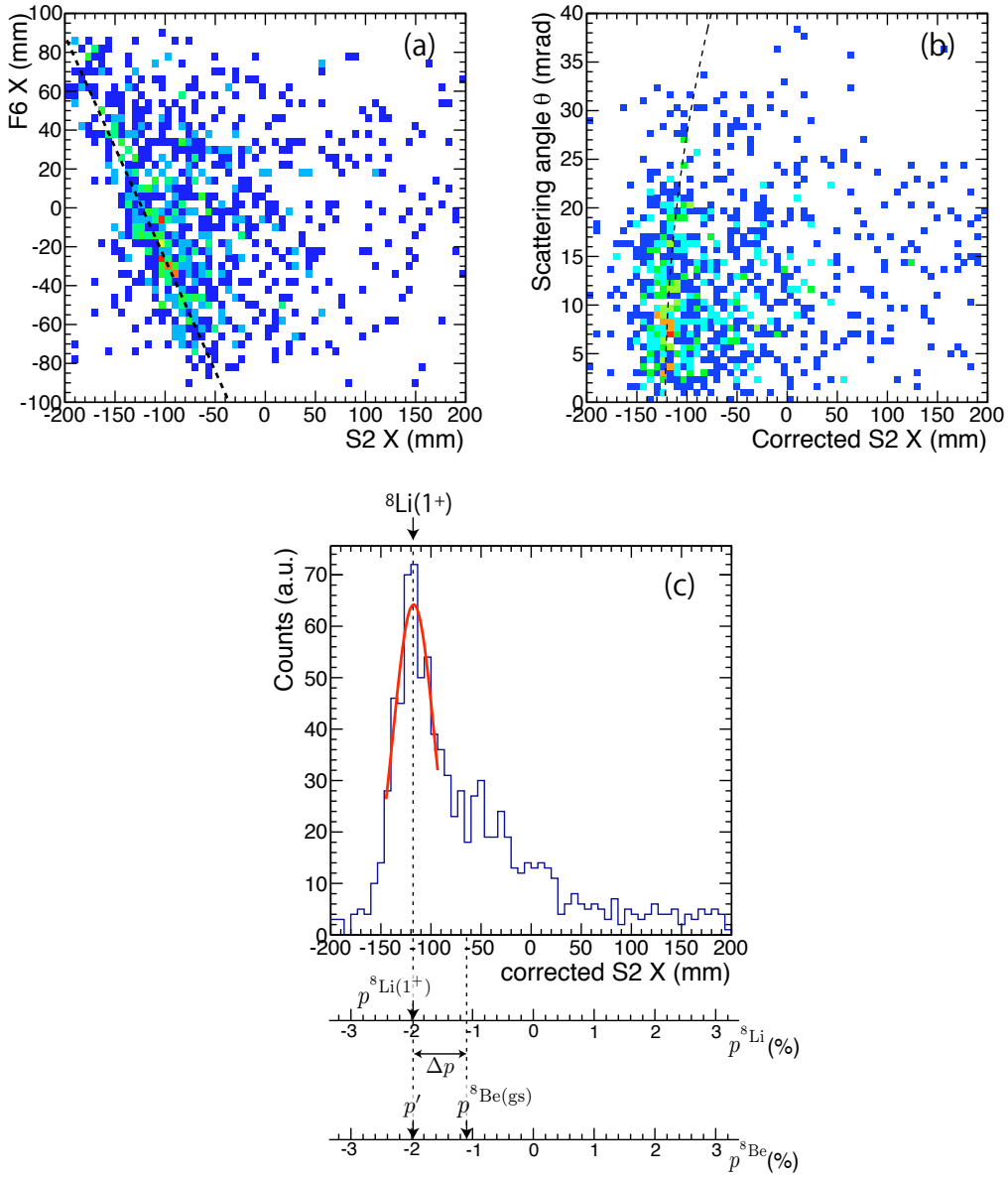

Figure 4.41: Known peak of the ^{8}Li produced by the ^{8}He(p,n) reaction at the FH10 plastic scintillator. (a) The correlation between F6 and S2 position for the horizontal direction. The dashed line represents the center of loci. (b) The correlation between the S2 position corrected by the F6 position and scattering angle with kinematical curve. The dashed line represent kinematical correlation in this reaction. (c) The position at S2 corrected by the F6 position and scattering angle.

(Fig. 4.41 (c)). We estimate that this error is ±2.0 mm, which corresponds to ±0.92 MeV.

Finally, from these estimate, the systematic uncertainty of the calibration was estimated at ±1.25 MeV.

4.5.2 Momentum of the Beam and Ejectile

The momentum of ^{8}Be was determined from the central ray of the two α particles at S2. There was a correlation between the momentum of the beam and momentum of the reaction products. When we calculated the missing-mass spectrum, we used the the momentum of ^{8}Be corrected using the ^{8}He beam.

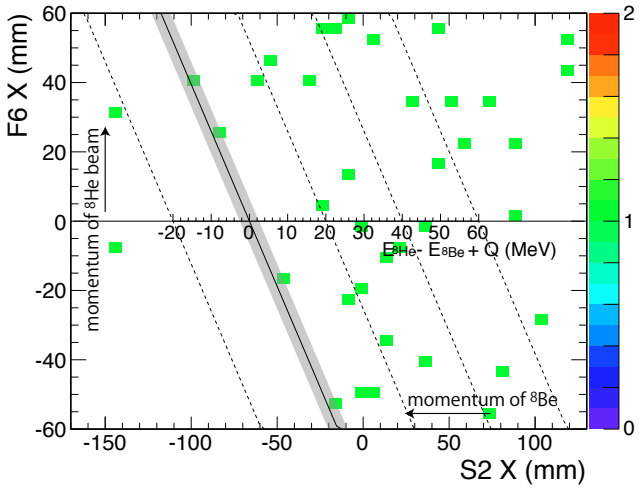

Figure 4.42: The correlation between the horizontal position at S2 and the horizontal position at F6. The solid and dashed diagonal lines correspond to the excitation energy of the 4n system.

Figure 4.42 shows the correlation of candidate events between the horizontal positions of F6 and S2, which correspond to the momentum of the ^{8}He beam and the momentum of the ^{8}Be ejectile respectively. The solid line corresponds to the threshold of four-neutron system (excitation energy of four-neutron system: $E_{4n} = 0$ MeV). The dashed and solid lines correspond to each excitation energy of the four-neutron system.

The events that decay to four neutrons have a positive excitation energy. We can clearly see the the difference in the number of events per unit area in the $E_{4n} \geq 0$ MeV and $E_{4n} < 0$ MeV region, although there were also two events in an unphysical region

4.5.3 Corrections

In order to calculate the missing-mass spectrum, we corrected the invariant-mass of ^{8}Be and the kinematical condition of the ^{8}Be ejectile.

Invariant-Mass of ^{8}Be

In order to reconstruct the missing-mass of the four-neutron system, the mass of the ^{8}Be was corrected from the invariant-mass of ^{8}Be. The excitation energy (decay energy) $E_{^{8}\mathrm{Be}}$ was described in Eqs. (4.50) and (4.51).

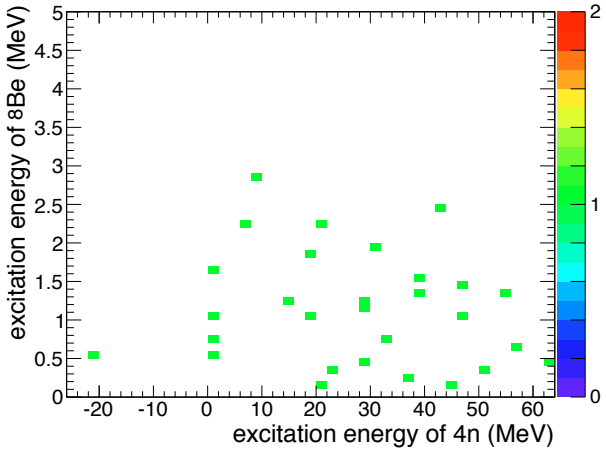

Figure 4.43: The correlation between the corrected missing-mass of 4n and the excitation energy of ^{8}Be.

Figure 4.43 shows the correlation between the excitation energy of the four-neutron system corrected from the excitation energy of ^{8}Be and the invariant-mass of the ^{8}Be. There was no bias in the excitation energy of ^{8}Be depending on the excitation energy of four-neutron.

Scattering Angle

We applied the kinematical correlation between the scattering angle and the momentum of the ejectile particle. The relationship between an observed momentum p, which corresponds to the horizontal position of S2, and the scattering angle θ was expressed as

$$p = p_0 \left(1 - \frac{\theta^2}{2(\beta_0/\beta - 1)}\right), \tag{4.56}$$

where p_0 and β_0 are the outgoing momentum and the beta factor for 0 degree scattering respectively. We calculated the momentum p corrected by the scattering angle θ.

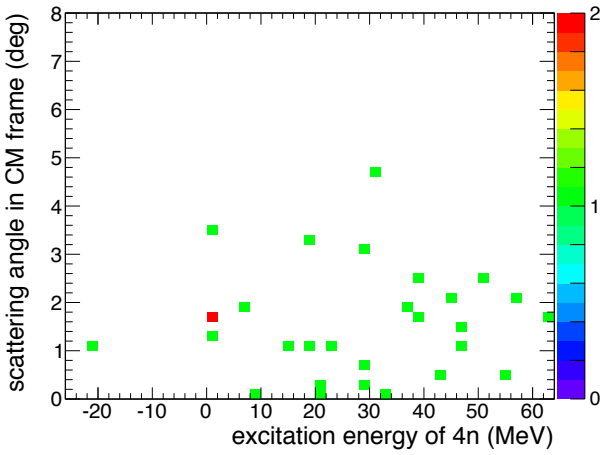

Figure 4.44: The correlation between the corrected missing-mass of the four-neutron system and the scattering angle of ^{8}Be in the center-of-mass frame.

Figure 4.44 shows the correlation between the corrected value of the excitation energy of the four-neutron system and the scattering angle of the center-of-mass frame of outgoing the ^{8}Be particle. There was no bias and of scattering angle depending on the excitation energy of four-neutron system. The scattering angle for almost all events is less than 5 degrees in the center-of-mass frame, which is expected.

The relationship between the scattering angle of the outgoing ^{8}Be in center-of-mass system ($\Theta_{\rm CM}$) and the laboratory system ($\theta_{\rm lab}$) was described as

$$\tan\theta_{\rm lab} \simeq \frac{\sin\Theta_{\rm CM}}{\gamma\left(\cos\Theta_{\rm CM} + \frac{\beta}{\beta_{\rm b}}\right)}. \tag{4.57}$$

Excitation Energy of Four-Neutron System

Finally, we corrected for the difference of the recoil momentum of ^{8}Be, which depended on the excitation energy of the four-neutron system. After these series of the corrections, we obtained the correct excitation energy of four-neutron system.

4.6 Background Estimation

We estimated the shape of the background in the missing-mass spectrum and absolute number of events from the analysis of the F6 MWDC.

4.6.1 Shape of Background Events in Missing-Mass Spectrum

We approximated the background as two random α particle events at S2. As described in Sec. 4.4.6, we choose the two-α-particle events at random from the data set of α particle taken during the measurement. We reconstructed the shape of the background using the same procedure and the same corrections as described in Sec. 4.5.3.

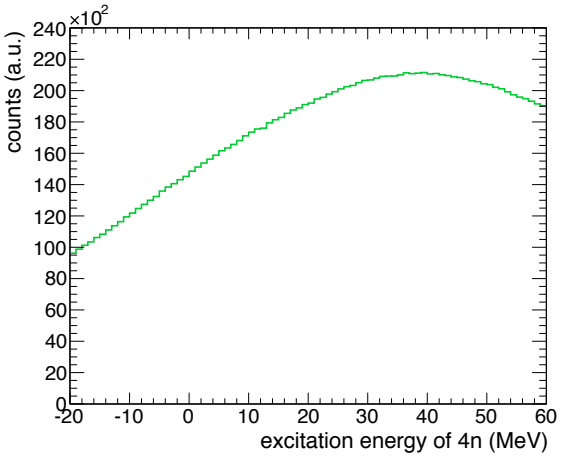

Figure 4.45: The background shape in the missing-mass of four-neutron produced with the data of single α particle.

Figure 4.45 shows the spectrum we obtained for the background. The single α event was distributed almost as a Gaussian distribution at S2. The average of the two α particles in this distribution formed a sharp Gaussian distribution.

4.6.2 Absolute Value of the Background Events

We estimated the absolute number of background events in the obtained missing-mass spectrum.

Failure of the Multi-Particle Rejection at F6

The multi-particle in a triggered bunch was considered a possible source of the background as discussed in Sec. 4.4.2. These events were rejected using the MWDC at F6. However, since the detection efficiency of the MWDC was limited to 86 %, multi-particle events contribute to the background in cases where one of the particles is detected while the other was not. We estimated the effect of these events on the multi-particle rejection in the missing-mass spectrum.

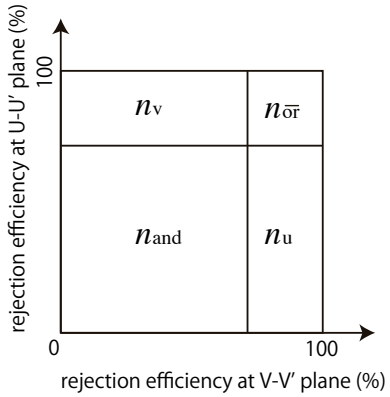

Figure 4.46: A schematic diagram of the Venn diagram of multi-particle rejection at F6 MWDC.

In order to determine the number of events, we consider the venn diagram of the number of rejected particle for each U-U′ and V-V′ plane as shown in Fig. 4.46. As described in Sec 4.2.1, the multi-particle triggered bunches could be rejected using the U-U′ and V-V′ planes independently. From the selection software gate of the candidate events, we obtained the number of events represented as n_{u}, n_{v} and n_{and}, where n_{u} and n_{v} is the number of rejected events in the selection cut of multi-particle rejection using the U-U′ and V-V′ planes, n_{and} is the number of events judged in the U-U′ and V-V′ planes, $n_{\bar{\mathrm{o}}\mathrm{r}}$, which we wanted to know, is the number of events still contained in the missing-mass spectrum as the background. Then we expressed the ratio of $n_{\bar{\mathrm{o}}\mathrm{r}}$ to the total number of events as

$$\frac{n_{\bar{\mathrm{o}}\mathrm{r}}}{N} = r_{\bar{\mathrm{o}}\mathrm{r}} = \left(\frac{n_{\mathrm{u}}}{n_{\mathrm{and}} + n_{\mathrm{u}}}\right)\left(\frac{n_{\mathrm{v}}}{n_{\mathrm{and}} + n_{\mathrm{v}}}\right), \tag{4.58}$$

where N is the total number of events of multi-particle in a trigger bunch,

which we could not know. Then the $n_{\bar{\text{or}}}$ was expressed as

$$n_{\bar{\text{or}}} = n_{\text{or}} \frac{r_{\bar{\text{or}}}}{1 - r_{\bar{\text{or}}}}, \tag{4.59}$$

where and $n_{\text{or}} = n_{\text{and}} + n_{\text{u}} + n_{\text{v}}$. From this relationship, we estimated the number of event as expressed as $n_{\bar{\text{or}}}$. We estimated the background events as

$$1.00 \pm 1.01 \quad \text{events} \tag{4.60}$$

in the region corresponding to $-25 < E_{4\text{n}} < 65$ MeV. Based on our analysis, we obtained the absolute number of the background events in the spectrum.

Multi-Particle in One Cell of MWDC at F6

Events with multi-particle in one cell of MWDC were not identified as two particles. These events therefore contribute to the background. The cell size of the MWDC at F6 was 9 mm for the U(30°) plane and 9 mm for the V(-30°) plane. The spot size of the beam was about ±50 mm in the vertical direction and ±80 mm in the horizontal direction as shown in Fig.4.23.

We estimated the ration of two particle events in a single MWDC using a simulation of the beam image. The data set taken during the measurement was used as a source of random events for the two particles. The number of such background events were estimated as

$$1.23 \pm 0.20 \quad \text{events} \tag{4.61}$$

in the $-25 < E_{4\text{n}} < 65$ MeV region of the missing-mass spectrum.

Other Possible Background Source

Another possible background source is from the misidentify other particles as α particles. However, these events were estimated to include less than 0.1% of events, corresponding to 0.05 events in this spectrum. This estimateion was described in Sec. 4.4.4.

Overall

In the previous analysis, we determined the number of background events to be

$$2.23 \pm 1.03 \quad \text{events} \tag{4.62}$$

aain the region corresponding to $-25 < E_{4\text{n}} < 65$ MeV of the missing-mass spectrum.

4.6.3 Differential Cross Section

The differential cross section of the ^{4}He(^{8}He,^{8}Be)4n reaction at 186 MeV/u is expressed as

$$\frac{d^2\sigma}{d\Omega dE} = \frac{Y}{N_{\rm beam}\ n_{\rm TG}\ \epsilon_{\rm det}\ \epsilon_{\rm DAQ}\ \Delta\Omega\ \Delta E}, \tag{4.63}$$

where Y is the yield of the four-neutron production events, $N_{\rm beam}$ is the total number of incident beam, $n_{\rm TG}$ is the number of particle in the target, $\epsilon_{\rm TG}$ is the total efficiency of detectors, $\epsilon_{\rm DAQ}$ is the live time of the DAQ system, $\Delta\Omega$ is the solid angle of the spectrometer and ΔE is bin of the excitation energy.

Chapter 5

Results and Discussion

5.1 Missing-Mass Spectrum of the 4n System

We detected 38 events produced by the ^{4}He(^{8}He,^{8}Be)4n reaction in the excitation energy $-25 < E_{4n} < 65$ MeV region. This spectrum was obtained after a series of corrections (see Sec. 4.5.3), while there were still 2.23 ± 1.03 background events in this region as estimated in Sec. 4.6.

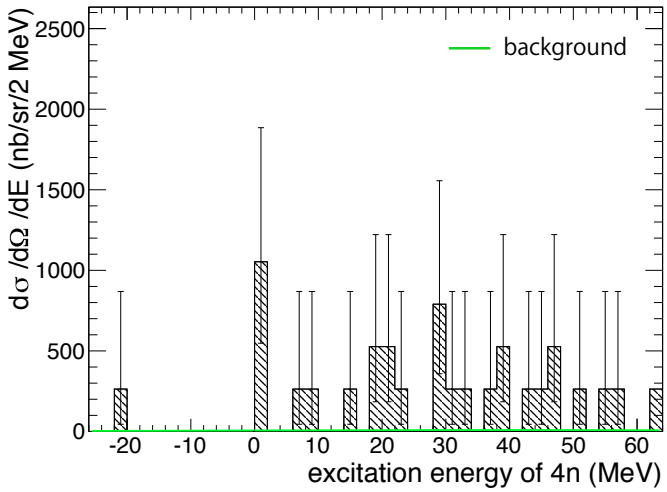

Figure 5.1: The missing-mass spectrum of the four-neutron system. The green line represents the estimated background.

Figure 5.1 shows the final missing-mass spectrum of four-neutron system. The excitation energy of $E_{4n} = 0$ MeV corresponds to the threshold of four-neutron decay. The green line represents the background spectrum estimate

in which the total number of the estimated background events are normalized by the cross section. The region of excitation energy of $-25 < E_{4n} < 65$ MeV was fully covered with the acceptance in this analysis (Sec. 4.3.5). The uncertainty of the energy calibration was estimated as ± 1.25 MeV (sigma) in previous section (Sec. 4.5.1). The resolution of the missing-mass spectrum was 1.16 MeV (sigma) estimated by the ion optical condition (Sec. 4.3).

There are two main components in this spectrum. One is the strength at the low energy region. There are 4 events in the $0 < E_{4n} < 2$ MeV region. Second is the continuum in the $E_{4n} \geq 2$ region. The mean of the strength at low energy region is

$$\hat{E}_{4n} = 0.83 \pm 0.25 \text{ MeV}. \tag{5.1}$$

Compared to the theoretical paper [1, 15], which predicted the possibility of the low energy resonance state around 2 MeV above the threshold, this value seems to be reasonable. However, it must be noted that there was an uncertainty in the energy calibration of ± 1.25 MeV in our experiment (Sec. 4.5.1). The significance of this strength and a shape of the continuum are discussed in following section.

5.2 Comparison with Theoretical Curves

In order to investigate the shape of the final spectrum, we fit the theoretical curve to the experimental data and evaluated the experimental data, including a complete statistical analysis.

Fitting for the Theoretical Curve

The upper panel of Fig. 5.2 shows the missing-mass spectrum fitted by the theoretical curves [53] and the background. The calculation assumes that the four-neutron system consists of two di-neutron pairs as the scattering state in the four-neutron decay. The idea of the calculation in Ref. [53] is based on the Ref. [54]. The reasons to employ this assumption are (i) the attractive interaction between neutrons is well-known as a di-neutron correlation [55], (ii) this is the simplest and most symmetric assumption and (iii) the previous study in Ref. [2] suggests that this assumption is the most probable case. In this calculation, the final state interaction between two neutrons (di-neutron) and between two di-neutrons are described with the effective range theory [55–57]. The scattering length of the di-neutron and the two di-neutrons are described as a_{2n} and a_{2n-2n}, respectively.

The fitting curves are for three different assumption about the correlation between neutrons. If the scattering length is $a = 0$ fm, there is no correla-

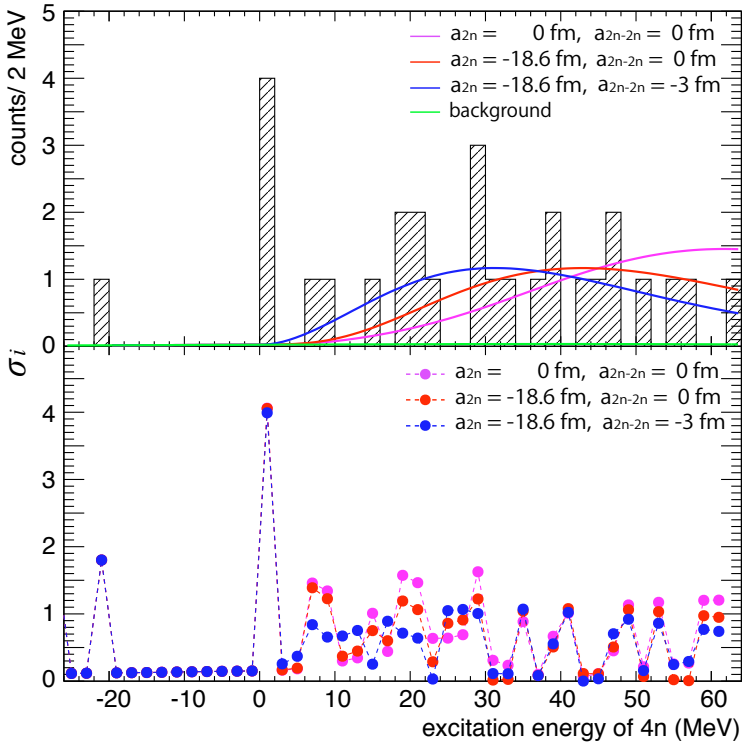

Figure 5.2: (a) The missing-mass spectrum of the four-neutron system fit with theoretical curves and the background function. The magenta line represents the curve without correlation of four neutrons. The red and blue lines represent the curves, which assume two di-neutrons with the scattering lengths $a_{2n-2n} = 0$ fm (no correlation) and $a_{2n-2n} = -3$ fm (attractive) respectively. (b) Evaluation of the goodness-of-fit for each bin using likelihood ratio test. The σ_i were defined in Eq. (5.4).

tion between the neutrons. On the other hand, if the scattering length a is negative, it means that there is an attractive final state interaction. The magenta line represents the curve assuming no correlation between the neutrons. The red line represents one with only a di-neutron correlation in each di-neutron, which is described by the known value of the scattering length $a_{2n} = -18.6$ fm [55]. The blue line includes the di-neutron correlation and the correlation between two di-neutrons described as the scattering length $a_{2n-2n} = -3$ fm, which is the weak attractive interaction.

The slope of the theoretical curve near the threshold depends on the scattering length. If the four neutrons decay into phase space without any correlation, the slope of the spectrum above the threshold is expected to rise proportional to $E_{4n}^{(7/2)}$ (Appendix B). On the other hand, if the decay is at a rate correlated, which include an attractive final state interaction, the phase space is reduced similar to a two body decay such as through two di-neutrons. An evaluation of the goodness-of-fit for these curves is discussed in following section.

Evaluation of Goodness-of-Fit for Each Bin

In order to estimate the bin-by-bin "goodness-of-fit" of the fitting curve, we used the likelihood ratio test χ^2_λ (Appendix C), which asymptotically follows a general χ^2 statistics. The likelihood ratio test is the statistical test based on the ratio of the likelihood function for two set of information: one is the data from the observed histogram and the other is a predicted curve. The test expresses statistical significance between two models. The χ^2_λ is defined as

$$\chi^2_\lambda = -2\ln\left[L(\boldsymbol{y};\boldsymbol{n})/L(\boldsymbol{n};\boldsymbol{n})\right] \tag{5.2}$$

$$= 2\sum_i \left[y_i - n_i + n_i \ln\left(n_i/y_i\right)\right], \tag{5.3}$$

where L is the likelihood function for the Poisson distribution, $\boldsymbol{n} = \{n_1, n_2, ..., n_i\}$ is the number of events in the i-th bin and $\boldsymbol{y} = \{y_1, y_2, ..., y_i\}$ is the number of events predicted by theoretical curve in the i-th bin. This method allows us to estimate the parameters and uncertainties identical to those in the method of maximum likelihood [58]. The χ^2_λ statistics is further useful for testing the goodness-of-fit since the value of its minimum will asymptotically obey a classical chi-square distribution, while a general chi-square minimization suffers under- or over- estimation of the area under the peak since this treatment has an assumption of Gaussian distribution of the errors implicitly. If the significance in the i-th bin is defined as

$$\sigma_i = \sqrt{y_i + n_i \ln\left(n_i/y_i\right)}, \tag{5.4}$$

where the σ_i asymptotically corresponds to the formula of the usual chi-square test $\chi^2 = \sum_i (y_i - n_i)^2/2\sigma$ assuming the Gaussian distribution.

The lower panel of Fig. 5.2 shows σ_i for each fitting curve. Note that we can clearly see an enhancement in $\sigma_i \simeq 4$ at the low energy region in comparison with the continuum of the theoretical curves. Whether the interaction between di-neutrons exists or not, it is a natural consequence when we assume the decay of the phase space, or in other words, that the missing-mass spectrum rises gradually from the threshold with an energy dependence of $E^{(7/2)}$ or $E^{(3/2)}$. This indicates that there is something causing the enhancement in low energy region beyond simple phase space decay.

The χ^2_λ was 45.7 for non-correlated curve, 40.6 for $a_{2\mathrm{n}-2\mathrm{n}} = 0$ fm and 36.1 for $a_{2\mathrm{n}-2\mathrm{n}} = -3$ fm with di-neutron correlation while the number of degree of freedom was 39. The difference of goodness-of-fit between the two theoretical curve is mainly due to the shape of the slope in the $0 < E_{4\mathrm{n}} < 20$ MeV region and the mean value of the $0 < E_{4\mathrm{n}} < 65$ MeV region. While the difference of the goodness-of-fit for each curve is not significantly, there is an possibility that the interaction between di-neutron and di-neutron is attractive.

5.2.1 Significance of the Strength at Low Energy

In order to evaluate the significance of the strength at low energy more carefully, we considered the "look elsewhere effect" [59]. The significance of observing a local strength must take into account the probability that such a strength originated from fluctuations of continuum elsewhere in the region. The "trial factor" was defined as the ratio between the probability of observing the strength excess at some fixed point and the probability of observing it anywhere in the region of interest. The region of interest was defined as [-2, 10] MeV, since it seemed impossible to observe the such a narrow resonance in the region of $E_{4\mathrm{n}} \sim 10$ MeV. If there is a resonance state in the $E_{4\mathrm{n}} > 10$ MeV region, the width is expected to be so large, it would be impossible to distinguish it from the continuum. In Ref. [59], the trial factor is asymptotically proportional to the effective number of independent search regions and to the significance in the fixed region.

The trial factor was estimated as described in Appendix D. The points indicated by triangle in Fig. 5.3 show the significance σ_i taking into account the "look elsewhere effect" for the two di-neutrons correlated curve ($a_{2\mathrm{n}} = -18.6$ fm, $a_{2\mathrm{n}-2\mathrm{n}} = -3$ fm) in Fig. 5.2. The points indicated by are the σ_i without this effect, which makes them the same as in Fig. 5.2. The trial factor below 1 sigma tends to be underestimated in the asymptotically approximation.

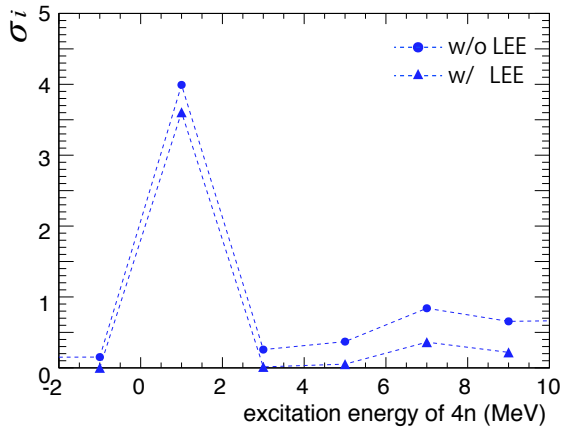

Figure 5.3: The circles represent the σ_i for the a_{2n} and a_{2n-2n} curve (blue line in Fig. 5.2). The triangles represent the one considered to the "look elsewhere effect" in the region of interest.

According to this evaluation, the significance the strength at low energies was 3.6 sigma. Indicating that the strength is clearly significant difference.

5.3 Momentum Transfer of Produced Events

One of the important aspects to investigate in the very weakly bound or unbound system is the momentum transfer. For this experiment, it is especially important since we can produce the four-neutron system with a small momentum transfer by the exothermic reaction as described in Sec. 2.1. The momentum transfer of the events produced in the ^{4}He(^{8}He,^{8}Be)4n reaction was shown in Fig. 5.4, which is reminiscent of Fig. 2.2. The momentum transfer corresponds to the scattering angle of the ejectiles. The red solid line and red shaded area represent the kinematically accessible region in this exothermic ^{4}He(^{8}He,^{8}Be)4n reaction. The red dashed line corresponds to $\theta = 1^\circ$ in the ^{4}He(^{8}He,^{8}Be)4n reaction. On the other hand, in order to compare with the previous experiment using the (π^-, π^+) reaction at 156 MeV [2], the blue line was represented in Fig. 2.2.

Note that momentum transfer for the 3 events between $0 < E_{4n} < 2$ MeV region is smaller than 35 MeV/c, which is the accessible region only with the exothermic reaction. As discussed in Sec. 2.1, this region was not allowed to access with endothermic reaction, for instance (π^-, π^+) reaction. We considered that we could obtain clear strength at the low energy region only our experiment.

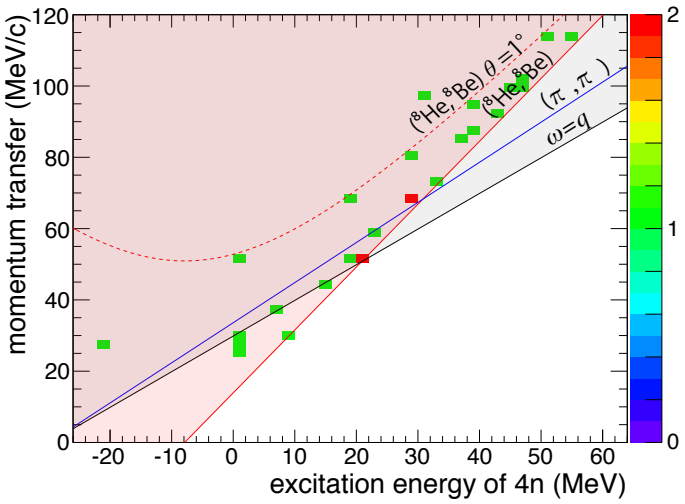

Figure 5.4: The relation between the excitation energy and momentum transfer at the reaction for the obtained events. The red solid line and red shaded area represent the accessible region in ^{4}He(^{8}He,^{8}Be)4n reaction. The red dashed line represents the $\theta = 1^\circ$ in ^{4}He(^{8}He,^{8}Be)4n reaction. The black line and gray shaded area represent the photon line and accessible region with endothermic reaction. The blue solid line represents the (π^-, π^+) reaction at 156 MeV.

Chapter 6

Conclusion

We performed a missing-mass measurement in order to investigate the four-neutron system via the exothermic double-charge exchange reaction ^{4}He(^{8}He, ^{8}Be)4n at 186 MeV/u. The exothermic reaction was expected to produce the four-neutron system with a small momentum transfer. The experiment was performed at the RIBF at RIKEN by using the BigRIPS-HRB beam line and the SHARAQ spectrometer.

We measured 38 events produced via the ^{4}He(^{8}He,^{8}Be)4n reaction in the missing-mass spectrum of the four-neutron system. The obtained missing-mass spectrum showed two components: one was strength in a low excitation energy region $0 < E_{4n} < 2$ MeV, while the other was the continuum in the $E_{4n} > 2$ MeV region. The shape and absolute value of the background events were estimated and there were only 2.23 $\pm$ 1.01 background events in the whole spectrum region, this was almost negligible compered to the selected 38 events.

The low energy region contained 4 events in total. This strength was clearly enhanced in comparison to the two theoretical curves, which assume the effective range theory with the decay of two correlated and non-correlated di-neutron clusters. The significance of this enhancement was estimated as 3.7 σ. Although there was an uncertainty on the energy calibration of $\pm$1.25 MeV, the mean of these events was 0.83 $\pm$ 0.25 MeV. This indicated a possibility for the low energy resonance state of tetra-neutron. The momentum transfer of some of these events was smaller than 35 MeV/c, which was kinematically accessible only by our exothermic reaction. The fitting result of the continuum region supports the model that there is a correlation between two di-neutrons.

Appendix A

Ion Optics

In this section, we describe the notation of the transfer matrix and ion optical analysis.

We defined the horizontal position as x, the horizontal angle as a, the vertical position as y, the vertical angle as a and the momentum difference from the central orbit as δ. A vector at the focal plane (FP) was defined as

$$\vec{X}_{\mathrm{FP}} = \begin{bmatrix} x_{\mathrm{FP}} \\ a_{\mathrm{FP}} \\ y_{\mathrm{FP}} \\ b_{\mathrm{FP}} \\ \delta_{FP} \end{bmatrix}. \tag{A.1}$$

The vector at the FP1 focal plane transferred from the focal plane FP0 is described using the transfer matrix R as

$$\vec{X}_{\mathrm{FP1}} = R\ \vec{X}_{\mathrm{FP0}}. \tag{A.2}$$

The elements in this transfer matrix are

$$\begin{bmatrix} x_{\mathrm{FP1}} \\ a_{\mathrm{FP1}} \\ y_{\mathrm{FP1}} \\ b_{\mathrm{FP1}} \\ \delta_{FP1} \end{bmatrix} = \begin{bmatrix} (x|x) & (x|a) & (x|y) & (x|b) & (x|\delta) \\ (a|x) & (a|a) & (a|y) & (a|b) & (a|\delta) \\ (y|x) & (y|a) & (y|y) & (y|b) & (y|\delta) \\ (b|x) & (b|a) & (b|y) & (b|b) & (b|\delta) \\ (\delta|x) & (\delta|a) & (\delta|y) & (\delta|b) & (\delta|\delta) \end{bmatrix} \begin{bmatrix} x_{\mathrm{FP0}} \\ a_{\mathrm{FP0}} \\ y_{\mathrm{FP0}} \\ b_{\mathrm{FP0}} \\ \delta_{\mathrm{FP0}} \end{bmatrix}. \tag{A.3}$$

Appendix B

Phase Space Decay of Multi-Body System

B.1 Phase Space

Fermi's Golden Rule in perturbation theory is described by

$$w_{i\to f} = \frac{2\pi}{\hbar}|\langle f|\Delta H|i\rangle|^2\rho_f. \tag{B.1}$$

This equation expresses that the cores section is proportional to the density in the final state, in other words, the phase space of the final state. The density is expressed as a function of the momentum space in the non-relativistic limit:

$$\rho_f(E) = \delta\left(E - \sum E_i\right)\prod_i \frac{d^3p_i}{(2\pi)^3 2m}, \tag{B.2}$$

where

$$d^3p = p^2\ dp\ d\Omega = \sqrt{2m^3}\sqrt{E}\ dE\ d\Omega. \tag{B.3}$$

From this equation, the energy spectrum of the 2-body system in the phase space decay is proportional to the square of energy as E^2.

B.1.1 3-Body Decay

The relative energy of the 3-body system is illustrated as in Fig. B.1. The total energy of the system is defined as E and expressed as $E = E_{12} + E_{3-12}$. From Eq. B.2, the phase space is described as

$$\rho(E) \quad = \quad \int \delta(E - (E_{12} + E_{3-12}))\sqrt{E_{12}}\sqrt{E_{3-12}}dE_{12}dE_{3-12} \tag{B.4}$$

$$= \int \sqrt{E_{12}}\sqrt{E - E_{12}} \tag{B.5}$$

$$\propto E^2. \tag{B.6}$$

This means that the the energy distribution of the 3-body system in phase space decay is a function of E^2.

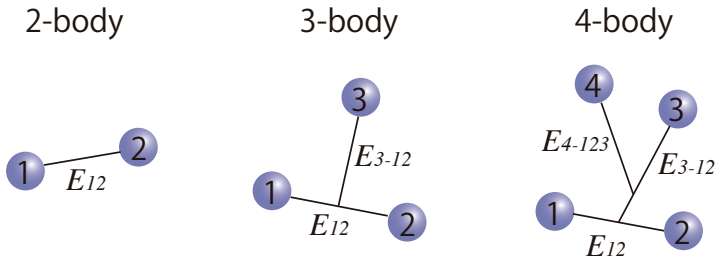

Figure B.1: A simple illustration of the relative energy of 2-body, 3-body and 4-body decay.

B.1.2 4-Body Decay

For the 4-body decay, we define the relative energy as shown in Fig. B.1 the same as in 3-body decay. This relation of the relative energy is assumed the to be the same for each of the 4-bodies. The total energy of the system is defined as $E = E_{12} + E_{3-12} + E_{4-123}$. The phase space is described using

$$\rho(E) = \int \delta(E - (E_{12} + E_{3-12} + E_{4-123}))\sqrt{E_{12}}\sqrt{E_{3-12}}\sqrt{E_{4-123}}\; dE_{12}\; dE_{3-12}\; dE_{4-123}$$

$$= \int \sqrt{E_{4-123}}\sqrt{E_{3-12}}\sqrt{E_{4-123} + E_{3-12} - E}\; dE_{4-123}\; dE_{3-12} \tag{B.7}$$

$$= \int \sqrt{E_{4-123}}(E - E_{4-123})^2 \tag{B.8}$$

$$\propto E^{7/2}. \tag{B.9}$$

This means that the the energy spectrum of the 4-body system in phase space decay is the function of $E^{(7/2)}$. Four neutron decay with non correlation decay is expected to follow this formula.

Appendix C

Likelihood Ratio Test

In order to estimate a "goodness-of-fit" for the fitting curves for bin-by-bin, we defined the likelihood ratio test χ^2_λ to follow a general χ^2 statistics. This method allow to estimate parameters and errors identical to those of method of maximum likelihood [58]. The χ^2_λ statistics is further useful for testing goodness-of-fit since the value of its minimum asymptotically obey a classical chi-square distribution, while the general chi-square minimization suffer under- or over- estimation of the area under the peak since this treatment has an assumption of Gaussian distribution of the errors implicitly.

The likelihood for of the histogram assuming the Poisson distribution was

$$L(\boldsymbol{y};\boldsymbol{n}) = \prod_i \exp(-y_i)\frac{y_i^{n_i}}{n_i!}, \tag{C.1}$$

where n_i is the number of events in the i th bin and y_i is the number of events predicted by theoretical curve in the i th bin. We defined the likelihood ratio as

$$\lambda = L(\boldsymbol{y};\boldsymbol{n})/L(\boldsymbol{m};\boldsymbol{n}), \tag{C.2}$$

where $\boldsymbol{m} = (m_1, m_2, ...m_i)$ is the true (unknown) value of the $\boldsymbol{n} = (n_1, n_2, ...n_i)$. We define the likelihood ratio test χ^2_λ as

$$\chi^2_\lambda = -2\ln\lambda. \tag{C.3}$$

We estimated the true values $\boldsymbol{m}$ by $\boldsymbol{n}$, then

$$\lambda = L(\boldsymbol{y};\boldsymbol{n})/L(\boldsymbol{n};\boldsymbol{n}) \tag{C.4}$$

$$= \prod_i \exp(-y_i + n_i)(y_i/n_i)^{n_i}. \tag{C.5}$$

After the deformation, we obtained

$$\chi^2_\lambda = 2\sum_i \left[y_i - n_i + n_i \ln\left(n_i/y_i\right)\right]. \tag{C.6}$$

If we defined σ_i as

$$\sigma_i = \sqrt{y_i + n_i \ln (n_i/y_i)}, \tag{C.7}$$

where σ_i corresponds to the formula of usual chi-square test: $\chi^2 = \sum_i (y_i - n_i)^2/2\sigma_i$ assuming a Gaussian distribution.

Appendix D

Look Elsewhere Effect

The "trial factor" is defined as

$$\text{trial\#} = \frac{p_{\text{anywhere}}}{p_{\text{fix}}}, \tag{D.1}$$

where p_{fix} is the probability of observing the signal strength at some fixed point and p_{anywhere} is the probability of observing it anywhere in the region of interest.

The most straightforward way to estimate the trial factor is using a Monte Carlo simulation to find a fluctuation in a continuum. However, this procedure consumes CPU power and time in the order of 10^7 loops corresponding to a 5 σ. Therefore, in Ref. [59], the trial factor is estimated by approximation as a function of effective number of independent search regions and a significance in the fixed region.

If the number of degrees of freedom is only a parameter of the signal strength, the trial factor is asymptotically approximated as

$$\text{trial\#} \sim 1 + \sqrt{\frac{\pi}{2}} N Z_{\text{fix}}, \tag{D.2}$$

where N is the number of local minima of the significance for each bin (σ_i), Z_{fix} is the significance in the fixed region The number of N is deduced by the set of 10^4 Monte Carlo simulation.

In this analysis, the region of interest was [-2, 10] MeV and the trial factor was obtained as shown in Fig. D.1. The probability taking into account this effect (p_{LEE}) of the each bin was estimated as

$$p_{\text{LEE}} = \text{Trial\#}(Z_{\text{fix}}) \times p_{\text{fix}}, \tag{D.3}$$

where p_{fix} is the probability of observing the strength in the fixed region. The square points in Fig. 5.3 were the significance corresponding to the p_{LEE}.

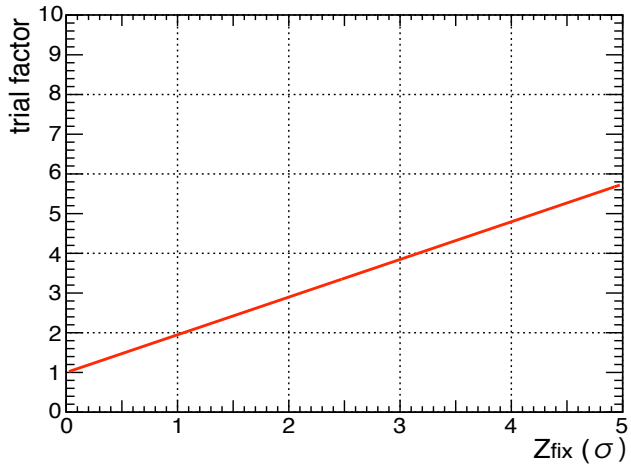

Figure D.1: Trial factor as a function of significance in the fixed region (Z_{fix}).

Bibliography

[1] S. Pieper, Physical Review Letters **90**, 252501 (2003).

[2] J. Ungar, R. Mckeown, D. F. Geesaman, R. J. Holt, J. R. Specht, K. E. Stephenson, B. Zeidman, and C. Morris, Physics Letters **144**, 333 (1984).

[3] K. H. Sun, F. A. Pecjak, and A. J. Allen, Physical Review **85**, 4 (1952).

[4] J. P. Schiffer and R. Vanderbosch, Physics Letters **5**, 292 (1963).

[5] S. Cierjacks, G. Markus, W. Michaelis, and W. Ponitz, Physical Review **137**, B345 (1965).

[6] W. Gibbs, B. Gibson, A. Hess, and G. Stephenston, Physical Review C **15**, 1384 (1977).

[7] T. P. Gorringe, S. Ahmad, D. S. Armstrong, R. A. Burnham, A. J. Larabee, C. E. Waltham, P. Depommier, and R. Poutissou, Physical Review C **40**, 2390 (1989).

[8] A. V. Belozyorov, C. Borcea, Z. Dlouhy, and a.M Kalinin, Nuclear Physics A **477**, 131 (1988).

[9] D. V. Aleksandrov, E. Y. Nikol, B. G. Novatski, S. B. Sakuta, and D. N. Stepanov, JETP Lett. **81**, 43 (2005).

[10] F. M. Marqués, M. Labiche, N. Orr, J. Angélique, L. Axelsson, B. Benoit, U. Bergmann, M. Borge, W. Catford, S. Chappell, N. Clarke, G. Costa, N. Curtis, A. D'Arrigo, E. de Góes Brennand, F. de Oliveira Santos, O. Dorvaux, G. Fazio, M. Freer, B. Fulton, G. Giardina, S. Grévy, D. Guillemaud-Mueller, F. Hanappe, B. Heusch, B. Jonson, C. Le Brun, S. Leenhardt, M. Lewitowicz, M. López, K. Markenroth, A. Mueller, T. Nilsson, A. Ninane, G. Nyman, I. Piqueras, K. Riisager, M. Laurent, F. Sarazin, S. Singer, O. Sorlin, and L. Stuttgé, Physical Review C **65**, 044006 (2002).

[11] N. K. Timofeyuk, Journal of Physics G **29**, 8 (2003).

[12] C. Bertulani and V. Zelevinsky, Journal of Physics G **29**, (2003).

[13] S. A. Sofianos, S. A. Rakityansky, and G. P. Vermaak, Journal of Physics G **23**, 1619 (1997).

[14] I. V. Simenog, B. E. Grinyuk, and Y. M. Bidasyuk, arXiv 8 (2005).

[15] Y. a. Lashko and G. F. Filippov, Physics of Atomic Nuclei **71**, 209 (2011).

[16] R. Jibuti, R. Y. Kezerashvili, and K. I. Sigua, Physics Letters **102**, 381 (1981).

[17] K. Arai, Physical Review C **68**, 034303 (2003).

[18] R. Wiringa and S. Pieper, Physical Review Letters **89**, 18 (2002).

[19] R. Wiringa, V. Stoks, and R. Schiavilla, Physical Review C **51**, (1995).

[20] T. Otsuka, T. Suzuki, J. Holt, A. Schwenk, and Y. Akaishi, Physical Review Letters **105**, 032501 (2010).

[21] H.-W. Hammer, A. Nogga, and A. Schwenk, Reviews of Modern Physics **85**, 197 (2013).

[22] I. Tews, T. Krüger, K. Hebeler, and a. Schwenk, Physical Review Letters **110**, 032504 (2013).

[23] K. Hebeler, J. M. Lattimer, C. J. Pethick, and a. Schwenk, Physical Review Letters **105**, 161102 (2010).

[24] J. Giovinazzo, B. Blank, M. Chartier, S. Czajkowski, A. Fleury, M. Lopez Jimenez, M. Pravikoff, J.-C. Thomas, F. de Oliveira Santos, M. Lewitowicz, V. Maslov, M. Stanoiu, R. Grzywacz, M. Pfützner, C. Borcea, and B. Brown, Physical Review Letters **89**, 102501 (2002).

[25] L. V. Grigorenko, I. G. Mukha, C. Scheidenberger, and M. V. Zhukov, Physical Review C **84**, 021303 (2011).

[26] T. Kubo, K. Kusaka, K. Yoshida, a. Yoshida, T. Ohnishi, M. Ohtake, Y. Yanagisawa, N. Fukuda, T. Haseyama, Y. Yano, N. Kakutani, T. Tsuchihashi, and K. Sato, IEEE Transactions on Applied Superconductivity **17**, 1069 (2007).

[27] T. Kawabata, G. Berg, T. Kubo, H. Sakai, S. Shimoura, and T. Uesaka, Nuclear Instruments and Methods in Physics Research Section B: Beam Interactions with Materials and Atoms **266**, 4201 (2008).

[28] T. Uesaka, S. Shimoura, H. Sakai, G. Berg, K. Nakanishi, Y. Sasamoto, a. Saito, S. Michimasa, T. Kawabata, and T. Kubo, Nuclear Instruments and Methods in Physics Research Section B: Beam Interactions with Materials and Atoms **266**, 4218 (2008).

[29] T. Uesaka, S. Shimoura, and H. Sakai, Journal of Physical Society of Japan 1 (2012).

[30] H. Ryuto, M. Kunibu, T. Minemura, T. Motobayashi, K. Sagara, S. Shimoura, M. Tamaki, Y. Yanagisawa, and Y. Yano, Nuclear Instruments and Methods in Physics Research Section A: Accelerators, Spectrometers, Detectors and Associated Equipment **555**, 1 (2005).

[31] Y. Yano, Nuclear Instruments and Methods in Physics Research Section B: Beam Interactions with Materials and Atoms **261**, 1009 (2007).

[32] S. Shimoura, Nuclear Instruments and Methods in Physics Research Section B: Beam Interactions with Materials and Atoms **266**, 4131 (2008).

[33] Y. Sasamoto, Ph.D. thesis, the University of Tokyo (2012).

[34] K. Kisamori, S. Shimoura, S. Michimasa, S. Ota, S. Noji, H. Tokieda, R. Yokoyama, and H. Baba, CNS Annual Report **90**, 68 (2013).

[35] M. Berz and K. Makino, COSY Infinity version 9 - user ' s guide and reference manual, COSY Infinity version 9 - user ' s guide and reference manual .

[36] H. Miya, S. Ota, T. Fujii, S. Kawase, Y. Kubota, C. Lee, H. Matsubara, K. Miki, a. Saito, S. Michimasa, T. Uesaka, H. Sakai, and S. Shimoura, Nuclear Instruments and Methods in Physics Research Section B: Beam Interactions with Materials and Atoms **317**, 701 (2013).

[37] S. Noji, Ph.D. thesis, the University of Tokyo (2012).

[38] Y. Kikuchi, S. Ota, H. Matsubara, Y. Kubota, C. Lee, S. Kawase, and T. Uesaka, CNS Annual Report **90**, 63 (2013).

[39] Y. Kikuchi, master thesis, the University of Tokyo (2012).

[40] H. Tokieda, master thesis, the University of Tokyo (2010).

[41] S. Michimasa, H. Tokieda, S. Noji, S. Ota, S. Shimoura, T. Uesaka, H. Sakai, P. Roussel-Chomaz, J. F. Libin, P. Gangnant, and C. Spitaels, CNS Annual Report **86**, 45 (2011).

[42] K. Kisamori, master thesis, the University of Tokyo (2012).

[43] Goodfellow Cambridge Ltd, http://www.goodfellow.com .

[44] S. Michimasa, Ph.D. thesis, the University of Tokyo (2006).

[45] H. Baba, T. Ichihara, T. Ohnishi, S. Takeuchi, K. Yoshida, Y. Watanabe, S. Ota, and S. Shimoura, Nuclear Instruments and Methods in Physics Research Section A: Accelerators, Spectrometers, Detectors and Associated Equipment **616**, 65 (2010).

[46] Artemis, Website will be opened .

[47] ROOT, A Data Analysis Framework, root.cern.ch .

[48] K. Miki, Ph.D. thesis, the University of Tokyo (2011).

[49] I. Endo, T. Kawamoto, Y. Mizuno, T. Ohsugi, T. Taniguchi, and T. Takeshita, Nuclear Instruments and Methods in Physics Research **188**, 51 (1981).

[50] Y. Lacouture and D. Cousineau, Tutorials in Quantitative Methods for Psychology **4**, 35 (2008).

[51] F. Barker and P. Treacy, Nuclear Physics **38**, 33 (1962).

[52] O. Tarasov and D. Bazin, Nuclear Instruments and Methods in Physics Research Section B: Beam Interactions with Materials and Atoms **266**, 4657 (2008).

[53] S. Shimoura, Private communication .

[54] L. V. Grigorenko, N. K. Timofeyuk, and M. V. Zhukov, The European Physical Journal A - Hadrons and Nuclei **19**, 187 (2004).

[55] R. Machleidt and I. Slaus, Journal of Physics G: Nuclear and Particle Physics **27**, R69 (2001).

[56] N. Austern, Nuclear Physics **7**, 195 (1958).

[57] A. Gå rdestig, Journal of Physics G: Nuclear and Particle Physics **36**, 053001 (2009).

[58] S. Baker and R. D. Cousins, Nuclear Instruments and Methods in Physics Research **221**, 437 (1984).

[59] E. Gross and O. Vitells, The European Physical Journal C **70**, 525 (2010).

Acknowledgments

First of all, I would like to express my deepest gratitude to my supervisor Prof. Susumu Shimoura. He has been continuously giving me precious advice throughout the course of my study. Without his hearty encouragement, warm guidance, and valuable discussions, I could not have completed this work.

I also would like to express my gratitude to Dr. S. Michimasa. He gave me a lot of advices and discussion in detail. I would like to give my special thanks to Mr. H. Miya for his cooperation in the experiment and data analysis where we are faced with almost same difficulty. I have benefited from many friendship with members of NUSPEQ group: Prof. E. Ideguchi, Dr. S, Noji, Dr. M. Matsushita, Dr. D. Steppenbeck, Dr. S. Go, Mr. M. Takaki, Mr. R. Yokoyama, Mr. T. Fujii, Mr. M. Kobayashi and Mr. K. Kobayashi. They were always to listen, discuss or help me. I really enjoyed withe them in my research life.

I also appreciate for Prof. T. Uesaka, Prof. N. Imai, and Dr. S. Ota for giving me valuable advice and continuous support for my research activity. I am grateful for the CNS member and the SHARAQ group member for enjoying the research in my course of study. Especially for the member of the Prof. Yako group and Uesaka group: Prof. K. Yako, Dr. M. Dozono, Dr. H. Matsubara, Dr. Y. Sasamoto, Mr. L. Tang, Mr. H. Tokieda, Mr. S. Kawase, Mr. Y. Kubota and Mr. C. S. Lee, they discussed with me many things, encouraged me.

Many thanks to the member of the SHARAQ06 collaborators: Prof. H. Sakai, Prof. A. Tamii, Prof. T. Kawabata, Prof. D. Beaumel, Prof. Y. Maeda, Prof. A. Stolz, Dr. S. Takeuchi, Dr. S. Sakaguchi, Dr. M. Sasano, Dr. K. Miki, Dr. M. Kurata-Nishimura, Dr. Y. Kondo, Dr. M. Itoh, Dr. H. Baba, Dr. M. Assie, Dr. F. Hammache, Miss. M. Tsumura, Mr. T. Baba, Mr. T. Nishi, Dr. T. Kubo, Dr. N. Fukuda. Dr. N. Inabe, Dr. D. Kameda, Dr. H. Sato, Dr. Y. Shimizu, Dr. H. Suzuki, Dr. H. Takeda and Dr. Y. Yanagisawa. Without any work of collaborators, I could not accomplish the experiment.

I greatly acknowledge the support of the Junior Research Associate Program of the RIKEN and the member of the Uesaka Spin-Isospin laboratory.

I would like to thank Mr. H. Kurei, who direct how to prepare the equipment of the experiment and designed many experimental equipments. I also would like to thank Mr. Y. Ohshiro for for the operation of the ion source and provide a enough beam of our experiment. Special thanks go to Dr. S. Malek for her English edit with her kindness. This thesis become sophisticated due to her edit.

In daily life, I appreciate Miss. H. Kim, who give me many advice. Finally, I deeply express my appreciation of my family, father and mother for their encouragement and support over the year, and my wife, Mina, who is always the best sympathetic supporter of mine.

I am really sure that everything in the research life of this 5 years, including fun and though, are special pleasure in my life.